UNIVERSITY OF OKLAHOMA

GRADUATE COLLEGE

SEISMIC ATTRIBUTE ANALYSIS AND ITS APPLICATION TO MAPPING FOLDS AND FRACTURES

A DISSERTATION

SUBMITTED TO THE GRADUATE FACULTY

in partial fulfillment of the requirements for the

Degree of

DOCTOR OF PHILOSOPHY

By
HA THANH MAI

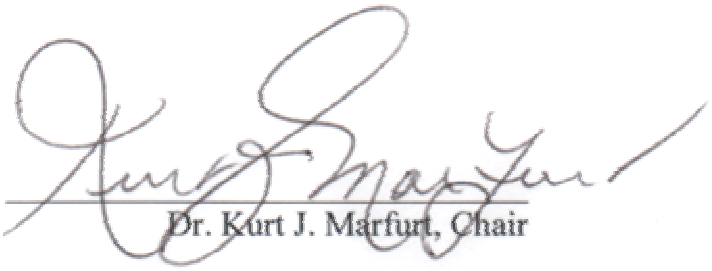
Norman, Oklahoma
2010

Downloaded from SHAREOK. Persistent Handle URL: https://hdl.handle.net/11244/318813

SEISMIC ATTRIBUTE ANALYSIS AND ITS APPLICATION TO MAPPING FOLDS AND FRACTURES

A DISSERTATION APPROVED FOR THE
CONOCOPHILLIPS SCHOOL OF GEOLOGY AND GEOPHYSICS

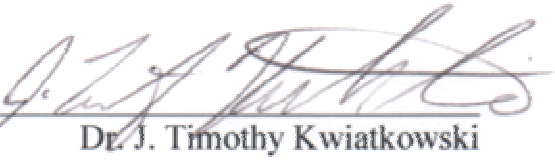
BY



Dr. Kurt J. Marfurt, Chair



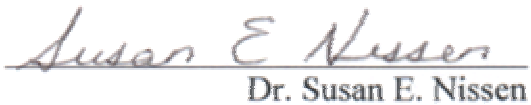
Dr. G. Randy Keller



Dr. J. Timothy Kwiatkowski



Dr. S. Lakshmivarahan



Dr. Susan E. Nissen

© Copyright by HA THANH MAI 2010

All Rights Reserved.

This dissertation is dedicated to my family and those who love and support me!

Acknowledgments

This dissertation would not have been possible without the help and support of so many people in so many ways.

I would like to express my wholehearted appreciation to Dr. Kurt J. Marfurt, my committee chair, my mentor, who has inspired, motivated, helped and supported me during my academic career. He passed along enthusiasm wisdom, giving me confidence, and leading me through the jungle of mist to come to this point. When I look at him, I just think of my dad, with a similar look, the same spirit and inspiration. He was really like a father to me, where I look up to, and depend on. Without his patient guidance, technical advice, sincere encouragement, the completion of this dissertation would not have happened. I also thank him for giving me the opportunity to work at the Attribute-Assisted Seismic Processing and Interpretation consortium, handling a great deal of data, working with various type of software, perfecting my programming skills, and connecting with many professional partners. I hope to maintain the scientific honesty I learnt from him, and to exceed his standards of excellence in my future career.

My special gratitude dedicated to Dr. Roger A. Young, who, regretfully passed away due to illness. Dr. Young was always by me, encouraged and supported me, especially when I was under stress and going downhill. Without him, I would not have gone this far.

I would like to thank Dr. G. Randy Keller, who has been always delightfully and cheerfully giving me support and advices. I would also like to express my sincere appreciation to the committee members, Dr. Tim Kwiatkowski, Dr. S. Lakshmivarahan, and Dr. Susan E. Nissen for their commitment to serve on my committee, their comments

and suggestions on this dissertation work. Especially to Dr. Tim Kwiatkowski, he's been giving me a lot of guidance on programming and computer management.

My great gratitude goes to Brad Wallet (Big Wallet), who has helped me a whole lot in both research and programming, writing Petrel's add-on modules that add significant value on my research. His constantly urged me to finish up (so he can put a bathtub in my office) every time he passed by, alternatively pulling strings or whipping me, to make my dissertation writing process go faster.

I want to thank PetroVietnam National Oil Group for their support on my studies, including financial support, research ideas, and the Cuu Long data volume that forms the central part of my research.

Living a long way from home as what seems to be a career student at the University of Oklahoma, I would like to thank the entire staff at the ConocoPhillips School of Geology and Geophysics: Donna Mullins, Nancy Leonard, Adrianne Fox, Niki Chapin, and Teresa Hackney. During my thirteen years living in Oklahoma, starting as a freshman and ending as a holder of a Ph.D. I have received so much help and love from you all. I thank you.

I deeply appreciate the companionship of my buddy Nguyễn Xuân Vinh. We don't share the same research interests, and we don't have many other points in common, but we get along just great. He's been a great supporter, listener, and sincere friend with who I could share stress or complaints, without worrying of damaging anyone. His knowledge and practice of Buddhism helped me when I needed to get back on my feet.

I also thank Sergio Chávez-Pérez of the IMP, who shared a lot of his experiences with me, giving me valuable suggestions and advice in both research and life. These

thanks extend to my dear friends Carlos Russian, Olubunmi Elebiju, Rachel Barber, Marcilio Matos, Oswaldo Davogustto, Victor Pena and many others at CPSGG. We've had a great time working and playing here. I also thank all my Vietnamese friends at OU, and at my organization H-A-O, who have shared all the joys and tears with me, cheered me when I was successful, and supported me when I failed.

Deep in my heart, I am thankful to Mr. and Mrs. Flanagan, for their caring, feeding, teaching, and simply loving me since the first day I came to U.S. I dearly call them "Uncle Larry" and "Má Hà". They are truly like second parents to me.

Finally, I am deeply indebted to my parents, Mr. Mai Thanh Tân and Mrs. Bùi Thúy Nga, and my brother Mai Hải Lâm and his family, for their endless support and loving. It is their inspiration, encouragement, and nourishment that help me successful and become who I am right now. The big dedication of this dissertation is for my father, who is a geophysics professor at Hanoi University of Mining and Geology. Professionally, he inspired me into this wonderful geophysics world, from my childhood, when he brought home some long seismic lines in paper, and did interpretation on it with color pencils. A long way raising me up, he keep encouraging and supporting me until today, and I am sure he will always be by me in every step that I go in the future. In my eyes, he is a great geophysics professor, a great teacher who was loved and respected by many (that many time I ask myself, how I can be one like him). And more than that, he is also a friend, who listens to me, share and support my line of thinking and decisions.

We have a slogan: "Make dreams happen". I am making my dream happen.

Table of Contents

Acknowledgments ..... **iv**

Table of Contents ..... **vii**

List of Figures ..... **ix**

Abstract ..... **xvii**

Chapter 1 Motivation and Objectives **1**

Chapter 2 Introduction **3**

Chapter 3 Theory and Methodology **5**

Structural dip, amplitude gradient, and curvature – A 360^{o} perspective 5
Curvature 7
Geometric description 7
Mathematical description 8
Shape index and curvedness 9
Curvature Lineaments – Multi-attribute displays and rose diagrams 10
Summary 11
List of Figures 12
References 19

Chapter 4 Attributes applied to the Cuu Long Basin, Vietnam **21**

Description 21
Enhanced seismic data processing and interpretation for fractured basement in the Cuu Long basin, Vietnam 22

Chapter 5 Attributes applied to the Chicontepec basin, Mexico **45**

Description 45
Attribute-aided interpretation of complex structures, an example from the Chicontepec basin, Mexico 46

Chapter 6 Use of seismic attributes in structural interpretation **76**

Summary 76
Attribute Illumination of basement faults, Cuu Long Basin, Vietnam 78
Attribute illumination of basement faults, examples from Cuu Long Basin basement, Vietnam and the Midcontinent, USA 83
Curvature lineaments and multi-attribute display of full-stack PP, SS, and acoustic impedance seismic data – Diamond-M field, West Texas 93
Coherence and volumetric curvature and their spatial relationship to faults and folds, an example from Chicontepec basin, Mexico 98
Using 3D rose diagrams for correlation of seismic fracture lineaments with similar lineaments from attributes and well log data 103
Multi-attribute display and rose diagrams for interpretation of seismic fracture lineaments, example from the Cuu Long Basin, Vietnam 108

Using automatically generated 3D rose diagrams for correlation of seismic fracture lineaments with similar lineaments from attributes and well log data..... 112

Chapter 7 Conclusions..... 118

Appendix..... 119

Overview..... 119
Master Graphic User Interface (GUI): aaspi_util 122
AASPI seismic attribute GUIs and computing programs..... 124

List of Figures

Theory and Methodology…….5

Figure 1: Mathematical definition of a dipping surface. By convention, n = unit vector normal to the surface; a = unit vector dip along the surface; θ = dip magnitude; ψ = dip azimuth; ξ = strike; θ_x = the apparent dip in the *xz* plane; and θ_y = the apparent dip in the *yz* plane (modified after Chopra and Marfurt 2007).....12
Figure 2: Outcrop of fracture granite basement in Phan Thiet, Vietnam. The exfoliation fracture surface (rectangle) is represented by the strike ξ in E-W direction, dipping θ into the direction of unit vector dip a (image courtesy of PetroVietnam).....12
Figure 3: A schematic diagram showing a 2D estimate of coherence. The high coherence response represents a seismic reflector (modified after Marfurt et al. 1998).....13
Figure 4: A schematic diagram showing a 3D search-based estimate of coherence, in which p_x indicates the inline and p_y the crossline components of vector time dip (modified after Marfurt et al. 1998).....13
Figure 5: A schematic diagram showing the calculation of seismic reflector dip. θ_x = the apparent dip magnitude in the *x* direction. p_x = the inline components of vector time dip. *v* = average time to depth conversion velocity.....14
Figure 6: Processing workflow to generate directional attributes. (a) Generating directional dip or amplitude energy gradient attribute from seismic amplitude. (b) Generating Euler curvature attributes from inline and crossline dip attributes.....14
Figure 7: Folding surface, Lago Argentino.....15
Figure 8: Definition of curvature. For a particular point P on a curve, green arrows indicate normal vectors, n, to the curve. τ is the vector tangent to the curve at point P. Curvature is defined in terms of the radius of the circle tangent to the curve at the analysis point. Anticlinal features have positive curvature (k_{2D}>0), and synclinal features have negative curvature (k_{2D} <0). Planar features (dipping or horizontal) have zero curvature (k_{2D} =0) (modified after Roberts, 2001).....15
Figure 9: A quadratic surface with the normal, n, defined at point *P*. The circle tangent to the surface whose radius is minimum defines the magnitude of the maximum curvature, $|k_{max}| \equiv 1/R_{min}$ (in blue). For a quadratic surface, the plane perpendicular to that containing the previously defined blue circle will contain one whose radius is maximum, which defines the magnitude of the minimum curvature, $|k_{min}| \equiv 1/R_{max}$ (in red). Graphically, the sign of the curvature will be negative if it defines a concave surface and positive if it defines a convex surface. For seismic interpretation, we typically define anticlinal surfaces as being convex up, such that k_{max} has a negative sign and k_{min} has a positive sign in this image.....16
Figure 10: The definition of 3D quadratic shapes expressed as a function of the most-positive principal curvature, k_1, and the most-negative principal curvature, k_2. By definition, $k_1 \geq k_2$. Thus, if both k_1 and k_2 are less than zero, we have a bowl; if both are greater than zero, we have a dome; and if both are equal to zero, we have a plane.....16
Figure 11: Example of shape index modulated by curvedness. Chicontepec, Mexico.....17
Figure 12: Example of ridge curvedness and the azimuth of minimum curvature composite image, DiamondM, Texas.....17
Figure 13: G function of shape components (al-Dossary and Marfurt, 2006).....18
Figure 14: Example of 3D rose diagrams on time structure map, DiamondM, Texas.....18

Attributes applied to the Cuu Long Basin, Vietnam……...21

Figure 1: Cuu Long basin in the Southeast Continental shell of Vietnam (image courtesy of PetroVietnam). 36
Figure 2: Geological cross section, Cuu Long basin. 37
Figure 3: Seismic cross section showing fractures and faults inside granite basement, generated during rifting of the basin. 37
Figure 4: Seismic model representing fractured basement in Cuu Long Basin. 38
Figure 5: Modeled gather (a) before and (b) after application of parabolic Radon filter. 38
Figure 6: Time-migrated seismic section showing the basement (a) before and (b) after re-processing with Radon and τ-p filters applied. 39
Figure 7: Comparison of (a) Kirchhoff depth migration and (b) controlled beam migration on depth slice at z=3100m. Line AA' shown in Figure 8. While the lateral resolution is slightly lower, the controlled beam migration much better indicates the fractures. 40
Figure 8: Comparison of (a) Kirchhoff depth migration and (b) controlled beam migration on a vertical seismic section. Yellow line indicates location of depth slice displayed in Figure 7. 41
Figure 9: Mathematical, geologic, and seismic nomenclature used in defining reflector dip. By convention, n = unit vector normal to the reflector; a = unit vector dip along the reflector; θ = dip magnitude; ψ = dip azimuth; ξ = strike; θ_x = the apparent dip in the xz plane; and θ_y = the apparent dip in the yz plane (after Chopra and Marfurt 2007). 42
Figure 10: Vertical seismic section showing top of basement and interpreted faults. Depth slices shown in Figure 11-13 are indicated in green and yellow lines. 42
Figure 11: Depth slices at z=2850 m through apparent dip, p_ψ, computed at apparent direction ψ=0^O, 30^O, 60^O, 90^O, 120^O, and 150^O from North. White arrows indicate lineaments were interpreted as main NE-SW faults running along basement top. Red and yellow arrows indicate faults and fractures within basement. 43
Figure 12: Depth slices at z=3100 m through apparent dip, p_ψ, computed at apparent direction ψ=0^O and 60^O from North. 43
Figure 13: Depth slices at z=3100 m through apparent amplitude gradients, gψ, computed at apparent direction ψ=0^O, 30^O, 60^O, 90^O, 120^O, and 150^O from North. White arrows indicate lineaments were interpreted as main NE-SW faults running along basement top. Red and yellow arrows indicate faults and fractures within basement. 44

Attributes applied to the Chicontepec Basin, Mecico……...45

Figure 1. Definition of curvature. For a particular point P on a curve. Green arrows indicate normal vectors, n, to the curve. τ is the vector tangent to the curve at point P. Curvature is defined in terms of the radius of the circle tangent to the curve at the analysis point. Anticlinal features have positive curvature (k_{2D}>0), and synclinal features have negative curvature (k_{2D} <0). Planar features (dipping or horizontal) have zero curvature (k_{2D} =0). (Modified after Roberts, 2001). 63
Figure 2. (a) A quadratic surface with the normal, n, defined at point P. (b) The circle tangent to the surface whose radius is minimum defines the magnitude of the maximum curvature, $|k_{max}| \equiv 1/R_{min}$ (in blue). For a quadratic surface, the plane perpendicular to that containing the previously defined blue circle will contain one whose radius is maximum, which defines the magnitude of the minimum curvature, $|k_{min}| \equiv 1/R_{max}$ (in red). Graphically, the sign of the curvature will be negative if it defines a concave surface and positive if it defines a convex surface. For seismic interpretation, we typically define anticlinal surfaces as being convex up, such that k_{max} has a negative sign and k_{min} has a positive sign in this image. 63
Figure 3. Lateral displacement of most-positive (k_{pos}) and most-negative curvature (k_{neg}) anomalies, correlating the crest and trough of the folded structure from what we denote as

the most-positive and most-negative principal curvature anomalies (k_1 and k_2) which correlate to the more geologically relevant anticlinal and synclinal fold axes. For this image with approximately 2D symmetry in the vertical plane, the anomalies for k_{max} would be identical in location and sign for those of k_1 and k_2, such that the major anomalies could be efficiently mapped using a single (rather than two) attributes. 64
Figure 4. Normal faults expressing different mechanisms: (a) a fault showing simple displacement with no drag, that would result in a coherence anomaly, but exhibiting no change in dip and hence no volumetric curvature anomalies, (b) a fault with drag on both sides exhibiting no coherence anomalies, but a most-positive principal curvature anomaly on the footwall (in red) and a most-negative principal curvature anomaly on the hanging wall (in blue), and (c) a growth fault with syntectonic deposition, which would exhibit both a coherence anomaly and a most-positive principal curvature anomaly over the roll-over anticline (in red). 65
Figure 5. A vertical slice along y=-30 m, of the 3D derivative operator s (a) $\partial/\partial x$, (b) $\partial/\partial y$, and (c) $\partial/\partial t$ applied to the inline and crossline components of dip used in volumetric curvature computation for data sampled at Δx=30 m, Δy=30 m, and Δt=2 ms. The operator $\partial/\partial t$ is computed from $\partial/\partial z$ using a constant reference velocity. The value of $\partial/\partial y$ along $y=0$ is identically zero. 66
Figure 6. (a) Representative seismic amplitude vertical and time slice. On the same slices, I co-render (b) shape index modulated by curvedness with (c) seismic amplitude and (d) coherence. The seismic amplitude is set to be 50% transparent. White arrows indicate faults, blue arrows indicate valleys, and yellow arrows indicate ridge features. (e) 2D color table used in shape index modulated by curvedness, and color legend for coherence and seismic amplitude. 67
Figure 7. Location of Chicontepec basin, Mexico. (After Salvador, 1991). 68
Figure 8. Most-positive curvature anomalies (yellow) co-rendered with most-positive principal curvature anomalies (red). Note how the anomalies are aligned in the western, flatter part of the image. 69
Figure 9. (a) A cartoon of a fold. Anticlinal feature with most-positive principal curvature anomalies, k_1, in red, delineating the anticline's hinge line, and most-negative principal curvature anomalies, k_2, in blue, corresponding to the synclinal axes of the fold. There are no significant coherence anomalies. (b) Representative vertical slice through the seismic amplitude volume showing a fold. (c) Seismic amplitude co-rendered with most-positive and most-negative principal curvatures. (d) 3D view of a vertical and time slice through the amplitude data co-rendered with most-positive and most-negative principal curvature. (e) The shape index modulated by curvedness, co-rendered with seismic amplitude. 2D color legend same as Figure 6e. 70
Figure 10. (a) Cartoon of a pop-up structure showing two faults giving rise to coherence (green) anomalies separating most-positive principal curvature (red), and most-negative principal curvature (blue) anomalies. (b) Vertical section through the seismic amplitude data showing a pop-up block. (c) Seismic amplitude co-rendered with most-positive and most-negative principal curvatures and coherence. (d) 3D view of a vertical and time slice through the amplitude data co-rendered with most-positive and most-negative principal curvature and coherence. (e) The shape index modulated by curvedness, co-rendered with coherence and seismic amplitude. 2D color legend same as Figure 6e. 71
Figure 11. (a) Cartoon of a graben structure showing two faults giving rise to coherence (green) anomalies separating most-positive principal curvature (red), and most-negative principal curvature (blue) anomalies. (b) Vertical section through the seismic amplitude data showing graben. (c) Seismic amplitude co-rendered with most-positive and most-negative principal curvatures and coherence. (d) 3D view of a vertical and time slice through the amplitude data co-rendered with most-positive and most-negative principal curvature and coherence.

(e) The shape index modulated by curvedness, co-rendered with coherence and seismic amplitude. 2D color legend same as Figure 6e. 72
Figure 12. Seismic artifacts due to shallow volcanic and low fold giving rise to curvature and coherence anomalies. 73
Figure 13. (a) Time-structure map of the top-Cretaceous horizon. (b) Horizon slice through coherence along the top-Cretaceous co-rendered with corresponding most-positive and most-negative principal curvature slices. (c) Horizon slice through coherence along the top-Cretaceous co-rendered with the shape-index modulated by curvedness slice. 2D color legend same as Figure 6e. 74
Figure 14. (a) Time slice at 1.5s at the approximate top Cretaceous level though seismic amplitude, co-rendered with corresponding most-positive and most-negative principal curvature slices. (b) Time slice at 1.5s at the approximate top Cretaceous level though coherence along the top-Cretaceous co-rendered with the shape-index modulated by curvedness slice. 2D color legend same as Figure 6e. 75

Attribute Illumination of basement faults, Cuu Long Basin, Vietnam……...78

Figure 1: Mathematical, geologic, and seismic nomenclature used in defining reflector dip. By convention, n = unit vector normal to the reflector; a = unit vector dip along the reflector; θ = dip magnitude; ψ = dip azimuth; ξ = strike; θx = the apparent dip in the xz plane; and θy = the apparent dip in the yz plane. (after Chopra and Marfurt 2007) 78
Figure 2: Seismic section on (a) apparent dip depth slice and (b) amplitude gradient. The white arrows show location where the attributes help interpreting fault features 79
Figure 3: Depth slices at z=2750 m through apparent dip, p_{ψ}, computed at ψ=0^{O}, 30^{O}, 60^{O}, 90^{O}, 120^{O}, and 150$^{O.}$ from North. Block white arrows indicate lineaments that we interpret to be associated with faults and fractures. Several meandering channel segments can be seen in the sedimentary section to the SE. 80
Figure 4: Depth slices at z=2750 m through apparent amplitude gradients, g_{ψ}, computed at ψ=0^{O}, 30^{O}, 60^{O}, 90^{O}, 120^{O}, and 150$^{O.}$ from North. Block white arrows indicate lineaments that we interpret to be associated with faults and fractures. Several meandering channel segments can be seen in the sedimentary section to the SE. 81
Figure 5: Depth slices at z=2750 m through (a) maximum curvature (b) minimum curvatures and (c) azimuth of minimum curvature 81

Attribute illumination of basement faults, examples from Cuu Long Basin basement, Vietnam and the Midcontinent, USA……...83

Figure 1: Mathematical, geologic, and seismic nomenclature used in defining reflector dip. By convention, n = unit vector normal to the reflector; a = unit vector dip along the reflector; θ = dip magnitude; ψ = dip azimuth; ξ = strike; θ_x = the apparent dip in the *xz* plane; and θ_y = the apparent dip in the *yz* plane. (after Chopra and Marfurt 2007) 83
Figure 2: An illustrated definition of 2D curvature. Concave downward features have a positive value while concave upward features have a negative value. 84
Figure 3: Seismic section on (a) negative curvature and (b) positive curvature depth slice. The arrows show location where the attributes help interpreting fault features 85
Figure 4: Depth slices at z=2750 m through apparent dip, p_{ψ}, computed at ψ=0^{O}, 30^{O}, 60^{O}, 90^{O}, 120^{O}, and 150$^{O.}$ from North. Block white arrows indicate lineaments that we interpret to be associated with faults and fractures. Several meandering channel segments can be seen in the sedimentary section to the SE. Cuu Long basin 87

Figure 5: Depth slices at z=2750 m through apparent amplitude gradients, g_{ψ}, computed at ψ=0^{O}, 30^{O}, 60^{O}, 90^{O}, 120^{O}, and 150$^{O.}$ from North. Block white arrows indicate lineaments that we interpret to be associated with faults and fractures. Several meandering channel segments can be seen in the sedimentary section to the SE. Cuu Long basin.....88
Figure 6: (a) Depth slices at z=2750 m through apparent dip, p_{ψ}, computed at ψ=0^{O} from North. (b) Major fault frequency detected in direction ψ=0^{O}. Mean direction of faults detected in this case is about 74^{0}. Cuu Long basin.....88
Figure 7: (a) Depth slices at z=2750 m through apparent dip, p_{ψ}, computed at ψ=90^{O} from North. (b) Major fault frequency detected in direction ψ=90^{O}. Mean direction of faults detected in this case is about 161^{0}. Cuu Long basin.....89
Figure 8: (a) Depth slices at z=2750 m through apparent amplitude gradients, p_{ψ}, computed at ψ=0^{O} from North. (b) Major fault frequency detected in direction ψ=0^{O}. Mean direction of faults detected in this case is about 69^{0}. Cuu Long basin.....89
Figure 9: (a) Depth slices at z=2750 m through apparent amplitude gradients, p_{ψ}, computed at ψ=90^{O} from North. (b) Major fault frequency detected in direction ψ=90^{O}. Mean direction of faults detected in this case is about 157^{0}. Cuu Long basin 89
Figure 10: Depth slices at z=2750 m through (a) seismic, (b) variance, (c) positive curvature, and (d) negative curvature – Cuu Long basin 90
Figure 11: Seismic section on (a) negative curvature and (b) positive curvature time slice. The arrows show location where the attributes aided fault interpretation - Osage county.....90
Figure 12: Time slices at z=700ms through (a) seismic, (b) variance, (c) negative curvature, and (d) positive curvature. Osage county.....91
Figure 13: Time slices at z=630 ms through (a) seismic, (b) variance, (c) negative curvature, and (d) positive curvature. Osage county.....91
Figure 14: Time slices at 700ms through (a) inline amplitude gradient, (b) crossline amplitude gradient and Time slices at 630ms through (a) inline amplitude gradient, (b) crossline amplitude gradient. Osage county.....92

Curvature lineaments and multi-attribute display of full-stack PP, SS, and acoustic impedance seismic data – Diamond-M field, West Texas……..…….93

Figure 1: Location of study area, Midland basin, Texas. (after WorldOil.com).....93
Figure 2: An illustrated definition of 3D curvature. Synclinal features have negative curvature and anticlinal features have positive curvature. (After Lisle, 1994). 93
Figure 3: 2D multi-attribute display. The ridge component of curvedness is plotted against lightness and modulates the azimuth of minimum curvatures, ψ_{min}, plotted against hue.....93
Figure 4: (a) Multi-attribute display of the azimuth of minimum-curvature, ψ_{min}, modulated by the ridge component of curvedness and (b) the corresponding rose diagrams. 94
Figure 5: Time structure map coresponding to top of Pennsivanian age Canyon Reef formation, interpreted from the PP seismic data.....94
Figure 6: PP data at time slice *t=935ms* just below the top of the Canyon Reef Fm through (a) most-positive and (b) most- negative curvature volumes. (c) Multi-attribute display using transparency to show anomalous features seen in (a) and (b) on top of the seismic amplitude time slice. (d) Multi-attribute ridge-ψ_{min}, display described in Figure 3 overlain by rose diagrams (in white). 95
Figure 7: SS data at time slice *t=1871ms* (just below the top of the Canyon Reef Fm and equivalent to 935ms in PP data) through Reef Fm through (a) most-positive and (b) most-negative curvature volumes. (c) Multi-attribute display using transparency to show anomalous features seen in (a) and (b) on top of the seismic amplitude time slice. (d) Multi-attribute ridge-ψ_{min}, display overlain by rose diagrams (in white). 96

Figure 8: Acoustic Impedance data at time slice *t=935ms* just below the top of the Canyon Reef Fm through (a) most-positive and (b) most- negative curvature volumes. (c) Multi-attribute display using transparency to show anomalous features seen in (a) and (b) on top of the seismic amplitude time slice. (d) Multi-attribute ridge-ψ_{min}, display overlain by rose diagrams (in white). 96

Multi-attribute display and rose diagrams for interpretation of seismic fracture lineaments, example from the Cuu Long Basin, Vietnam……...98

Figure 1: An illustrated definition of 3D curvature. Synclinal features have negative curvature and anticlinal features have positive curvature 98
Figure 2: Most-positive and most-negative curvatures (Modified from Lisle, 1994)..... 98
Figure 3: Illustration of fold with positive and negative curvature..... 98
Figure 4: An illustration of normal faults with positive and negative curvature: (a) simple displacement with no drag, (b) fault with drag on one side, (c) fault with drag on two sides, and (d) fault with syntectonic depositions..... 99
Figure 5: Ant-tracking on most-positive curvature (red, with blue arrow) and on new defined maximum curvature (pink, with pink arrow). 99
Figure 6: Anticlinal feature. Minumum curvature features (blue) delineate the two limbs of the fold, while maximum curvature (red) delineate the axial plane.. There are no significant coherence anomalies. 100
Figure 7: Intepreted faults (yellow) on a pop-up feature bound by coherence (green), maximum curvature (red), minimum curvature (blue) anomalies..... 100
Figure 8: Interpreted faults (yellow) and intervening graben delineated by maximum curvature (red) and minimum curvature and coherence (green). 100
Figure 9: A representative seismic line with (a) interpreted faults, (b) coherence, (c) co-rendered ant-tracked maximum curvature, minimum curvature and coherence with the vertical seismic line, and (d) with an itersecting time slice as well. Intepreted faults (yellow) on a pop-up feature bound by coherence (green), maximum curvature (red), minimum curvature (blue) anomalies. 101
Figure 10: Interpreted faults (yellow) and intervening graben delineated by maximum curvature (red) and minimum curvature and coherence (green): (a) seismic line with interpreted fault (b) coherence, c) ant-tracked maximum curvature, minimum curvature and coherence on seismic line, d) their horizontally extend. 101

Using 3D rose diagrams for correlation of seismic fracture lineaments with similar lineaments from attributes and well log data ……....103

Figure 1. Lineaments on most-positive curvature horizon slice manually-interpreted as yellow line segments and transformed into a rose diagram shown in the inset.(After Chopra and Marfurt, 2007b). 105
Figure 2. Strat-slice from coherence volume displayed at a marker horizon and merged with 3D rose diagrams (in red) generated with a search radius of 600 m. In (a) the rose diagrams were generated with the ridge attribute and in (b) the roses were generated with the valley attribute. Notice that there are slight differences in their amplitudes but the orientations seem to be close. 105
Figure 3. Strat-slice from coherence volume displayed at a marker horizon and merged with 3D rose diagrams (in red) generated with a search radius of (a) 300m, (b) 600 m, and (c) 100m. In all cases the valley attribute was used besides the azimuth of minimum curvature. Notice that this choice will depend to a large extent on the features on the horizon or time slices being viewed. 105

Figure 4. 3D rose diagrams merged with a truncated coherence volume. This composite volume can now be animated to view the alignment and orientation of the features seen on the coherence with roses generated from different attributes and eventually with similar roses from image logs. 106
Figure 5. A blow up of the 3D Rose diagrams at individual points in the 3D volume. Notice the alignment of the petals is not the same within the thickness of the strat-cube, and the changes in orientation of fractures with time are indicated with yellow arrows. 106
Figure 6. Strat-cube from a merged volume comprising the 3D rose diagrams as well as the coherence attribute, shown in (a) at 50 ms, and (b) 100 ms below a marker horizon. This composite volume can now be animated to view the alignment and orientation of the features seen on the coherence with roses shown and eventually with similar roses from image logs. 106

Multi-attribute display and rose diagrams for interpretation of seismic fracture lineaments, example from the Cuu Long Basin, Vietnam……..... 108

Figure 1. An illustrated definition of 3D curvature. Maximum curvature has shortest radius and minimum curvature has largest radius. Minumum curvature azimuth is the direction of minumum curvature. (After Lisle, 1994) 108
Figure 2. Geometry of of some folded surfaces. By definition, $k_{neg} \leq k_{pos}$. If $k_{pos} = 0$ and $k_{neg} < 0$, we have a valley shape, and if $k_{pos} > 0$ and $k_{neg} = 0$, we have a ridge shape. (After Bergbauer et al, 2003) 109
Figure 3. Combination of the azimuth of minimum-curvature, ψ_{min}, and the ridge component of curvedness to create multi-attribute display and rose diagrams. 109
Figure 4. 2D multi-attribute display. The ridge component of curvedness is plotted against lightness and modulates the azimuth of minimum curvatures, ψ_{min}, plotted against hue. 109
Figure 5. (a) Multi-attribute display of the azimuth of minimum-curvature, ψ_{min}, modulated by the ridge component of curvedness and (b) the corresponding rose diagrams. 109
Figure 6. (a) Seismic amplitude time slice below top of granite basement, (b) Multi-attribute display of ψ_{min} modulated by the ridge curvedness, (c) the blended images with rose diagrams (white) 111
Figure 7. 3D rose diagrams showing on (a) truncated seismic volume, (b) depth structure map of top basement 111

Using automatically generated 3D rose diagrams for correlation of seismic fracture lineaments with similar lineaments from attributes and well log data……..... 112

Figure 1. Horizon slice for the most-positive curvature attribute. Lineaments interpreted as faults are marked as yellow line segments and have been transformed into the rose diagram shown in the inset. (After Chopra and Marfurt, 2007b). 113
Figure 2. Horizon slices from (a) coherence, (b) ridge, and (c) valley attributes. 113
Figure 3. Strat-slice from a coherence volume displayed at a marker horizon and merged with 3D rose diagrams (in red) generated with a search radius of (a) 300 m, (b) 600 m, and (c) 1000 m. In all cases, the other attribute used was the ridge attribute. Notice that this choice will depend to a large extent on the features on the horizon or time slice being viewed. 114
Figure 4. Rose diagrams displayed 40 ms above a marker horizon. 115
Figure 5. 3D rose diagrams merged with a truncated stratal coherence volume. This composite volume can now be animated to view the alignment and orientation of the features seen on the coherence with roses generated from different attributes and eventually with similar roses from image logs. 116

Figure 6. A zoom of the 3D rose diagrams at individual points in the 3D volume. Notice the alignment of the petals is not the same within the thickness of the strat-cube, and the changes in orientation of fractures with time are indicated with yellow arrows. 116
Figure 7. Strat-cube from a merged volume comprising the 3D rose diagram as well as the coherence attribute, shown in (a) at 50 ms, and in (b) at 100 ms below the marker horizon. This composite volume can now be animated to view the alignment and orientation of the features seen on the coherence with roses generated from different attributes and eventually with similar roses from image logs. 116

Appendix……..……...119

Figure A1: AASPI software workflow 120
Figure A2: AASPI software components..... 120
Figure A3: AASPI Utilities..... 122
Figure A4: AASPI Manual: Running AASPI Software with GUIs..... 123
Figure A5: AASPI dip3d 124
Figure A6: AASPI Dip Angle Estimator 125
Figure A7: AASPI image_filt3d 126
Figure A8: AASPI sof3d..... 126
Figure A9: AASPI similarity3d 127
Figure A10: AASPI curvature3d 127
Figure A11: AASPI apparent_cmpt..... 128
Figure A12: AASPI euler_curvature..... 128
Figure A13: AASPI real_pca_spectra..... 129
Figure A14: AASPI real_pca_waveform..... 129
Figure A15: AASPI generate_roses..... 130
Figure A16: AASPI spec_cmp..... 130
Figure A17: AASPI footprint_suppression..... 131
Figure A18: AASPI glcm3d..... 131
Figure A19: AASPI hlplot 132
Figure A20: AASPI hsplot..... 133
Figure A21: AASPI hlsplot3d..... 134
Figure A22: AASPI spec_cmp_plot (4D)..... 135

Abstract

Geometric attributes such as coherence and curvature have been very successful in delineating faults in sedimentary basins. While not a common exploration objective, fractured and faulted basement forms important reservoirs in Venezuela, USA (Southern California), Brazil, Libya, Algeria, Egypt, Russia, and Vietnam (Landes, 1960; Canh, 2008). Because of the absence of stratified, coherent reflectors, illumination of basement faults is more problematic than illumination of faults within the sedimentary column. In order to address these problems, it is important to carefully analyze alternative forms of the 3D seismic data, which in this dissertation will be primarily combinations of one or more seismic attributes, and interpret them within the context of an appropriate structural deformation model. For that purpose, in this research, I concentrate on analyzing structural dip and azimuth, amplitude energy gradients, and a large family of attributes based on curvature to better illuminate fracture 'sweet spots' and estimate their density and orientation. I develop and calibrate these attribute and interpretation workflows through application to a complexly folded and faulted, but otherwise typical, geologic target in the Chicontepec Basin of Mexico. I then apply this calibrated workflow to better characterize faults and build fracture models in the granite basement of the Cuu Long Basin, Vietnam, and the granite and rhyolite-metarhyolite basement of Osage County, Oklahoma, USA. In the Cuu Long granite basement, it forms an important unconventional reservoir. In Osage County, we suspect basement control of overlying fractures in the Mississippian chat deposits.

References

Canh, T. N, 2008, Achievements of 20 years hydrocarbon exploration and production in fractured granite basement reservoirs: Fractured Basement Reservoir, PetroVietnam, **2**, 13-18.

Landes, K. K., Amoruso, J. J., Charlesworth, L. J., Heany, F. and Lesperancep, J., 1960, Petroleum resources in basement rocks. AAPG Bull., **44**, 1682-1691.

Chapter 1 Motivation and Objectives

In Vietnam, the first oil and gas discovery in fractured granite basement rocks was in 1987. Since that time, oil and gas production from fractured granite basement reservoirs has played a very important part in the oil and gas industry of Vietnam, as well as the national economy development. Although there have been exploration and production activities in fractured basement reservoirs in Vietnam for over 20 years, there are still a lot of challenging problems that remain unsolved, to enhance oil recovery from this special type of reservoir (Canh, 2008).

The illumination of faults is more problematic in granite basement than in the sedimentary zones, for a number of reasons: in the granite basement, faults and fractures are more complicated, and lack horizontal, coherent layered reflectors, and the seismic data quality is much lower.

The basement fractures increase porosity and permeability, allowing it to serve as a hydrocarbon reservoir. Knowing fault/fracture intensity and orientation can guide horizontal drilling programs, thereby increasing production, and optimizing drainage.

In this research, I use detailed analysis of seismic attributes relate to folds, faults and fractures, including structural dip, amplitude gradients, and curvature and coherence to better delineate structurally complex features, map density and orientation of fracture zones.

Objective of my research is to provide methods and tools to enhance the signature of basement faults or fractures zone, to automatically and quickly evaluate fracture intensity and orientation, thereby locating potential prospects, and aiding design of horizontal drilling programs to enhance production and maximize drainage.

References

Canh, T. N, 2008, Achievements of 20 years hydrocarbon exploration and production in fractured granite basement reservoirs: Fractured Basement Reservoir, PetroVietnam, 13-18.

Chapter 2 Introduction

The oil industry has been developing rapidly. Most of the conventional reservoirs that fall within today's environmental and political constraints have been found or are being actively explored. As the task for exploration becomes more difficult, we need to look for oil and gas reservoir targets that are smaller, deeper, poorly illuminated due to complex structure, or are considered unconventional, requiring hydraulic fracturing, or are "new" play concepts, such as production from basement. To achieve these goals, new technologies are required, new research is carried out, and new processing algorithms are developed. In this dissertation, I summarize the research and contributions I have made as part of OU's Attribute-Assisted Seismic Processing and Interpretation (AASPI) research team. I have developed my own algorithms, debugged algorithms written by colleagues (and my own), developed graphical user interfaces, and most important, developed and calibrated workflows in applying seismic attributes to structurally complex environments such as the granite basement faulting in the Cuu Long Basin, Vietnam, the faulted and folded environment of Chicontepec Basin, Mexico, and many other places.

Since my goal has been not only the development but also the transfer of technology, my dissertation will be in form of a list of scientific papers and published expanded abstracts.

In Chapter 3, I begin with a summary of some of the basic concepts necessary to read the subsequent chapters – definitions of volumetric dip and azimuth, curvature, reflector shapes, amplitude gradients, and so forth, some of which were developed by me (Euler curvature and volumetric rose diagrams) and others that were developed by colleagues.

Chapter 4 is a paper to be submitted in May 2010 to *Geophysics* on the Cuu Long Basin, Vietnam, that forms the primary focus of my thesis.

Chapter 5 is a paper to be submitted in May 2010 to *Geophysics* on the Chicontepec Basin, Mexico, which serves as the calibration of my attribute interpretation workflows on a data volume that is difficult, but somewhat conventional, in that the folding and faulting occurs in the sedimentary column rather than basement.

Chapter 6 includes a suite of seven expanded abstracts that have presented and published at international meetings in the U.S.A., Australia, Vietnam, and Japan, as well as a paper published in the *First Break* where Satinder Chopra applied some of my workflows to data acquired over complex faulted geology from Alberta, Canada.

Each of the above papers and expanded abstracts are followed by the appropriate references.

I conclude this thesis with a snapshot of the Graphical User Interfaces (GUIs) that I have developed, along with a few representative shell scripts. I am proud to say that these GUIs are currently being used by the 16 AASPI's sponsors, representing the six inhabited continents. Although a computer programming exercise rather than a scientific contribution, I wish to include it not so much because of the considerable time invested in their development, but rather because the 'client interaction' of such software distribution and support helped my define and clarify our attribute work flows much more clearly.

Chapter 3 Theory and Methodology

Structural dip, amplitude gradient, and curvature – A 360^o perspective

Geologically and mathematically, a planar surface such as a formation top, a dipping bed or a fault surface can be represented by the magnitude of its true dip θ and strike ξ, or dip azimuth ψ, with respect to North. The true dip θ can be represented by apparent dips θ_x and θ_y along the *x* and *y* axes (Figure 1). Figure 2 is an example of a faulted surface from Phan Thiet, Vietnam. The exfoliation fault plane (rectangle) is represented by strike ξ in NE-SW direction, and dipping with magnitude θ into the direction of unit vector dip.

Seismically, any impedance contrast can scatter energy sent from the seismic source back to receivers. The seismic response of a smooth reflector results in aligned peak and troughs. We can find the dip of a reflector by searching for the dip angle exhibits the maximum semblance (Figure 3).

There are several popular means of computing volumetric dip components, including those based on weighted versions of the instantaneous frequency and wave-numbers (Barnes, 2000), on the gradient structure tensor (Randen et al., 2000) and on discrete semblance-based dip searches (Marfurt, 2006).

Figure 4 is a schematic diagram showing a 3D search-based estimate of seismic coherence, for time-migrated seismic data, with apparent dip components (p_x, p_y) along the inline and crossline directions in *s/ft* or *s/m*. Apparent dip components are computed as:

$$p_x = \Delta t / \Delta x , \tag{1a}$$

$$p_y = \Delta t / \Delta y . \tag{1b}$$

For depth-migrated seismic data such as our Cuu Long survey, we simply compute θ_x and θ_y and display them either as components or as dip magnitude, θ, and dip azimuth, ψ, or alternatively as dimensionless apparent dip components (p_x, p_y) measured in ft/ft or m/m.

$$\theta_x = \text{atan}(\Delta z / \Delta x), \tag{2a}$$

$$\theta_y = \text{atan}(\Delta z / \Delta y). \tag{2b}$$

The relationship between apparent seismic time dips and apparent angle dips are:

$$p_x = 2 * \tan(\theta_x) / v, \tag{3a}$$

$$p_y = 2 * \tan(\theta_y) / v, \tag{3b}$$

where v is an average time to depth conversion velocity. A graphic representation of p_x is displayed in Figure 5.

Directionally, one can compute apparent dip at any angle ψ from North through a simple trigonometric rotation:

$$p_\psi = p_x \cos(\psi - \phi) + p_y \sin(\psi - \phi), \tag{4}$$

where ϕ is the angle of the inline seismic axis from North.

Marfurt (2006) also describes an amplitude gradient vector attribute that has inline and crossline components (g_x, g_y). We can therefore compute an amplitude gradient at any angle, ψ, from North:

$$g_\psi = g_x \cos(\psi - \phi) + g_y \sin(\psi - \phi). \tag{5}$$

To compute the apparent curvature at an angle, δ, from the azimuth of minimum curvature, χ, one can slightly modify Roberts' (2001) description of Euler's formula:

$$k_\delta = k_{\max} \sin^2 \delta + k_{\min} \cos^2 \delta, \tag{6}$$

where k_{min} and k_{max} are the minimum and maximum curvatures. To compute the apparent curvature at an angle ψ, from North one obtains:

$$k_{\psi} = k_{\max} \sin^2(\psi - \chi) + k_{\min} \cos^2(\psi - \chi) . \quad (7)$$

Using equations 4, 5, and 7, I am able to animate through a suite of apparent dip, amplitude gradient, and curvature images, rotating 360^o from the North, and examine which perspective best illuminates structural features of interest. Figure 6 shows the workflows to generate these attributes.

Curvature

Planar surface is only one special type of geological surface, or reflector. In the real world, geological surfaces are commonly folded (Figure 7).

Geometric description

Curvature at any point, *P*, on a 2D curve is defined by the reciprocal of the radius of the osculating circle, *R*, tangent to the curve at the analysis point (Figure 8). For a 3D surface, we define curvature at a point *P* by fitting two circles within perpendicular planes tangent to that surface at the analysis point (Figure 9). The reciprocal of the radius of these two circles give rise to what are called apparent curvatures. We rotate the two perpendicular planes until we find the circle with the minimum radius. The reciprocal of this radius is defined as the maximum curvature, k_{max}. For a quadratic surface, the tangent circle contained in the plane perpendicular to that with the minimum radius will contain the circle with the maximum radius, whose reciprocal defines the minimum curvature, k_{min}. With the vertical axis being defined as positive down, we will define anticlinal features to have positive maximum curvature, and synclinal features to have negative maximum curvature.

Mathematical description

Fitting a quadratic surface for any point on an analysis surface, with the approximation

$$z(x,y)=ax^2 + by^2 + cxy + dx + ey + f, \quad (8)$$

Based on Rich (2008), one can compute the principal curvatures k_1 and k_2 as the eigenvalues of the quadratic surface:

$$k_1 = \frac{a(1+e^2)+b(1+d^2)-cde+(\alpha-\beta)^{1/2}}{(1+d^2+e^2)^{3/2}}, \quad (9)$$

and

$$k_2 = \frac{a(1+e^2)+b(1+d^2)-cde-(\alpha-\beta)^{1/2}}{(1+d^2+e^2)^{3/2}}, \quad (10)$$

where

$$\alpha = [a(1+e^2)-b(1+d^2)]^2, \quad (11)$$

$$\beta = [2bde-c(1+e^2)][2ade-c(1+d^2)], \quad (12)$$

Most references (in both mathematics and geology) define the maximum curvature to be the greater of absolute of the two principal curvatures, k_1 and k_2 (largest absolute curvature values)

$$k_{\max} = \begin{cases} k_1 \text{ if } |k_1| \geq |k_2| \\ k_2 \text{ if } |k_1| < |k_2| \end{cases}, \quad (13)$$

and minimum curvature to be the smaller of the absolute of the two principal curvatures

$$k_{\min} = \begin{cases} k_2 \text{ if } |k_1| \geq |k_2| \\ k_1 \text{ if } |k_1| < |k_2| \end{cases}. \quad (14)$$

The above definition is related to the definition of the first eigenvalue being the largest in magnitude, regardless of the shape (concave or convex) of the corresponding

eigenvector that best describes a quadratic surface. Roberts (2001) also defines the most-positive and most-negative curvatures

$$k_{pos} = (a+b) + [(a-b)^2 + c^2]^{1/2}, \quad (15)$$

and

$$k_{neg} = (a+b) - [(a-b)^2 + c^2]^{1/2}. \quad (16)$$

In the special case of zero dip, (i.e., at the crest and troughs of synclines and at the top and bottom of domes and bowls, we have $d = e = 0$, such that at these locations only

$$k_{pos}=k_1 \text{ , } (d=0, e=0) \quad (17)$$

and

$$k_{neg}=k_2 \text{ , } \quad (d=0, e=0). \quad (18)$$

Shape index and curvedness

In principal, the geologic structure can be visualized by animating between the two principal curvature k_1 or k_2. A simpler image can be obtained by combining k_1 and k_2 into the shape index, s

$$s = \frac{2}{\pi} \text{ATAN}\left(\frac{k_1 + k_2}{k_1 - k_2}\right), \quad (19)$$

and curvedness

$$c = (k_1^2 + k_2^2)^{1/2} \quad (20)$$

where values of s = -1.0, -0.5, 0.0, +0.5, and +1.0, indicate bowl, valley, saddle, ridge, and dome quadratic shapes (Figure 10). Figure 11 is an example from Chicontepec basin, displaying shape index modulated by curvedness. In the figure, ridge, valley, dome, bowl, and saddle shape are presented.

Curvature Lineaments – Multi-attribute displays and rose diagrams

Combining multiple attributes in a single image allows us to visually 'cluster' mathematically different attributes that are sensitive to the same underlying geology, which in Cuu Long Basin are faults and fracture lineaments. Since the ridge or the valley component of curvature might be related to the up-thrown size or down-thrown side of faults, and minimum curvature azimuth in this case is the strike of these features, I combine these attributes, and represent the results alternatively, as a 2D color display, or as a rose diagram. In Figure 12, I show a composite image of the ridge component of curvedness, c_r,

$$c_r = c \bullet G(s - 0.5), \tag{20}$$

where G is a function of shape index, as plotted in Figure 13, and minimum azimuth of curvature, ψ_{min} from DiamondM field, Texas. The lightness represents the lineament component of curvedness, which in this case is ridge, and hue represents the azimuth of minimum curvature. The black area is where the curvedness is low, or flatter zone.

For a more conventional display of these lineaments, we generate rose diagrams for any defined *n-inline* by *m-crossline* analysis window. Within each analysis window, we threshold the ridge (or valley) components of curvedness, c_r (or c_v), bin within each voxel according to its azimuth, ψ_{min}, and sum the threshold-clipped values of the ridge or valley components, thereby generating volumetric rose diagrams over a suite of windows spanning the entire seismic volume. A 3D rose diagram on a time structure map of top reef from DiamondM field is displayed in Figure 14. In this figure, locations of no lineaments, lineaments increasing, decreasing, rotating, constant, unidirection, bidirection are presented.

Summary

There are many geometric attributes that can be used to interpret geological structure. In this chapter, I have summarized the theory and mathematical foundation for apparent dip, amplitude gradient, curvature, and combinations of curvature attributes such as the shape index with curvedness, ridge curvedness with minimum curvature azimuth in multi-attribute display and rose diagrams. The applications of these methods are presented in the subsequent chapters.

List of Figures

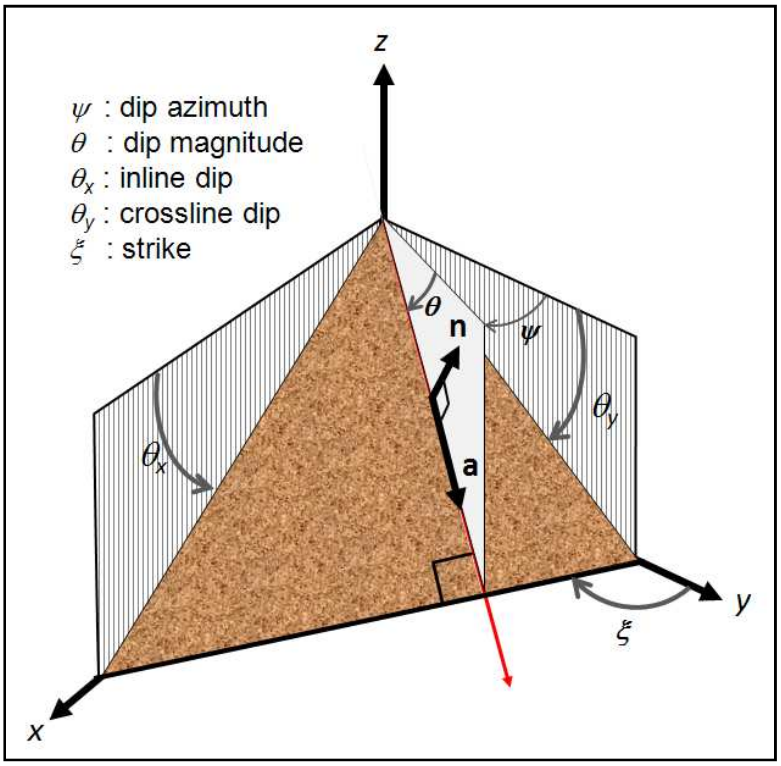


Figure 1: Mathematical definition of a dipping surface. By convention, **n** = unit vector normal to the surface; **a** = unit vector dip along the surface; θ = dip magnitude; ψ = dip azimuth; ξ = strike; θ_x = the apparent dip in the *xz* plane; and θ_y = the apparent dip in the *yz* plane (modified after Chopra and Marfurt 2007).

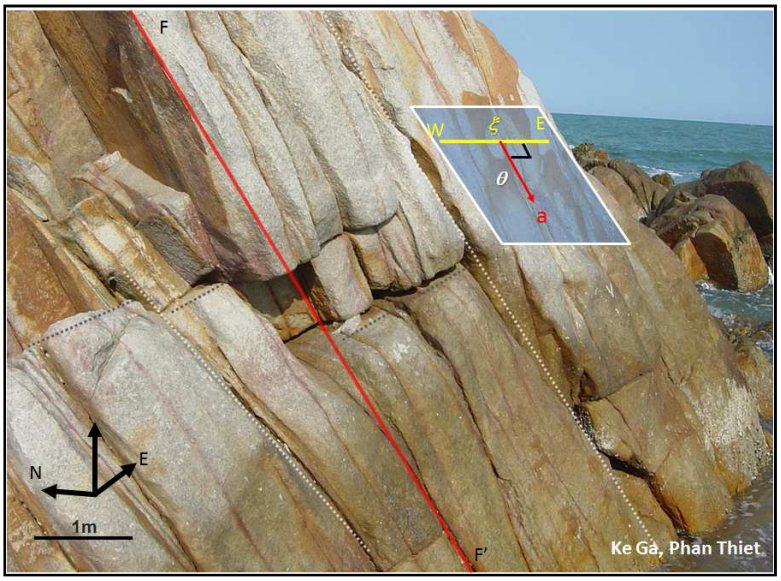


Figure 2: Outcrop of fracture granite basement in Phan Thiet, Vietnam. The exfoliation fracture surface (rectangle) is represented by the strike ξ in E-W direction, dipping θ into the direction of unit vector dip **a** (image courtesy of PetroVietnam).

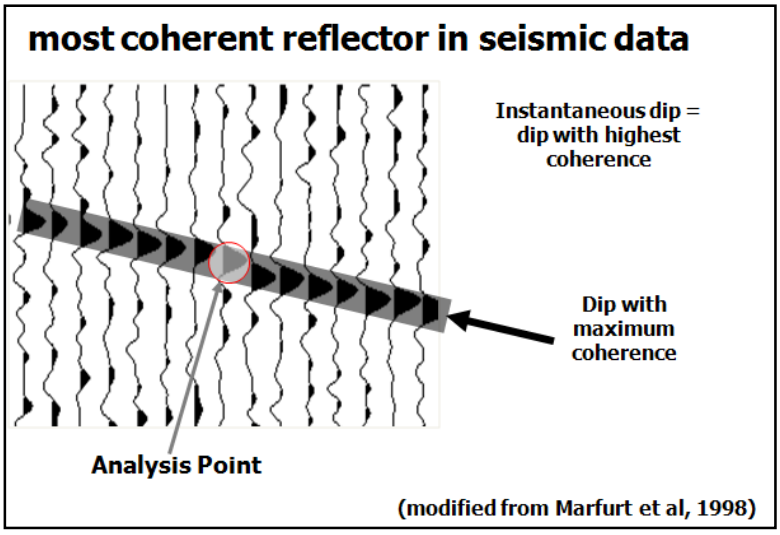


Figure 3: A schematic diagram showing a 2D estimate of coherence. The high coherence response represents a seismic reflector (modified after Marfurt et al. 1998).

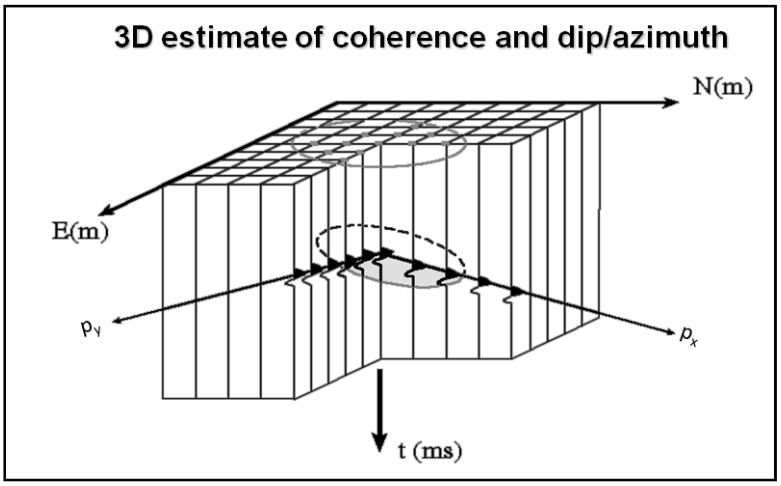


Figure 4: A schematic diagram showing a 3D search-based estimate of coherence, in which p_x indicates the inline and p_y the crossline components of vector time dip (modified after Marfurt et al. 1998).

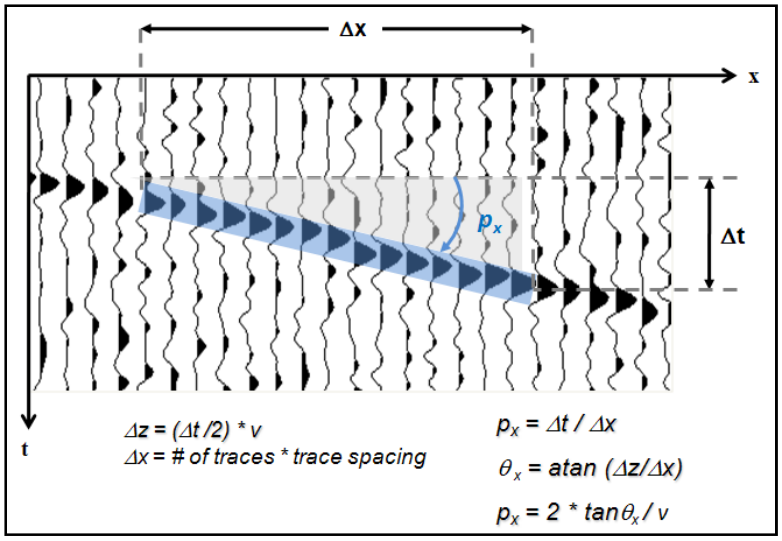


Figure 5: A schematic diagram showing the calculation of seismic reflector dip. θ_x = the apparent dip magnitude in the x direction. p_x = the inline components of vector time dip. v = average time to depth conversion velocity.

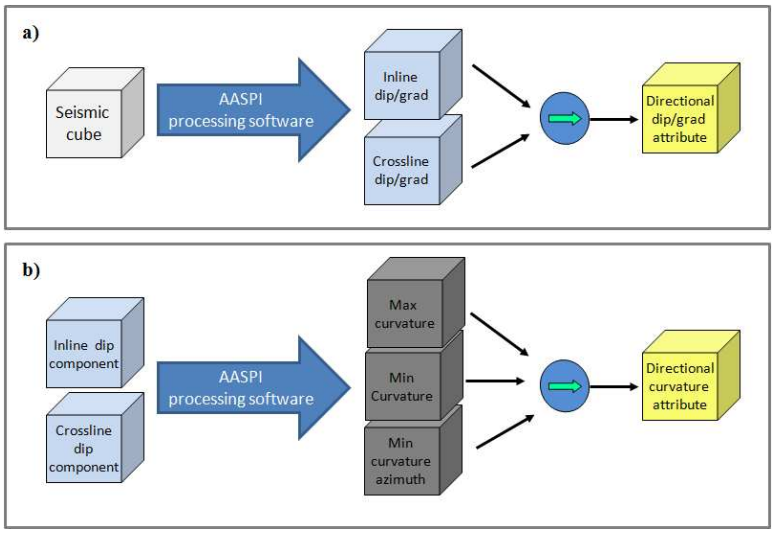


Figure 6: Processing workflow to generate directional attributes. (a) Generating directional dip or amplitude energy gradient attribute from seismic amplitude. (b) Generating Euler curvature attributes from inline and crossline dip attributes.

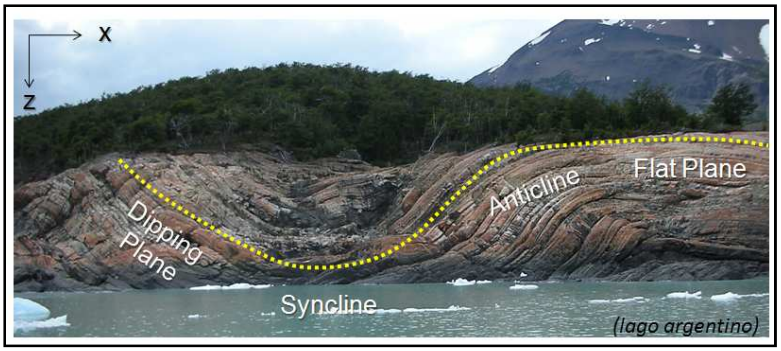


Figure 7: Folding surface, Lago Argentino

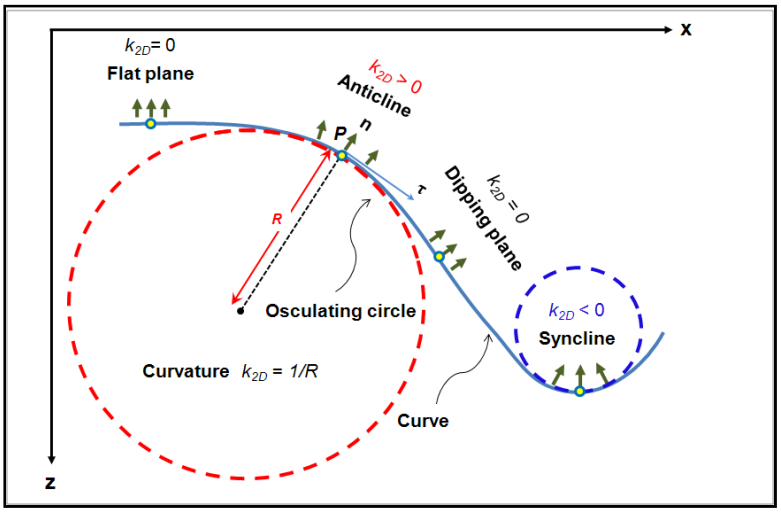


Figure 8: Definition of curvature. For a particular point **P** on a curve, green arrows indicate normal vectors, **n**, to the curve. **τ** is the vector tangent to the curve at point P. Curvature is defined in terms of the radius of the circle tangent to the curve at the analysis point. Anticlinal features have positive curvature (k_{2D}>0), and synclinal features have negative curvature (k_{2D} <0). Planar features (dipping or horizontal) have zero curvature (k_{2D} =0) (modified after Roberts, 2001).

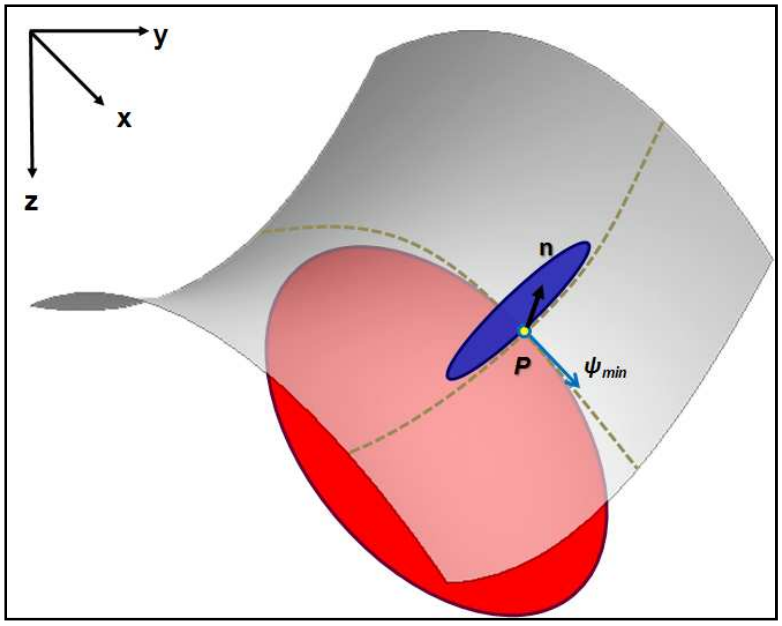


Figure 9: A quadratic surface with the normal, **n**, defined at point *P*. The circle tangent to the surface whose radius is minimum defines the magnitude of the maximum curvature, $|k_{max}| \equiv 1/R_{min}$ (in blue). For a quadratic surface, the plane perpendicular to that containing the previously defined blue circle will contain one whose radius is maximum, which defines the magnitude of the minimum curvature, $|k_{min}| \equiv 1/R_{max}$ (in red). Graphically, the sign of the curvature will be negative if it defines a concave surface and positive if it defines a convex surface. For seismic interpretation, we typically define anticlinal surfaces as being convex up, such that k_{max} has a negative sign and k_{min} has a positive sign in this image.

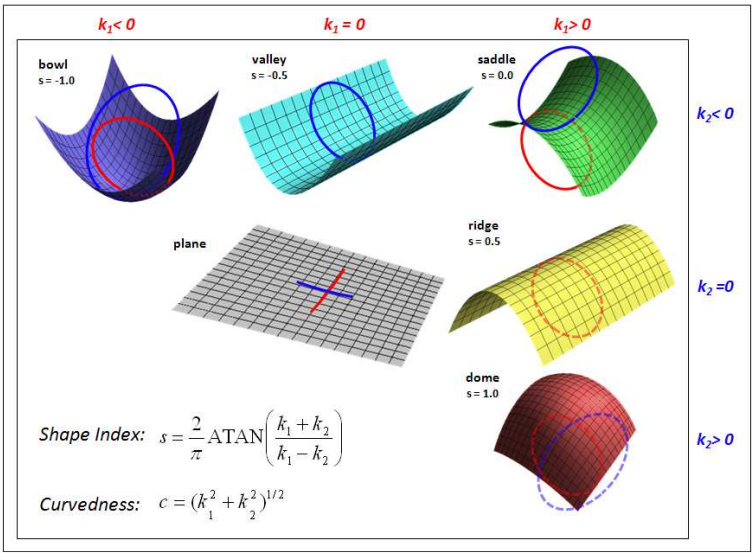


Figure 10: The definition of 3D quadratic shapes expressed as a function of the most-positive principal curvature, k_1, and the most-negative principal curvature, k_2. By definition, $k_1 \geq k_2$. Thus, if both k_1 and k_2 are less than zero, we have a bowl; if both are greater than zero, we have a dome; and if both are equal to zero, we have a plane.

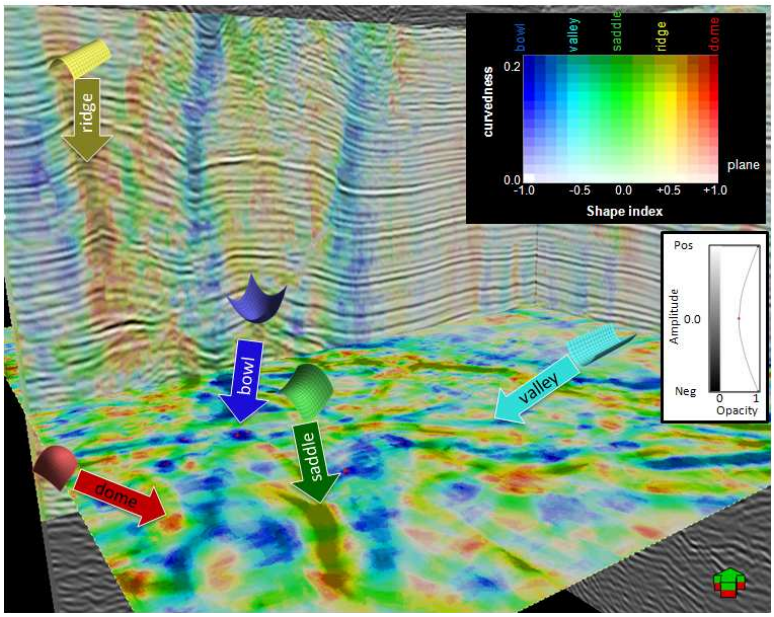


Figure 11: Example of shape index modulated by curvedness. Chicontepec, Mexico.

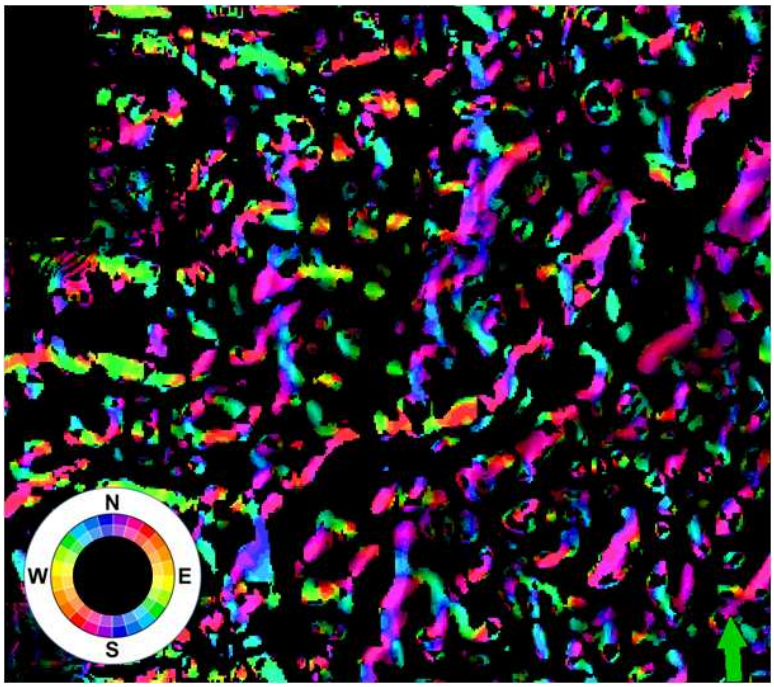


Figure 12: Example of ridge curvedness and the azimuth of minimum curvature composite image, DiamondM, Texas.

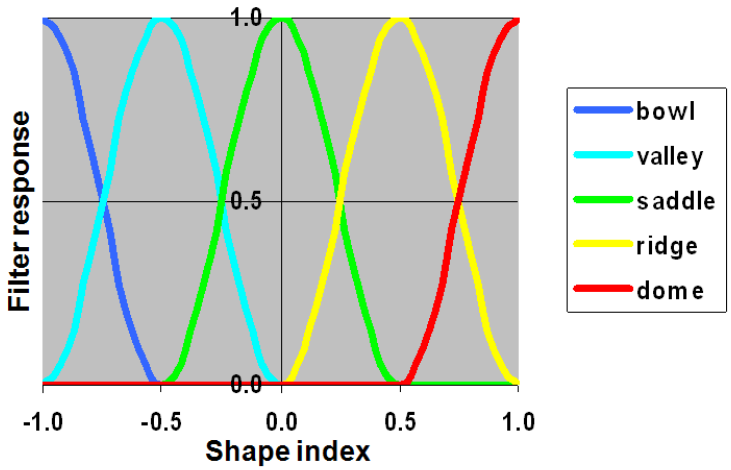


Figure 13: G function of shape components (al-Dossary and Marfurt, 2006)

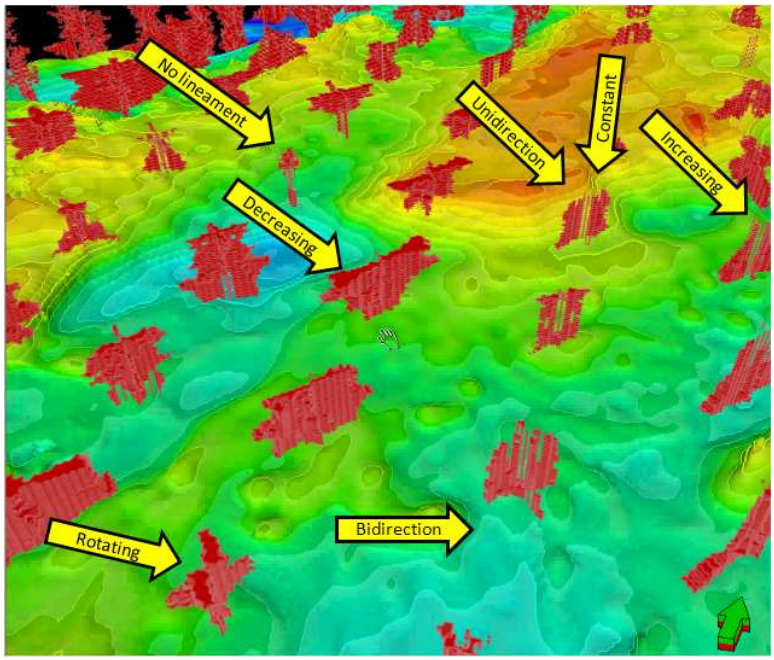


Figure 14: Example of 3D rose diagrams on time structure map, DiamondM, Texas.

References

Al-Dossary, S. and K. J. Marfurt, 2006, 3-D volumetric multispectral estimates of reflector curvature and rotation: Geophysics, **71**, 41-51

Barnes, A. E., 2000, Weighted average seismic attributes: Geophysics, **65**, 275–285.

Blumentritt, C., K. J. Marfurt, and E. C. Sullivan, 2006, Volume-based curvature computations illuminate fracture orientations, Lower-Mid Paleozoic, Central Basin Platform, West Texas: Geophysics, **71**, B159-B166

Chopra, S., and K. J. Marfurt, 2007, Seismic attributes for prospect identification and reservoir characterization: Geophysical Developments **11**, Society of Exploration Geophysicists.

Marfurt, K. J., 2006, Robust estimates of 3D reflector dip and azimuth: Geophysics, **71**, 29-40.

Marfurt, K. J., R. L. Kirlin, S. H. Farmer, and M. S. Bahorich, M. S. 1998, 3-D seismic attributes using a running window semblance-based algorithm: Geophysics, **63**, 1150-1165.

Nissen, S. E., T. R. Carr, K. J. Marfurt, and E. C. Sullivan, 2009, Using 3-D seismic volumetric curvature attributes to identify fracture trends in a depleted Mississippian carbonate reservoir: Implications for assessing candidates for CO2 sequestration, in M. Grobe, J. C. Pashin, and R. L. Dodge, eds., Carbon dioxide sequestration in geological media—State of the science: AAPG Studies in Geology **59**, p. 297–319.

Randen, T., et al., 2000, Three-dimensional texture attributes for seismic data analysis: 70th International Meeting, SEG, Expanded Abstracts, **19**, 668-671.

Rich, J., 2008, Expanding the applicability of curvature attributes through clarification of ambiguities in derivation and terminology: 78th Annual International Meeting, SEG, Expanded Abstract, 884-888.

Roberts, A., 2001, Curvature attributes and their application to 3D interpreted horizons: First Break, **19**, 85-99.

Sigismondi, E. M., and J. C. Soldo, 2003, Curvature attributes and seismic interpretation: Case studies from Argentina basins: The Leading Edge, **22**, 1122-1126.

Sullivan, E. C., K. J. Marfurt, A. Lacazette, and M. Ammerman, 2006, Application of new seismic attributes to collapse chimneys in the Fort Worth Basin: Geophysics, **71**, B111-B119.

Chapter 4 Attributes applied to the Cuu Long Basin, Vietnam

Description

Oil and gas production from fractured granite basement reservoirs plays a very important part in the oil and gas industry of Vietnam, with 85% of crude oil in Vietnam produced from the basement. Due to the complexity of this non-layered type of reservoir, the seismic data quality are very low. The following paper, to be submitted to *Geophysics* journal of Society of Exploration Geophysicists in May 2010, shows how seismic modeling, careful reprocessing, and depth migration followed by attribute analysis can help delineate these important basement fractures.

Enhanced seismic data processing and interpretation for fractured basement in the Cuu Long basin, Vietnam

Ha T. Mai[1], Mai T. Tan[2], Phan T. Vien[3] and Kurt J. Marfurt[1]

[1]The University of Oklahoma, USA
[2]Hanoi University of Mining and Geology, Vietnam
[3]PetroVietnam, Vietnam

ABSTRACT

The fractured granite basement is the primary oil and gas reservoir in the Cuu Long Basin, Vietnam. Due to the complexity of this non-layered target, seismic data quality within the basement is very low. For these reasons, it is important to apply improved seismic data processing workflows to improve the fracture imaging quality.

Our studies in the fractured granite basement of the Cuu Long Basin show that application of τ-p deconvolution and parabolic Radon transforms improves the signal-to-noise ratio by suppressing multiples, thereby revealing the top of the faulted basement. Using a multi-arrival-solution controlled beam migration (CBM) further improves the signal-to-noise ratio, and helps image steeply dipping discrete fracture events. Applying geometric attributes such as apparent dip, energy gradient, and curvature further delineate these faults and fractures. Mapping fracture intensity and orientation assists in delineating sweet spots and aids in planning horizontal wells.

LIST OF KEYWORDS

Cuu Long basin, fractured basement, beam migration, seismic attributes.

INTRODUCTION

The basement of the Cuu Long Basin is composed of pre-Cenozoic granite rocks. They were strongly deformed, fractured by tectonic events, exposed to weathering, and hydrothermally altered. These processes created local structural highs and a network of fractures with sufficient pore space and permeability to form an economic hydrocarbon reservoir.

Due to the complexity and non-layered nature of the structure, the seismic data contain a lot of noise and multiples. It is therefore critical carefully process, filter, and migrate the data to suppress multiples and other noise trains thereby revealing faults and fractures within the upper basement reservoir.

Throughout studies, we see that applying τ-p deconvolution and parabolic Radon transforms do a good job on suppressing noise to signal and removing multiples. Dealing with complicated steeply dipping faults in the area, applying multiple-arrival migration like controlled beam migration helps image events from fractured basements. Calculating geometric attributes, such as apparent dips, energy gradients, and curvature, we can generate shaded-relief maps from orthogonal attributes (Barnes 2003), hence highlighting the faults and features perpendicular to analysis direction. All of these processes help the interpreter to create a better map of the fault and fracture networks, providing better understanding of the basement reservoir, and to design better drilling solutions.

We begin with an overview of the unique geologic play in Cuu Long Basin. Next, we describe a suite of seismic models to better understand fracture illumination and the effectiveness of alternative multiple suppression strategies. We then apply our processing flow to depth migrate the seismic volume. We interpret our images with azimuth-

sensitive attributes to enhance our fractures. We conclude with a discussion on the effectiveness of our workflow.

CHARACTERISTICS OF PRE-CENOZOIC BASEMENT IN CUU LONG BASIN

The Cuu Long Basin is located on the Southeast continental shelf of Vietnam (Figure 1). Figure 2 shows a geological cross-section, indicating the sequence and relative thicknesses of the E, D, C-Lower, Middle and Upper Oligocene, as well as the B-Miocene layers. These sediment sections directly overlay the Pre-Cenozoic basement granite rocks. Tests and production data confirm that a vast reservoir exists in the basement's fractured granite rock, with the pore space containing oil. This target is the main exploration objective in Vietnam (Tan, 1990, 2001).

The structure of the Pre-Cenozoic basement of the Cuu Long Basin is very complex, being composed of magmatic rocks formed at different stages. The main lithology of the basement consists of granites, granodiorites, diorite, quartzite-diorite, and metamorphic rocks. The age of these basement rocks is late Jurassic - early Cretaceous (97-178 Ma). The basement has been deformed and fractured by a number of different factors, including rifting, followed by uplift, weathering and hydrothermal alteration (Figure 3). Tectonomagmatic activities occurred in Jurassic-Cretaceous and ended in mid-Miocene. The combined effects of tectonic deformation and a subsequent diagenesis have produced a fabric that is a mixture of fractures, vugs, forming favorable conditions for hydrocarbon from the Oligocene-Miocene source rocks to migrate and accumulate into the basement highs.

Surface weathering of the granite during exposure to sub-aerial conditions prior to the Oligocene resulted in the development of a zone of porosity enhancement near the top

of the basement. Weathered zones were only detected in a few wells with their thickness varying greatly.

Where present, the weathered zone makes a significantly increase to porosity and well productivity, but its sporadic and restricted development limits the impact on the reservoir performance as a whole. In contrast, the fracture systems in basement rocks created favorable conditions for hydrothermal alteration, and dissolution, confirmed by the presence of secondary minerals such as calcite, zeolite, and quartz encountered in the fractures.

Given these characteristics, the fractured granite basement reservoir in southeast continental shelf of Vietnam is one of the more unusual reservoirs in the world. For this reason, we need to recalibrate seismic processing and interpretation workflows that have been perfected for more traditional reservoirs encountered in layered sedimentary rocks.

SEISMIC MODELING

The pre-Cenozoic granite basement lies at great depth under a thick sediment cover is structurally complex, and lacks a clear bedded character. The porosity of the basement reservoir is composed of fracture porosity (including vuggy and cavern fracture porosity), which differs from the inter-granular porosity seen in sedimentary rocks. The unique characteristics of the Cuu Long basement reservoir require a careful reevaluation and possibly a unique processing, imaging, reservoir characterization, and exploitation workflow. Fagin (1991) found seismic modeling to be an effective tool when encountering new seismic structures and plays.

Based on early Kirchhoff depth migrated images 3D seismic, it was possible to generate a detailed model of the basement oil reservoir. The model was made for the purpose of studying the wave propagation within fractured granite, and provided a basis to

propose an optimum seismic processing sequence. A 2D seismic model representing the fractured basement is shown in Figure 4, where we note that the velocity field varies both vertically and laterally.

The lithology can be represented by a suite of clastic overburden layers overlying the granitic basement. The depth of the top of granite basement ranges between 2km and 6km. Where the upper Oligocene lies directly on top of the basement, the large velocity contrast provides a strong seismic response. Where the lower Oligocene lies on top of basement, the velocity contrast is small, making the signature of the top basement seismically weak.

2D finite difference gathers were simulating using the same source and receiver spacing and frequency as the 3D survey. These models indicate that simple and interbed multiples reflections are originating in the Oligocene mask the much weaker internal basement fracture response,

Figure 5a and 5b show the modeled seismic gathers with and without noise suppression using parabolic Radon filters. Note that the basement diffraction signal is overprinted by high amplitude multiples (Vien, 2003).

SEISMIC PROCESSING AND IMAGING

Given the findings from our model study, we are able to perfect our processing and imaging workflow. Although Sonic log measurements show the granite matrix velocity to be between 5.4-6.0 km/s, some imaging studies found that a velocity of 4.6 km/s was more applicable for the migration and stacking response of the intra-granite fractures. The initial velocity model was built on this premise.

Velocity updating was performed using tomography, based on residual curvature analysis of common image gathers. While this method successfully handled the

overburden clastics, defining the velocity for the deeper zone was difficult because of the weaker primary reflectivity, remnant multiple contamination and the general insensitivity of the method to velocity perturbations at depth.

To continue the velocity update into the E-Sequence and Basement, a stacking velocity sweep method was used. The interpreted Top E horizon was fixed as the upper boundary of the stack sweep. The velocity field above the Top E remained static, while the velocity field below Top E was smoothed and used as the reference velocity. Percentage variations around this reference velocity were calculated, generating a total of seven different velocity models to be input into migration – in this case, beam migration, thus generating seven controlled beam migration (CBM) stacks. The seven stacks were analyzed at each location and depth, and the preferred stack response picked as one would for any velocity analysis. The criterion for picking was based on both the quality of the signal and the geologic plausibility of the structure. After all locations were analyzed, the pick were smoothed and input into 3D tomography to compute the final velocity.

ENHANCEMENTS OF THE STUDIES IN FRACTURED BASEMENT

In order to enhance the data quality and imaging of the fractured basement in the Cuu Long Basin, we used τ-p deconvolution and parabolic Radon transforms to model and remove multiple reflections, thereby revealing the weaker diffractions from the fracture basement. We used controlled beam migration to image steeply dipping fault and fracture plane events. Finally, we used seismic attributes to further delineate and map our fractures.

Radon and τ-p filters

Our model study shows that there are many types of multiples with different nature and characteristics that affect the quality of the processed data. Two types of multiples are particularly important: high amplitude surface related multiple reflections from a number of strong reflection surfaces, and internal multiples between the strong reflection surfaces of the Lower Miocene, Oligocene, and top Basement. We find that τ-p deconvolution and parabolic Radon transforms do a good job in enhancing the signal-to-noise ratio, allowing us to image the diffraction signals from the fractured basement.

Based on their properties, multiple suppression methods can be based on either prediction criteria or on NMO differential. In the Cuu Long Basin, the primary reflections in the deep part of the section are normally weak, compared to multiple energy left after applying predictive deconvolution before stack on far-offset traces.

In general, multiples seen on far offset traces lose the periodicity seen in near offset traces. Treitel et al. (1982) showed that this periodicity can be preserved and thereby exploited in the τ-p domain to suppress multiples. Multiples from the shallow section often have a greater move-out than primaries arriving at the same time. Hampson (1986) showed that parabolic Radon transforms can effectively model such events, which can then be subtracted from the original data.

Internal reflections generated between reflection surfaces of the Lower Miocene and Oligocene are commonly characterized by a considerable residual normal move out. Unlike F-K demultiple filters, the Radon filter attempts to more equally suppress multiples for all traces including near- and far-offset traces. Figures 6a and 6b show prestack time migrated images without and with τ-p deconvolution and parabolic Radon transform filtering (Tan, 2001; Vien, 2003). We note that after effectively eliminating

multiples by the τ-p deconvolution and parabolic Radon transforms processes, signals from the basement are visible.

Improvements in Seismic Imaging in Fractured Basement

Both Kirchhoff and controlled beam migration (CBM) were used in the final pre-stack depth migration. Kirchhoff migration was run to image the shallow section and to facilitate any possible AVA analysis, while controlled beam migration was used to image the top of granite basement and the fracture zones inside the basement.

Controlled beam migration has an advantage of enhancing the signal-to-noise ratio, particularly for steeply dipping events. In a medium of complex velocity, a subsurface point may have multi-arrival ray paths. Since conventional Kirchhoff migration is a single-arrival migration algorithm, only one of several multi-arrivals is imaged, depending on certain predefined criteria. The remaining events are ignored, which can result in poor imaging. Wave equation migration does not use ray paths to represent the propagation of wave fronts, and thus accounts for all arrivals, and in general, produces cleaner images. However, it does not image steeply dipping events such as our fault and fracture planes.

Controlled beam migration has the advantage of both the Kirchhoff migration and wave equation migration. It can handle multi-arrival ray paths, and preserve steeply dipping reflection, resulting in a cleaner image (Raz, 1987; Sun, 2000; Hill, 2001; Bone et al., 2008). A good review of CBM with applications to this survey can be found in Gray (2009)

Figures 7 and 8 show a comparison of the Kirchhoff migration and the CBM migration on vertical and depth slices. The intra-basement events that were barely visible in Kirchhoff migration are clearly imaged with CBM.

The improvement in imaging allows a better understanding of the orientation, spacing and potential connectivity of the fracture zones within the basement. It also helps further attribute analysis and fault interpretation within the basement, and improves our confidence in targeting development well trajectories, and thus assists in optimizing productivity.

Attribute illumination of basement faults

Geometric attributes such as coherence and curvature have been very successful in delineating faults in sedimentary basins. Because of the absence of stratified, coherent reflectors, illumination of basement faults is more problematic than illumination of faults within the sedimentary column. In order to address these limitations we make simple modifications to well-established vector attributes including structural dip and azimuth and amplitude energy gradients to provide greater interpreter interaction (Mai et al., 2009).

Barnes (2003) showed how volumetric estimates of structural dip and azimuth can be used to generate shaded-relief volumes. Based on this idea, we could mathematically generate simple axis rotations and project the two orthogonal dip or energy gradient components along the surface against the direction of illumination.

A planar surface such as a dipping horizon or fault can be presented by its true dip azimuth, θ, and strike, ψ. The true dip θ can be presented by apparent dips θ_x and θ_y along the *x* and *y* axes (Figure 9).

For time-migrated seismic data, it's more convenient to measure apparent seismic time dip components along inline (p_x) and crossline (p_y) directions in *s/ft* or *s/m*. For depth-migrated seismic data such as our Cuu Long survey, we simply compute θ_x and θ_y.

There are several popular means of computing volumetric dip components, including those based on weighted versions of the instantaneous frequency and wave-numbers (Barnes, 2000), on the gradient structure tensor (Randen et al., 2000) and on discrete semblance-based dip searches (Marfurt, 2006).

We can compute apparent dip at any angle ψ from North through a simple trigonometric rotation

$$p_\psi = p_x \cos(\psi - \phi) + p_y \sin(\psi - \phi), \quad (1)$$

where ϕ is the angle of the inline seismic axis from North.

Marfurt (2006) also describes an amplitude gradient vector attribute that has inline and crossline components (g_x, g_y). We can therefore compute an amplitude gradient at any angle, ψ, from North:

$$g_\psi = g_x \cos(\psi - \phi) + g_y \sin(\psi - \phi). \quad (2)$$

Using equations 1 and 2, we are able to animate through a suite of apparent dip, amplitude gradient images at increments of 30^O to see which perspective best illuminates structural features of interest.

Results

We begin by computing apparent dip and energy-weighted amplitude-gradient methods, near the top of basement (Figure 10).

Figure 11 shows depth slices at the top of basement level (2850 m) through the apparent dip volume, p_ψ, as a function of azimuth, using equation 1 for ψ = 0^O, 30^O, 60^O, 90^O, 120^O, and 150^O. White arrows indicate the major NE-SW trending main faults. Red arrows indicate subtle faults running NE-SW and cutting into the basement. Yellow arrows indicate the faults that cut across the basement, in the N-S and NW-SE directions.

The reflector dip enhances different lineament features as the direction of illumination is rotated, as we can see by comparing Figures 11a and 11c. Since the dip attribute measures the dip of a reflector surface, the dip attribute computed on or near the top of basement reveals lineaments well. However, if we look deeper inside the basement, the dip estimates become noisier, making it harder to interpret the results (Figure 12).

In contrast, amplitude gradients are computed along local dip and better delineate high energy cross cutting fractures. Apparent amplitude energy gradient results were generated at the illumination direction ψ = 0^O, 30^O, 60^O, 90^O, 120^O, and 150^O from the North. Figure 13 shows depth slice at 3100 m cutting through the top of the granite basement. White arrows indicate lineaments that we interpret to be indicative of the major NE-SW trending faults that run along the boundary of basement top. Red arrows indicate subtle faults running NE-SW and cutting into the basement. Yellow arrows indicate the faults that cut across the basement, in N-S and NW-SE direction.

By rotating the direction of illumination, the apparent energy gradients enhance the signature of faults or fractures that are perpendicular to the illumination direction. At the apparent direction of 0^O and 150^O, we see NE-SW fractures (Figures 13a and 13f), while at 60^O and 90^O, we see N-S or NW-SE fractures.

CONCLUSIONS

The discovery of oil bearing reservoir in the fractured zones in basement rocks has opened a new trend for oil and gas prospecting in Vietnam. The reservoirs in basement are weathered rocks formed under the influence of tectonic deformation, hydrothermal alteration, and weathering processes. Highly fractured zones with good reservoir properties are usually concentrated in the basement highs, controlled by regional faults.

Seismic modeling in Cuu Long Basin shows that the signal from the basement consists of weak diffractions masked by a strong coherent noise. Multiple reflections in particular significantly reduce the signal-to-noise ratio in the deeper parts of the section. These model studies provide guidance in selecting an effective processing methods and parameters to improve the seismic imaging of the fractured basement in Cuu Long Basin. We found τ -p deconvolution and Radon parabolic transform enhances our signal-to-noise ratio, allowing us to image the diffracted fractured basement signal.

Controlled beam migration effectively images the top basement and intra-basement events. The image quality of CBM is clearly superior to that of Kirchhoff migration. Considerable care and multiple CBM iterations are necessary to correlate with well logs, in order to provide an accurate migration result.

Volumetric attributes such as dip and amplitude energy gradients, are multi-component in nature and are thus amenable to visualization from different user-controlled perspectives. By defining a suite of azimuths to investigate, the interpreter can enhance subtle faults and fractures that might otherwise be missed, or that are more likely to be open rather than sealed.

ACKNOWLEDGMENTS

Thanks to PetroVietnam for granting the research, and permission to publish the results used in this report. Thanks to the sponsors of OU Attribute-Assisted Seismic Processing and Interpretation (AASPI) consortium. We also thank our colleagues in Vietnam Petroleum Institute, Hanoi University of Mining and Geology, University of Oklahoma for ideas, recommendations, and support on the research.

REFERENCES

Barnes, A. E., 2000, Weighted average seismic attributes: Geophysics, **65**, 275–285.

Barnes, A. E., 2003, Shaded relief seismic attribute: Geophysics, **68**, 1281–1285.

Bone, G., N. T. Giang, D. N. Quy, V. N. An, D. Pham, J. Sun, J. Sun, and Q. Tang, 2008, Improvements in seismic imaging in fractured basement, Block 15-1, Offshore Vietnam: Fractured Basement Reservoir, PetroVietnam, 63-69.

Chopra, S., and K. J. Marfurt, 2007, Seismic attributes for prospect identification and reservoir characterization: Geophysical Developments **11**, Society of Exploration Geophysicists.

Fagin. S.W., 1991, Seismic modeling of geologic structures: Applications to Exploration problems: Geophysical Development, **2**, SEG, 3-92.

Grey S. H., Y. Xie, C. Notfors, T. Zhu, D. Wang, and C. Ting, 2009, Taking apart beam migration, The Leading Edge, **28**, 1098-1108

Hampson, D., 1986, Inverse velocity stacking for multiple elimination: Journal of the Canadian Society of Exploration Geophysicists, **22**, 44–55.

Hill, N. R., 2001, Prestack Gaussian-beam depth migration: Geophysics, **66**, 1240-1250.

Mai, H. T., and K. J. Marfurt, 2009, Attribute illumination of basement faults, examples from Cuu Long Basin basement, Vietnam and the Midcontinent, USA: PetroVietnam Journal, June, 10-20.

Marfurt, K. J., 2006, Robust estimates of 3D reflector dip and azimuth: Geophysics, **71**, 29-40.

Randen, T., E. Monsen, C. Signer, A. Abrahamsen, J. O. Hansen, T. Sæter, J. Schlaf, L. Sønneland, 2000, Three-dimensional texture attributes for seismic data analysis: 70th International Meeting, SEG, Expanded Abstracts, **19**, 668-671.

Raz. S., 1987, Beam stacking: a generalized preprocessing technique: Geophysics, **52**, 1194-1210.

Sun, Y., F. Qin, S. Checkles, J. P. Leveille, 2000, 3D prestack Kirchhoff Beam Migration for depth imaging: Geophysics, **65**, 1592-1603.

Tan, M. T., 1990, The enhancement of seismic prospecting effectiveness for oil and gas under the conditions of the sedimentary basins in the continental shelf of Vietnam: Applied Geophysics, **6**, No. 1323.

Tan, M. T., and N. Q. Thap, 2001, The Possibility of Applying Geophysical Methods to Study Fractured Basement Reservoir in the Continental Shelf of Vietnam: Offshore Technology Conference, Proceedings, OTC 13227.

Treitel S., P. R. Gutowski, D. E. Wagner, 1982, Plane-wave decomposition of seismograms, Geophysics, **47**, 1375-1401.

Vien, P. T., 2003, Some remarks on Seismic data processing in Cuu Long Basin: Vietnam Petroleum Institute Conference, Proceedings, 129-141.

LIST OF FIGURES



Figure 1: Cuu Long basin in the Southeast Continental shell of Vietnam (image courtesy of PetroVietnam).

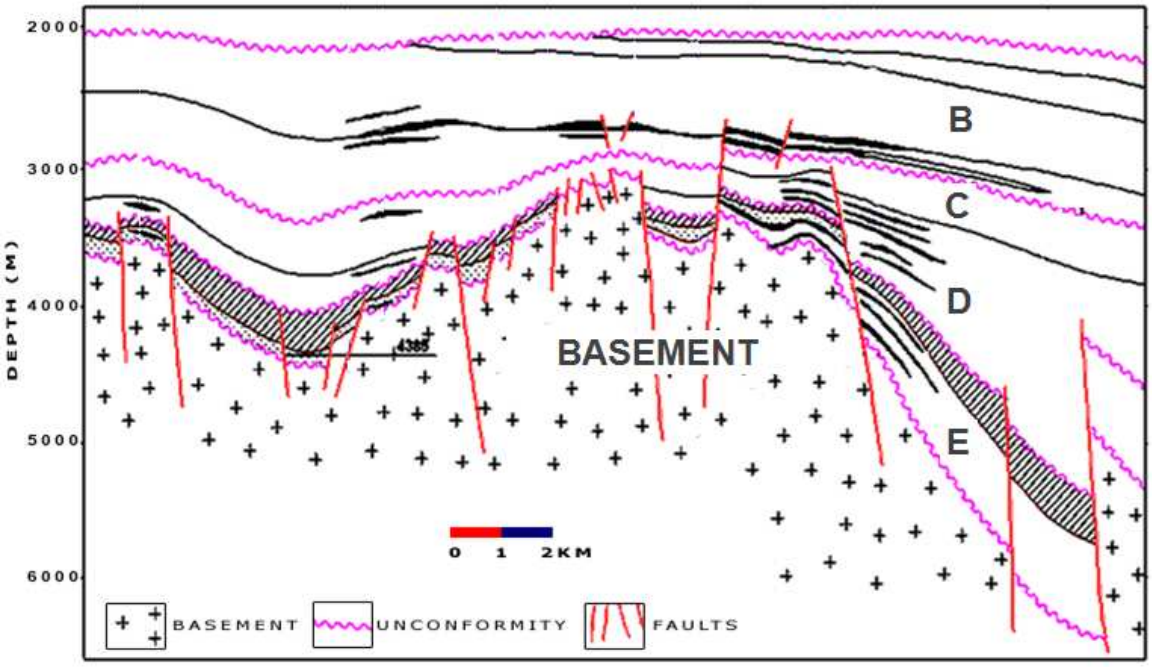


Figure 2: Geological cross section, Cuu Long basin.

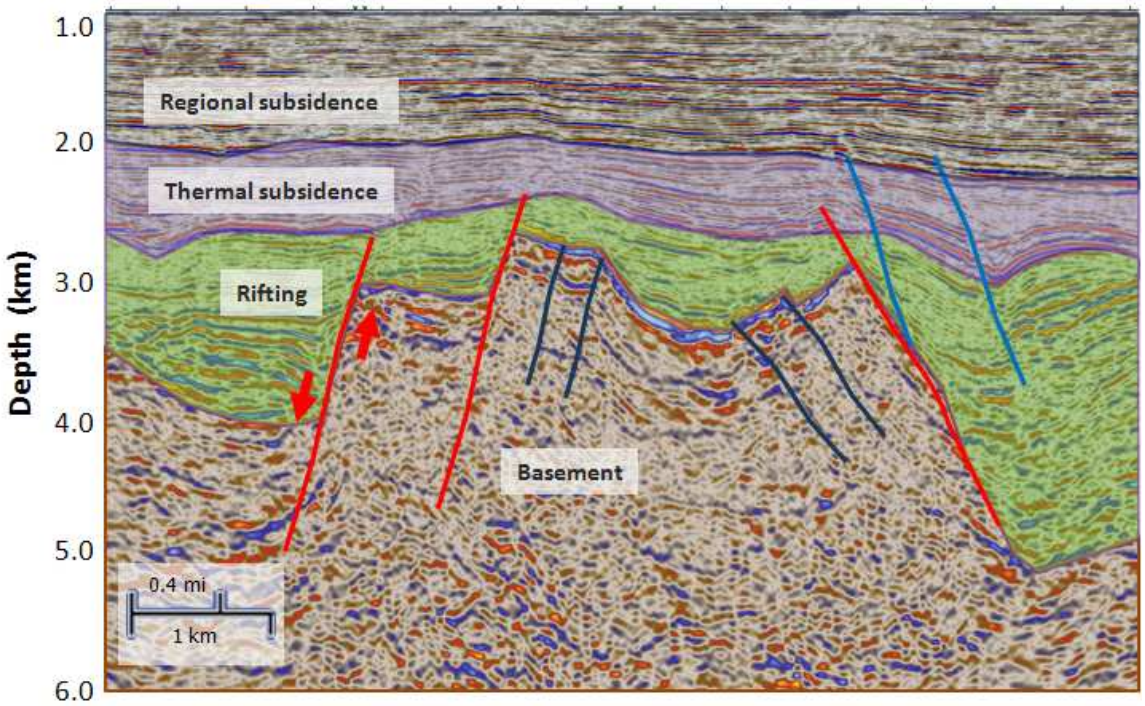


Figure 3: Seismic cross section showing fractures and faults inside granite basement, generated during rifting of the basin.

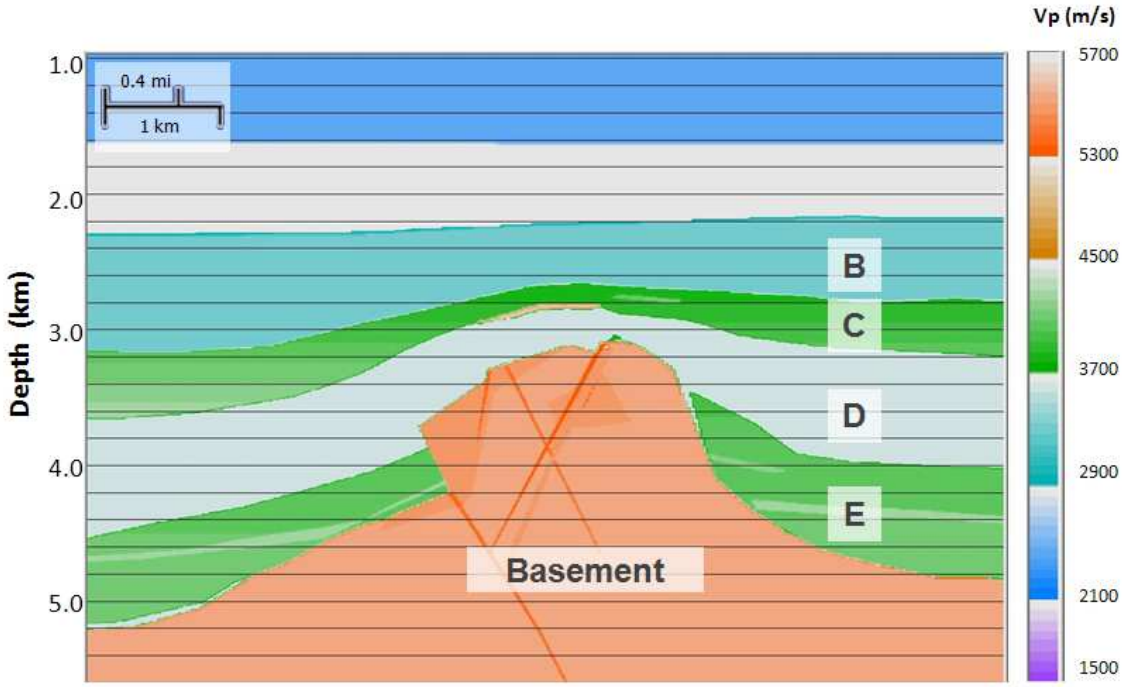


Figure 4: Seismic model representing fractured basement in Cuu Long Basin.

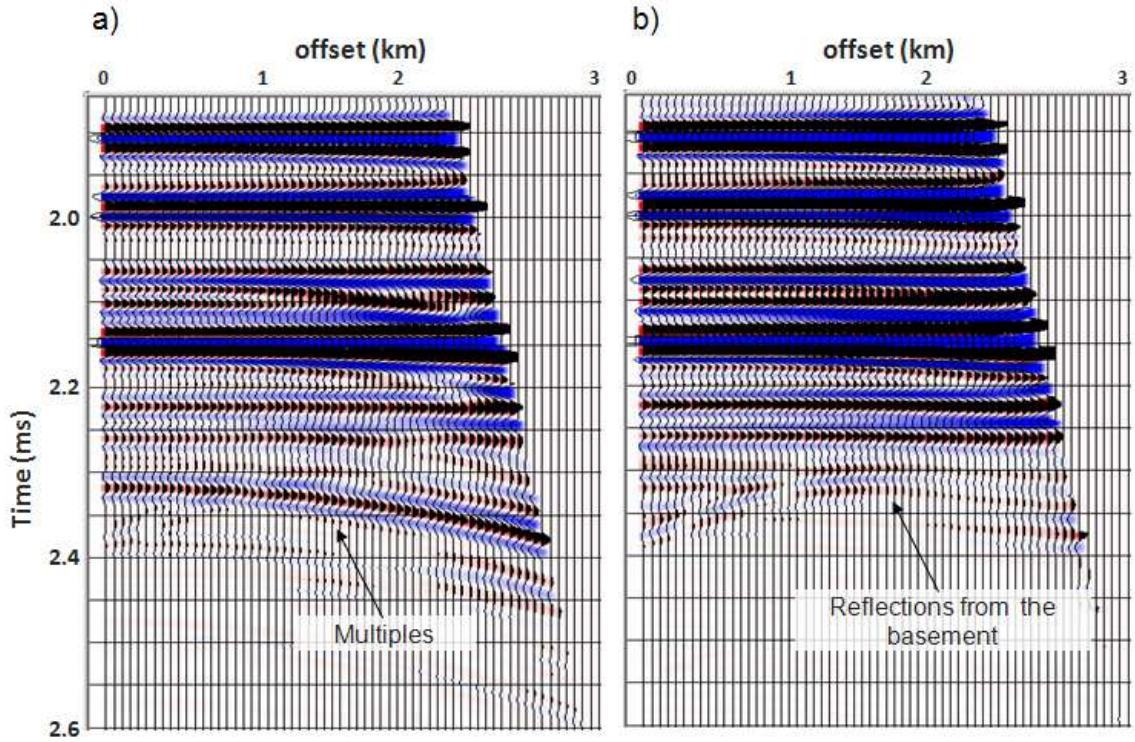


Figure 5: Modeled gather (a) before and (b) after application of parabolic Radon filter.

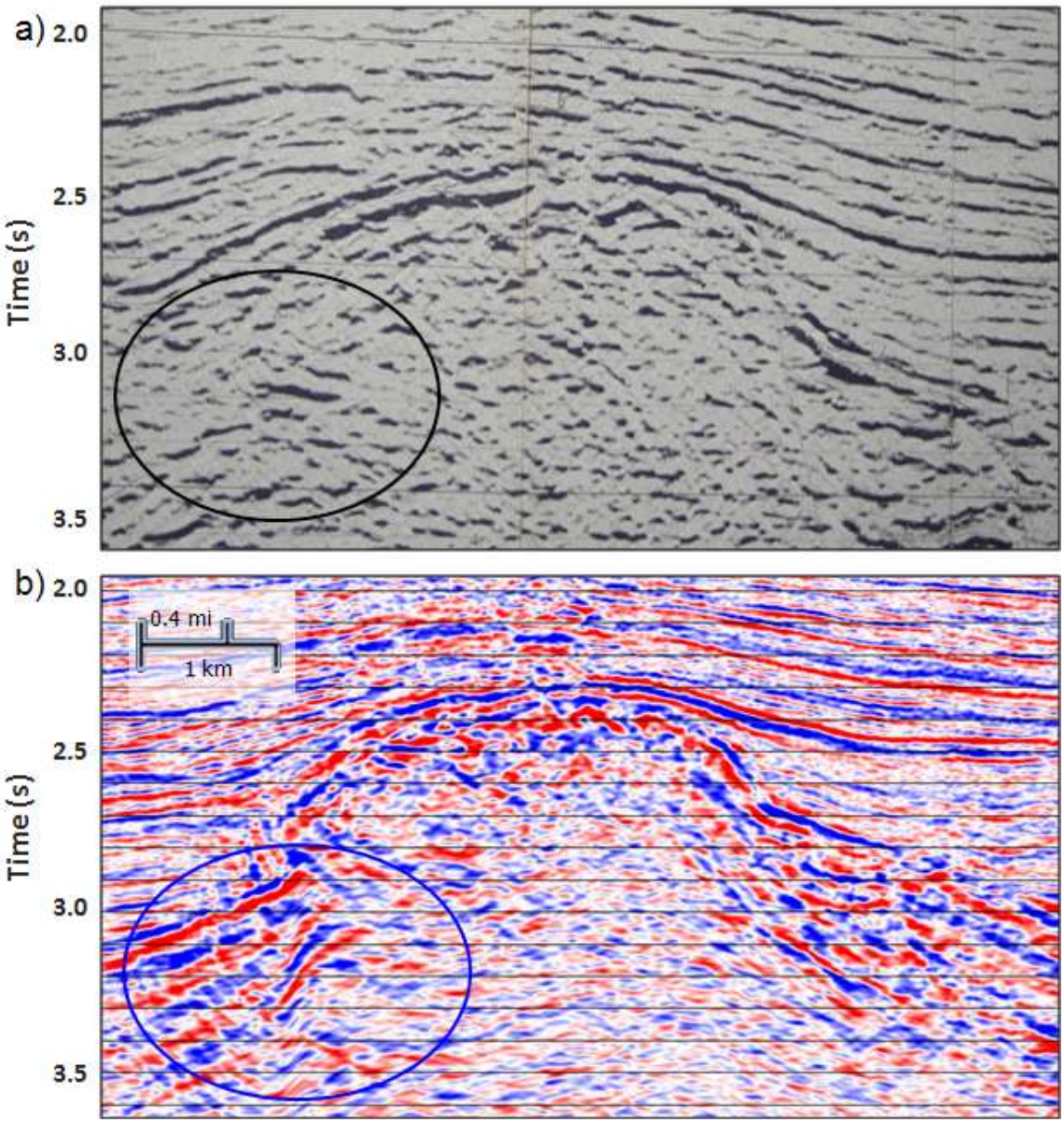


Figure 6: Time-migrated seismic section showing the basement (a) before and (b) after re-processing with Radon and τ-p filters applied.

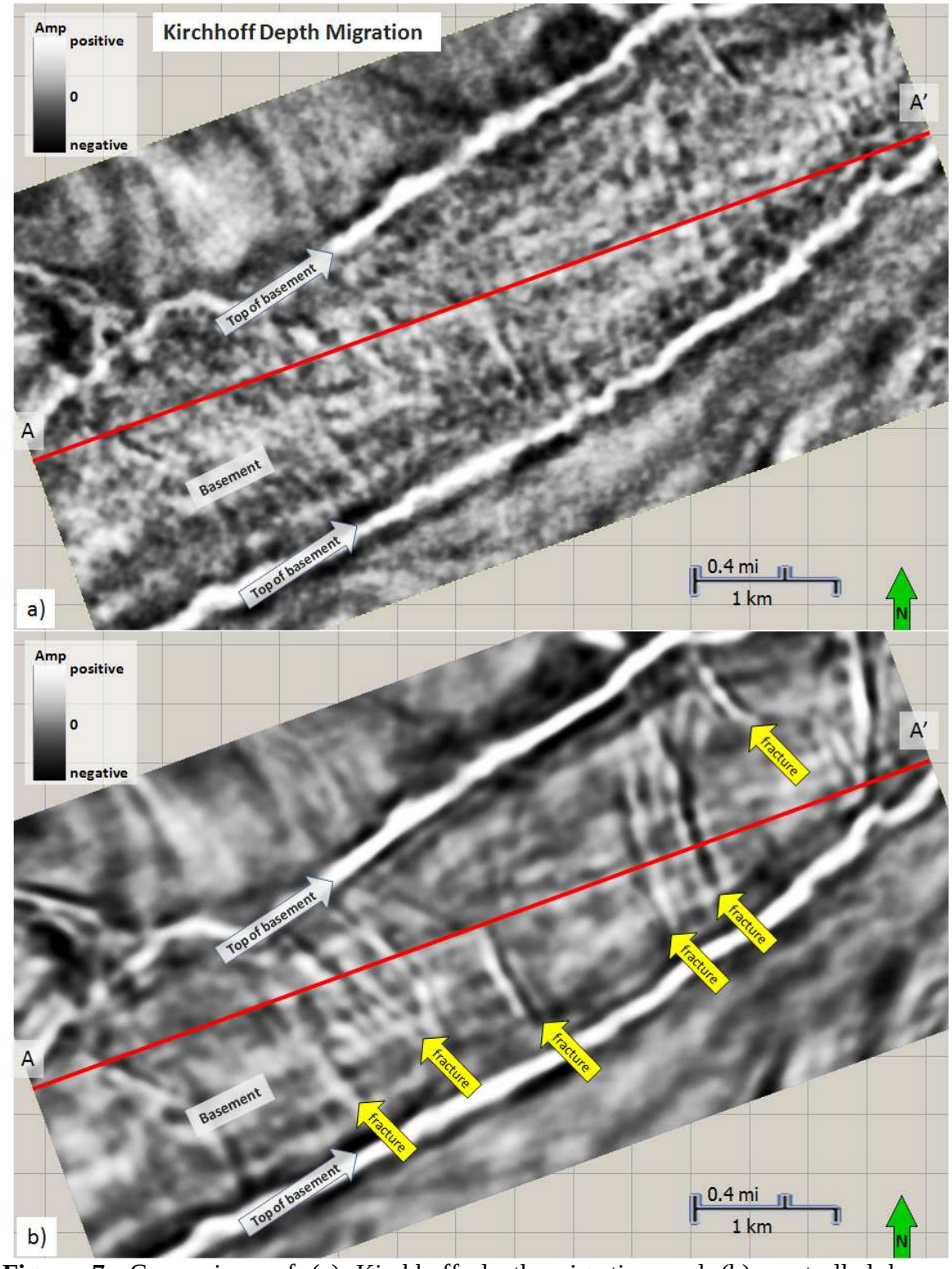


Figure 7: Comparison of (a) Kirchhoff depth migration and (b) controlled beam migration on depth slice at *z*=3100m. Line AA' shown in Figure 8. While the lateral resolution is slightly lower, the controlled beam migration much better indicates the fractures.

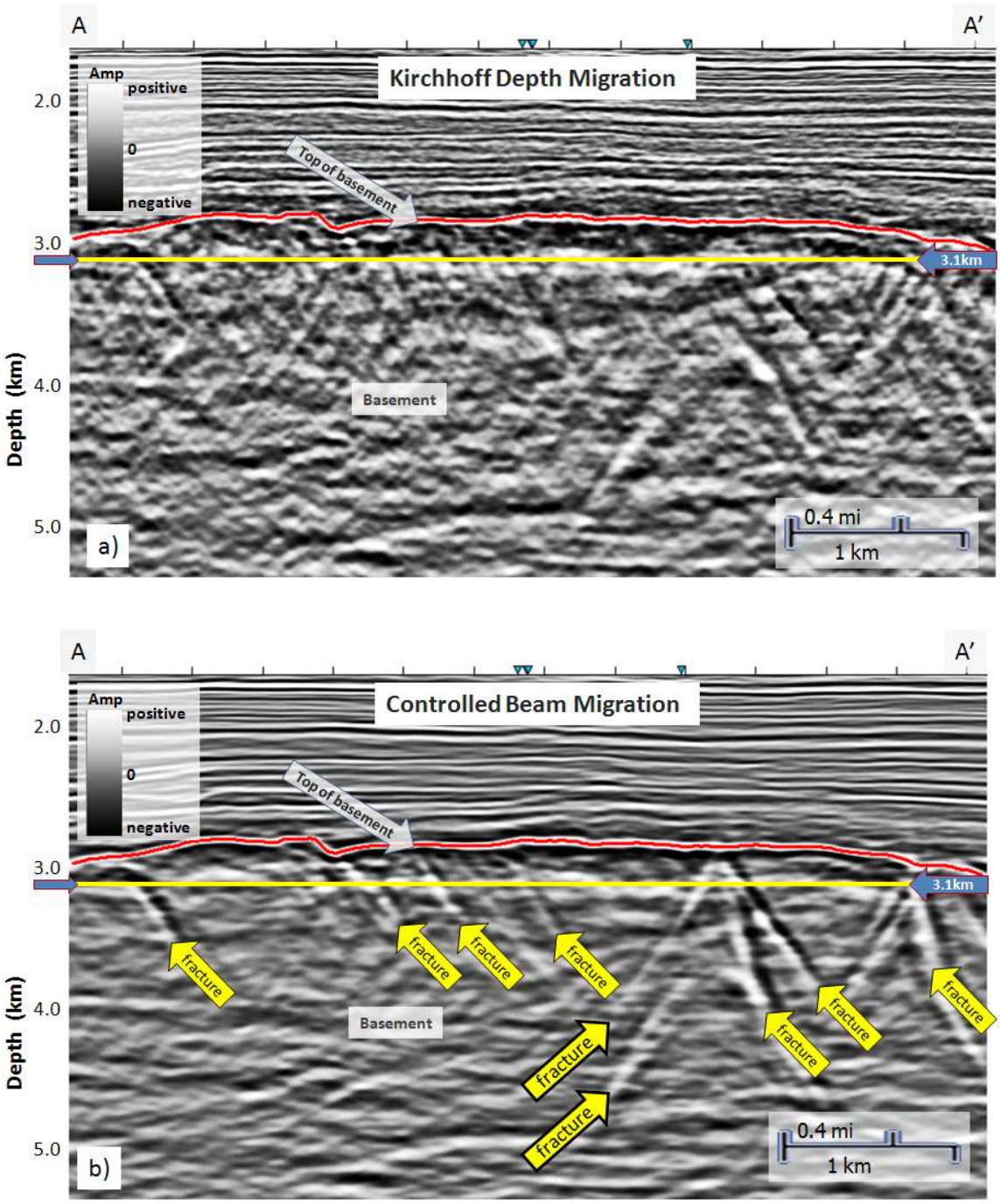


Figure 8: Comparison of (a) Kirchhoff depth migration and (b) controlled beam migration on a vertical seismic section. Yellow line indicates location of depth slice displayed in Figure 7.

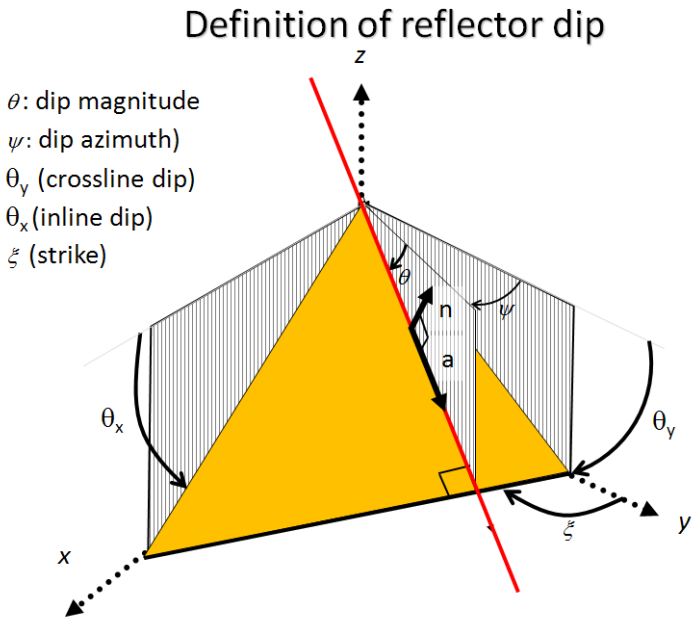


Figure 9: Mathematical, geologic, and seismic nomenclature used in defining reflector dip. By convention, **n** = unit vector normal to the reflector; **a** = unit vector dip along the reflector; θ = dip magnitude; ψ = dip azimuth; ξ = strike; θ_x = the apparent dip in the *xz* plane; and θ_y = the apparent dip in the *yz* plane (after Chopra and Marfurt 2007).

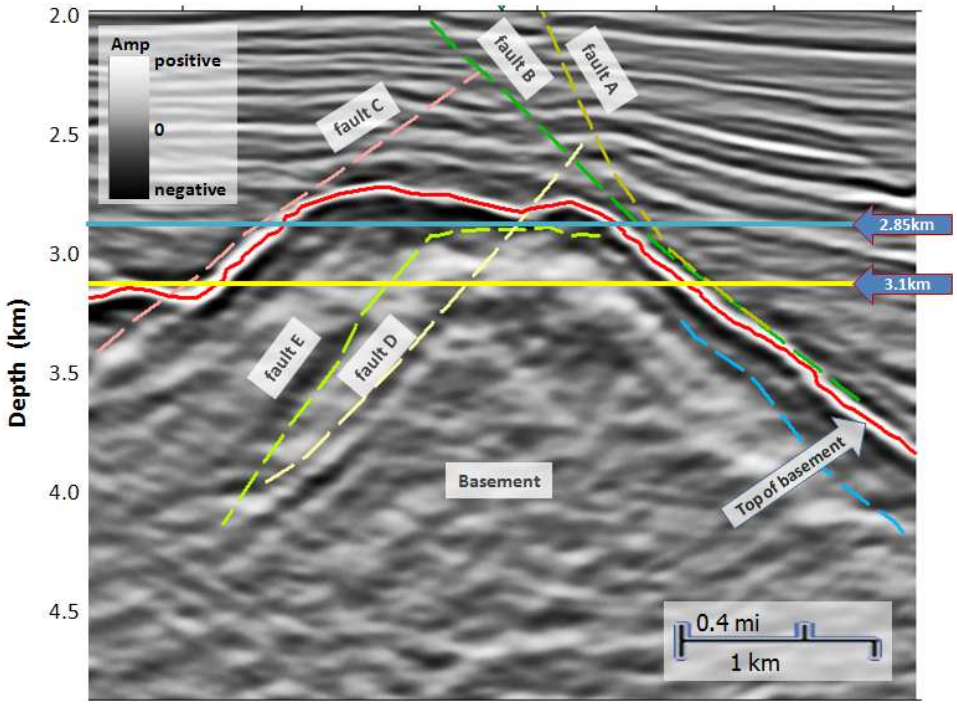


Figure 10: Vertical seismic section showing top of basement and interpreted faults. Depth slices shown in Figure 11-13 are indicated in green and yellow lines.

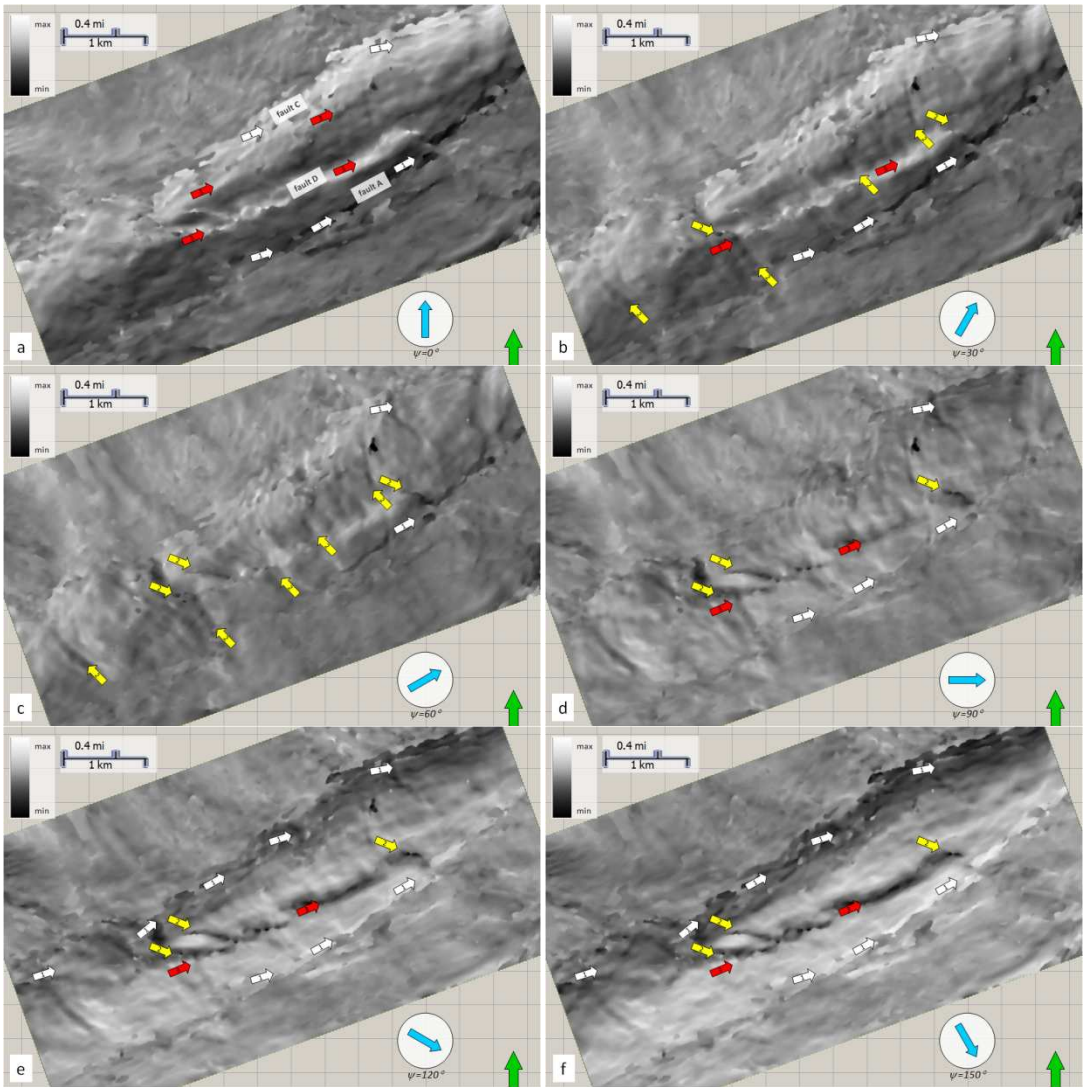


Figure 11: Depth slices at z=2850 m through apparent dip, p_{ψ}, computed at apparent direction ψ=0^{O}, 30^{O}, 60^{O}, 90^{O}, 120 ^{O}, and 150^{O} from North. White arrows indicate lineaments were interpreted as main NE-SW faults running along basement top. Red and yellow arrows indicate faults and fractures within basement.

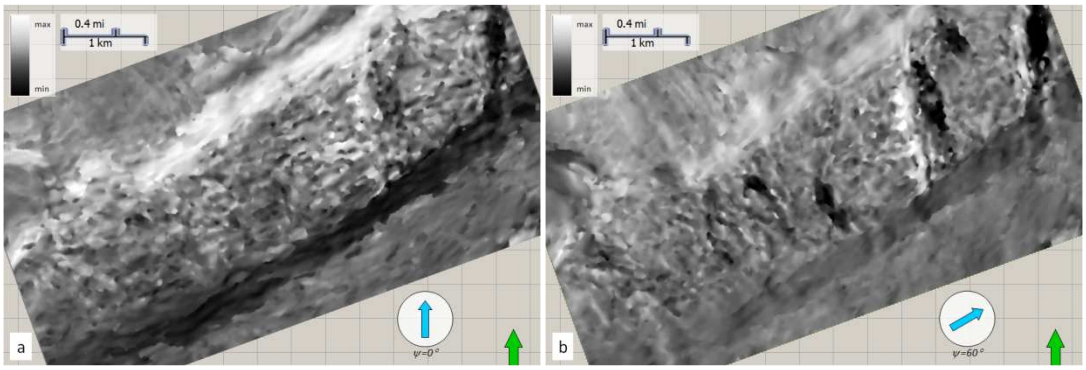


Figure 12: Depth slices at z=3100 m through apparent dip, p_{ψ}, computed at apparent direction ψ=0^{O} and 60^{O} from North.

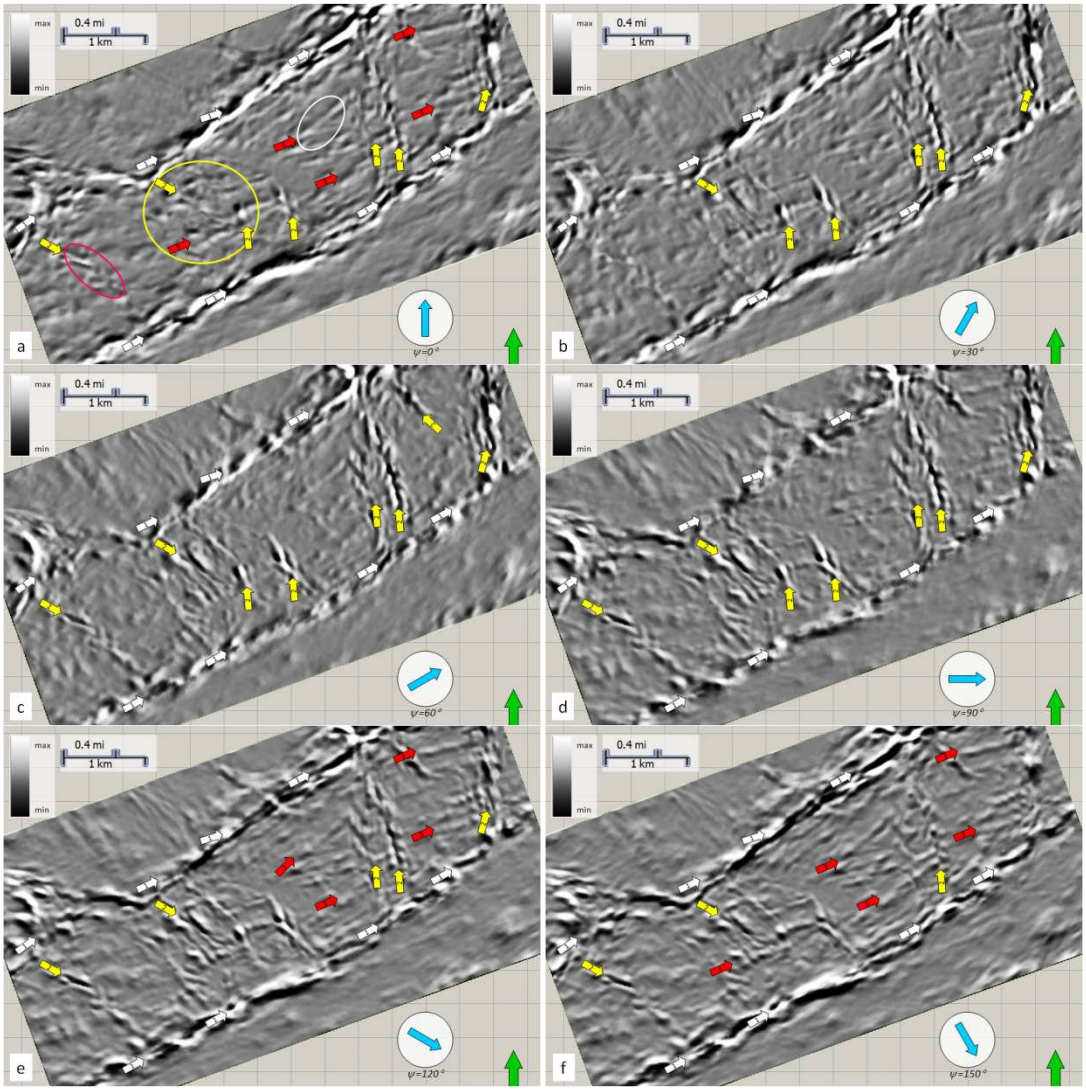


Figure 13: Depth slices at z=3100 m through apparent amplitude gradients, $g\psi$, computed at apparent direction ψ=0^{O}, 30^{O}, 60^{O}, 90^{O}, 120^{O}, and 150^{O} from North. White arrows indicate lineaments were interpreted as main NE-SW faults running along basement top. Red and yellow arrows indicate faults and fractures within basement.

Chapter 5 Attributes applied to the Chicontepec basin, Mexico

Description

Geometric attributes such as coherence and volumetric curvature are commonly used in delineating faults and folds. While fault patterns seen in coherence and principal curvature measures are easily recognized on time slices, they are often laterally shifted from each other. The kind and degree of lateral shift is an indication of the underlying tectonic deformation. This tutorial chapter illustrates some of the lateral relationships between coherence and the various curvature measures in order to give a better understanding of tectonic environment based on seismic attributes. The dataset used in this research is from a high-quality, structurally-complex 3D survey acquired within the Chicontepec basin, Mexico.

The paper is to be submitted to *Geophysics* journal of Society of Exploration Geophysicists in May 2010.

Attribute-aided interpretation of complex structures, an example from the Chicontepec basin, Mexico

Ha T. Mai, Kurt J. Marfurt, University of Oklahoma, Norman, USA
Sergio Chávez-Pérez, Instituto Mexicano del Petróleo

ABSTRACT

Geometric attributes such as coherence and volumetric curvature are commonly used in delineating faults and folds. While fault patterns seen in coherence and principal curvature measures are easily recognized on time slices, they are often laterally shifted from each other. The kind and degree of lateral shift is an indication of the underlying tectonic deformation. Unlike coherence, curvature also images folds and flexures that link fault systems. With proper understanding of the tectonic environment, a skilled interpreter can recognize horsts and grabens, en echelon faults, relay ramps, and pop-up structures on simple time slices. In this tutorial paper, we illustrate some of the lateral relationships between coherence and the various curvature measures using a high-quality, structurally-complex 3D survey acquired within the Chicontepec basin, Mexico.

LIST OF KEYWORDS

3D Seismic, Attributes, Curvature, Chicontepec

Attributes applied to Chicontepec Basin, Mexico

INTRODUCTION

While coherence attributes measure lateral changes in the waveform and allow us to map reflector offsets, lateral changes in stratigraphy, and chaotic depositional features, volumetric curvature attributes measure lateral changes in dip magnitude and dip azimuth, and thus allow us to map folds, flexures, buildups, collapse features, and differential compaction. Both attributes are used widely in detecting faults, with each attribute having its advantages and disadvantages. Coherence accurately tracks vertical faults cutting coherent seismic reflectors. For dipping faults, coherence often exhibits a vertically-smeared stair-step appearance on vertical slices, due to most implementations being computed on vertically-oriented windows parallel to the seismic traces. Where there is fault drag, reflector offset below seismic resolution, or antithetic faulting that appears as fault drag, dip-steered coherence may not illuminate the fault at all. For faults with very small displacement, the reflectors appear to have a subtle change in dip, resulting in the lack of a coherence anomaly; rather, these features appear as a slight flexure resulting in a curvature anomaly.

For faults having significant offset, curvature anomalies often track dip changes on either side of a fault due to drag, antithetic faulting, or syntectonic deposition. For this reason, curvature anomalies are often laterally displaced from the fault trace. The most common way to calibrate attribute anomalies seen on time slices is to visualize their relationship with conventional vertical slices through the seismic amplitude data. Typically, the interpreter animates through a suite of vertical slices to better understand the attribute anomalies. However, given an understanding of the tectonic style, we will show how a skilled interpreter can visualize the 3D fault and fold relationships with only a minimal amount of calibration with the vertical amplitude data.

Murray (1968) provides what we believe to be the first published application of curvature to the detection of subsurface fractures. Later, Lisle (1994) computed curvature from the Goose Egg dome outcrop and correlated it to fracture density. McQuillan (1974) showed air-photo scale of fracture patterns related to basement-controlled lineaments. Roberts (2001) showed the value of curvature computed from interpreted surfaces from 3D seismic surfaces. Stewart and Wynn (2000) and Bergbauer et al. (2003) showed the value of computing curvature at multiple scales, providing long-wavelength and short-wavelength images. Al-Dossary and Marfurt (2006) extended these ideas to volumetric computations.

In this paper we emphasize the interpretational rather than the computational aspects of volumetric curvature and shape indices, showing how it is complementary to the more widely-utilized coherence and other edge detection attributes.

We begin by defining several of the more common curvature attributes, and how they can be computed volumetrically. Given these definitions, we propose using the two principal curvatures, k_1 and k_2, rather than the more commonly used maximum, k_{max}, and minimum, k_{min}, curvatures or most-positive, k_{pos}, and most-negative, k_{neg}, curvatures. Next, we compute and interpret these attributes for a 3D survey acquired over complexly folded and faulted Mesozoic section in the deeper part of the Chicontepec basin, Mexico, to illustrate their lateral relationships. We conclude with a summary of our findings for this type of deformation and discuss potential artifacts and pitfalls in attribute interpretation.

GEOMETRIC DESCRIPTION OF CURVATURE

Curvature at any point, *P*, on a 2D curve is defined by the reciprocal of the radius of the osculating circle, *R*, tangent to the curve at the analysis point (Figure 1). For a 3D

surface, we define curvature at a point *P* by fitting two circles within perpendicular planes tangent to that surface at the analysis point (Figure 2). The reciprocal of the radius of these two circles give rise to what are called apparent curvatures. We rotate the two perpendicular planes until we find the circle with the minimum radius. The reciprocal of this radius is defined as the maximum curvature, k_{max}. For a quadratic surface, the tangent circle contained in the plane perpendicular to that with the minimum radius will contain the circle with the maximum radius, whose reciprocal defines the minimum curvature k_{min}. With the vertical axis being defined as positive down, we will define anticlinal features to have positive maximum curvature, and synclinal features to have negative maximum curvature.

The interpretation of curvature volumes computed over cylindrically-folded geologies (i.e., those defined by a simple 2D cross-section) is straightforward. For the anticline shown in Figure 3, the strongest maximum curvature value will be aligned with the hinge line of the fold, resulting in positive anomalies along the anticlinal fold axis and negative anomalies along the synclinal fold axis.

Along planar portions of the limbs, the curvature values will be approximately zero. Since the layers are continuous, the corresponding seismic waveform for simply folded, constant thickness layered geology would be continuous along the fold, such that dip-steered discontinuity measurements such as coherence will not show any anomalies.

The attribute expression of faults can be considerably more complicated. For normal faults with vertical displacements greater than half a seismic wavelength, we often see a discrete discontinuity that is clearly delineated by a low coherence anomaly. For highly competent rocks we may see no volumetric curvature if the reflector dip on both sides are equal (Figure 4a). However, commonly we see drag on either side of the

fault, which may be either through plastic deformation or through a suite of conjugate faults (Figure 4b). Parallel to the fault strike, we often have ramp structures, generating more complicated 3D curvature anomalies. For an excellent outcrop analysis of such features we direct the reader to a recent publication by Ferrill and Morris (2008).

Listric fault geometries associated with syntectonic deposition can also be complicated. On the footwall, we may see very little deformation, with the sediments maintaining their original attitude at some angle to the fault face. On the hanging wall, the reflectors rotate with depth, often maintaining a near-normal relation to the fault face. We may also see a positive curvature anomaly over a roll-over anticline if one exists (Figure 4c). Coherence does a good job at delineating the fault dislocation. Deeper in the section, as the fault begins to sole out, both coherence and curvature images become noisy and less easily interpreted.

MATHEMATICAL DESCRIPTION OF CURVATURE

Curvature is one of the fundamental components of differential geometry and is used routinely in 3D computer graphics (Salomon 2005), medical (Chen et al. 2007), facial recognition (Bruner and Tagiuri, 1954; Millman and Parker, 1977), and molecular docking (Tripathi, 2006). Mathematicians define curvature as the eigenvalues of a local surface in 3D Gassmannian space (Guggenheimer, 1977).

In this paper we use the same nomenclature as Roberts (2001) who discussed curvature computed from interpreted horizons. All of our computations will be volumetric rather than horizon-based and are built on previously-computed estimates of inline and crossline dip. Currently, there are at least four well-established means of computing volumetric dip based on complex trace analysis (Barnes, 2000), the gradient structure tensor (Randen, 2000), coherence-based scanning methods (Marfurt et al., 1998;

Marfurt, 2006), and prediction error filters (Fomel, 2002). Rather than fitting a quadratic surface to a point on a picked surface with the approximation

$$z(x,y) = ax^2 + by^2 + cxy + dx + ey + f\ , \tag{1}$$

we define the quadratic surface through the inline and crossline derivatives

$$p_x = \frac{\partial z(x,y)}{\partial x} = d\ , \tag{2}$$

and

$$p_y = \frac{\partial z(x,y)}{\partial y} = e\ . \tag{3}$$

Since curvature involves 2nd derivatives of structural elevation (or time for time-migrated data) one needs to compute the derivatives

$$\frac{\partial p_x(x,y)}{\partial x} = 2a\ , \tag{4}$$

$$\frac{\partial p_y(x,y)}{\partial y} = 2b\ , \tag{5}$$

and

$$\frac{\partial p_x(x,y)}{\partial y} = \frac{\partial p_y(x,y)}{\partial x} = c\ . \tag{6}$$

We improve upon Al-Dossary and Marfurt (2006) who computed derivatives on time slices by using full 3D derivatives, shown in Figure 5. This modest improvement significantly improves the appearance of curvature and shape images on vertical sections. Given these five quadratic coefficients Rich (2008) defines the most-positive and most-negative principal curvatures (k_1 and k_2) to be

$$k_1 = \frac{a(1+e^2) + b(1+d^2) - cde + (\alpha - \beta)^{1/2}}{(1+d^2+e^2)^{3/2}}\ , \tag{7}$$

and

$$k_2 = \frac{a(1+e^2)+b(1+d^2)-cde-(\alpha-\beta)^{1/2}}{(1+d^2+e^2)^{3/2}}, \tag{8}$$

where

$$\alpha = [a(1+e^2)-b(1+d^2)]^2, \tag{9}$$

$$\beta = [2bde-c(1+e^2)][2ade-c(1+d^2)], \tag{10}$$

We conclude our mathematical discussion with Roberts (2001) definition of the shape index, *s*

$$s = \frac{2}{\pi}\text{ATAN}\frac{k_1+k_2}{k_1-k_2}, \tag{11}$$

and curvedness, *C*

$$C = \left(k_1^2+k_2^2\right)^{1/2}. \tag{12}$$

The values of *s* = -1.0, -0.5, 0.0, +0.5, and +1.0, indicate bowl, valley, saddle, ridge, and dome quadratic shapes.

MULTIATTRIBUTE VISUALIZATION

Guo et al. (2008) provide a tutorial showing how to use the HLS model to modulate one attribute by another. Kidd (1999) showed how transparency (1.0-opacity) can be used to blend two attributes. In general, we find that blending works best when one of the images is plotted against a polychromatic color bar, while a second is plotted against a gray scale. Later, we illustrate this concept in Figure 6, where we plot the shape index modulated by curvedness against a 2D hue-lightness color map co-rendered with seismic amplitude plotted against a gray scale and set to be 50% transparent (Figure 6c)., and then co-rendered with coherence where high coherence is transparent (Figure 6d).

APPLICATION TO THE CHICONTEPEC BASIN, MEXICO

In order to illustrate the lateral relationship of our definitions of the most positive and most negative principal curvatures and coherence, we use a 3D seismic data acquired over the Amatitlán area of the Chicontepec basin (Figure 7). The Paleocene age Chicontepec formation consists of turbidities and mass transport complexes derived from the Sierra Madre Oriental to the west with perhaps a minor component from the Golden Lane high to the east. The underlying Mesozoic section is structurally deformed, providing accommodation space for the Tertiary sequences, with some faults cutting the exploration objective. The seismic survey is of high quality, with detailed mapping complicated by difficulties in distinguishing zones that are geologically chaotic such as mass-transport complexes and zones that are geophysically chaotic, due to overlying volcanic intrusive and extrusive rocks as well as areas of low seismic fold (Pena et al., 2009).

Figure 8 shows the most-positive curvature anomalies, k_{pos}, in yellow, and the most-positive principal curvature anomalies, k_1 in red. On the right side of the image, k_1 exhibits an anomaly along the axis of a dipping flexure (red arrow) while k_{pos} exhibits an anomaly that is correlated to the axis of a less geologically-interesting part of the fold with respect to the horizontal (yellow arrow). In the gently dipping areas seen on the left side of the image, k_1 and k_{pos} are nearly identical (orange arrow).

Multiple volumetric attributes (most-positive curvature k_{pos}, most-negative curvature, k_{neg}, maximum curvature, k_{max}, minimum-curvature, k_{min}, most-positive principal curvature, k_1, most-negative principal curvature, k_2, azimuth of minimum curvature, ψ_{min}, and energy ratio coherence, c, were calculated from the seismic volume.

The appearance of anticlines and synclines

Figure 9a shows a cartoon of the anticlinal feature corresponding to the green picks line in Figure 9b. Since there are no discrete reflector offsets present along the interpreted horizon, there are no significant coherence anomalies seen in Figure 9c. However, the dip along the interpreted horizon varies laterally. Along the axis of the anticlinal fold, we see anomalies in the most-positive principal curvature (in red). Where the reflectors are synclinal, we see anomalies in the most-negative principal curvature (in blue). Along planar dipping areas of the interpreted horizon, we see no curvature anomaly. In the vertical section, the most-positive principal curvature defines the anticlinal fold axis. The most-negative principal curvature anomalies define the edges of the folded anticline. Figure 9d shows the curvature anomalies as visualized using modern 3D interpretation software. On the time slice, we are able to trace the anticlinal fold axis in NW-SE direction. Figure 9e shows the shape index modulated by curvedness that provides an image of a long (yellow-brown) ridge on the time slice of the large anticline seen on the vertical section. Synclinal features bracketing the anticline appear as (cyan) valleys. Coupled with an appropriate deformation model, Masaferro (2003) showed how maps of the axial folds can be used to predict fractures.

The appearance of reverse faults in a pop-up block

Figure 10 shows several reverse fault features. We note a center pop-up block, with the reflectors bent down along the hanging wall side of the faults. At the top left corner, the fault shows simple displacement with no drag on the reflector; we only see a coherence anomaly (in green). At the right side in Figure 10c, where we note fault drag, the coherence anomaly (in green) are bracketed by a most-positive principal curvature anomaly (in red) on the hanging wall, and a most-negative principal curvature anomaly

(in blue) on the foot wall. At the bottom left of the figure, we only see reflector drag on the hanging wall side, which results in the most-positive principal curvature and coherence anomalies. Figure 10e shows the shape index modulated by curvedness. The faults (grey arrows) are bracketed by long lineaments of (cyan) valleys, and (yellow-brown) ridge. There is a deformation on the structure, creating a (red) dome in the middle of the pop-up block.

The appearance of a graben

Figure 11a and b show normal faults delineating a graben. In Figure 11c, we see a pair of most-positive principal curvature anomalies and coherence next to each other, with a most-negative principal curvature lineament further away. These are the same geometries discussed by Sigusmondi and Soldo (2003). Vertically, curvature anomaly appears to be more continuous, and more easily interpreted than the coherence anomaly which tends to be discontinuous and vertically smeared. Figure 11d shows the curvature anomalies and coherence as visualized in 3D. On the time slice, we are able to trace the faults as they are laterally extended in the NW-SE direction. In Figure 11e, we display the shape index modulated by curvedness co-rendered with the seismic amplitude providing further insight into the shape of the bowl-shaped graben.

The appearance of seismic noise

Like other attributes, curvature is sensitive to data quality. Falconer and Marfurt (2008) show how consistent errors in velocities can cause very subtle, periodic, acquisition footprint anomalies in travel time, which are enhanced by dip component attributes, and further enhanced by curvature attributes. At the Mesozoic level of the Amatitlán survey presented here, the overlying changes in lateral velocity are so great that any footprint periodicity is destroyed. These acquisition and processing artifacts –

most commonly associated with migration aliasing – give rise to curvature artifacts (Figure 12).

The use of image processing to enhance faults and axial planes

Recent advances in image enhancement have made significant progress in accelerating the interpretation process. One of the primary focuses is to skeletonize and join up discontinuities measured by coherence to approximate a more-continuous fault plane generated by a human interpreter. One approach is to use a suite of successive non-linear median-family filters (e.g. Barnes, 2006). We use a commercial implementation of an 'ant-tracking' algorithm described by Pedersen et al. (2002) to improve the continuity and sharpness of faults measured by coherence (Figures 13b, c, 14a, and b). We can also apply the same algorithm to improve the continuity and sharpness of axial planes as measured by curvature (Figures 13b and 14a).

Calibration on horizons

Our final calibration exercise is to examine curvature and coherence attributes extracted on a picked horizon. Figure 13a shows a conventional time-structure map at the top of Cretaceous enhanced with shaded relief illumination. Figure 13b shows a horizon slice through the coherence volume co-rendered with the most-positive and most-negative principal curvatures. Figure 13c shows a horizon slice through the coherence volume co-rendered with the shape index modulated by curvedness. Armed with our previous analysis of the attribute expression of structural styles (normal faults, grabens, axial planes, pop-up blocks) as well as of migration artifacts, we can confidently interpret the features seen on this multi-attribute horizon slice.

Figures 14a and b show time slices at t=1.5s at the approximate top-Cretaceous level through the same co-rendered attribute volumes. Note that the patterns are markedly

similar and that we can easily identify grabens, and pop-up features on the uninterpreted attribute volumes. Pop-up blocks appear as yellow (ridge) anomalies bound by two low coherence faults. Down-dropped blocks with drag on the faults appear as low coherence zones bracketed by a ridge on the hanging wall and a valley on the foot wall. By animating through these co-rendered time and vertical slices, we quickly define the structural complexity even in areas that may not contain mappable horizons.

CONCLUSIONS

Discontinuity measurements such as coherence are not sensitive to folding continuities, and often result in anomalies that are broken when viewed in the vertical section. Where they are not vertically smeared, they accurately locate the discontinuity. In contrast, curvature lineaments are more continuous on the vertical section and map folds and flexures. With fault drag and/or antithetic faulting, volumetric curvature will commonly bracket faults but may not coincide with the exact fault location. Co-rendering curvature with coherence along with the seismic amplitude data provides a superior interpretation product, allowing us to quickly visualize and quantify the structural style on uninterpreted vertical and time slices.

ACKNOWLEDGMENTS

We thank PEMEX Exploración y Producción for permission to publish this work and particularly to Juan M. Berlanga, Proyecto Aceite Terciario del Golfo, PEMEX Exploración y Producción, for making our work possible through access to seismic data, support for the data reprocessing and bits of help along the way. Thanks to the sponsors of the OU Attribute-Assisted Seismic Processing and Interpretation (AASPI) consortium. Thanks to Schlumberger for providing OU with licenses to Petrel used in the interpretation, ant-tracking, and 3D multi-attribute co-rendering. Thanks to Prof. S.

Varahan for helping with the overview on the use of curvature and shape indices in 3D differential geometry.

REFERENCES

Barnes, A. E., 2000, Weighted average seismic attributes: Geophysics, **65**, 275–285.

Barnes, A. E., 2006, A filter to improve seismic discontinuity data for fault interpretation, Geophysics, **71**, P1-P4

Blumentritt, C., K. J. Marfurt, and E. C. Sullivan, 2006, Volume-based curvature computations illuminate fracture orientations, Lower-Mid Paleozoic, Central Basin Platform, West Texas: Geophysics, **71**, B159-B166.

Bruner, I. S. and Tagiuri, R. 1954. The perception of people. In Handbook of Social Psychology, Vol. **2**, G. Lindzey, Ed., Addison-Wesley, Reading, MA, 634-654

Chen D., A. A. Farag, M. S. Hassouna, R. Falk, Principal Curvature Based Colonic Polyp Detection: Proc. of Computer Assisted Radiology and Surgery (CARS'07), Berlin, Germany, June 27-30, 2007, pp. 6-8.

Falconer, S., and K. J. Marfurt, 2008, Attribute-driven footprint suppression, 78th Annual International Meeting of the SEG, Expanded Abstracts, 2667-2671.

Ferrill, D. A., and A. P. Morris, 2008, Fault zone deformation controlled by carbonate mechanical stratigraphy, Balcones fault system, Texas: AAPG Bulletin, **92**, 359-380.

Fomel , S., 2002, Applications of plane-wave destruction filters, Geophysics, **67**, 1946-1960

Gou, H., S. Lewis, and K. J. Marfurt, 2008, Mapping Multiple Attributes to 3- and 4-Component Color Models – a Tutorial: Geophysics, **73**, W7-W19.

Guggenheimer, H. 1977, Surfaces, Differential Geometry, Dover, ISBN 0-486-63433-7.

Gordon, G. 1991. Face recognition based on depth maps and surface curvature. In SPIE Proceedings, Vol. **1570**: Geometric Methods in Computer Vision. SPIE Press, Bellingham, WA 234—247.

Kidd, G. D., 1999, Fundamentals of 3-D seismic volume visualization: The Leading Edge, **18**, 702-712.

Lisle, R. J., 1994, Detection of zones of abnormal strains in structures using Gaussian curvature analysis: AAPG Bulletin, **78**, 1811-1819.

Masaferro, J. L., M. Bulnes, J. Poblet, and N. Casson, 2003, Kinematic evolution and fracture prediction of the Valle Morado structure inferred from 3-D seismic data, Salta province, northwest Argentina: AAPG Bulletin, **87**, 1083-1104.

McQuillan, H., 1974, Fracture patterns on Kuh-eAsmari anticline, southwest Iran:AAPGBulletin, **58**, 236–246.

Millman, R. S. and G. D. Parker, 1977, Elements of Differential Geometry, Prentice-Hall, ISBN 0-132-64143-7.

Murray, Jr., G. H., 1968, Quantitative fracture study-Spanish Pool, McKenzie County, North Dakota: AAPGBulletin, **52**, 57–65.

Nissen, S. E., T. R. Carr, K. J. Marfurt, and E. C. Sullivan, 2009, Using 3-D seismic volumetric curvature attributes to identify fracture trends in a depleted Mississippian carbonate reservoir: Implications for assessing candidates for CO2 sequestration, in M. Grobe, J. C. Pashin, and R. L. Dodge, eds., Carbon dioxide sequestration in geological media—State of the science: AAPG Studies in Geology **59**, p. 297–319.

Pedersen, S. I., T. Randen, L. Sonneland, and O. Steen, 2002, Automatic 3D Fault interpretation by artificial ants: 64th Meeting, EAGE Expanded Abstracts, G037.

Pena, V., S. Chávez-Pérez, M. Vázquez-García, and K. J. Marfurt, 2009, Impact of shallow volcanics on seismic data quality in Chicontepec Basin, Mexico: The Leading Edge, **28**, 674-679.

Rich, J., 2008, Expanding the applicability of curvature attributes through clarification of ambiguities in derivation and terminology: 78th Annual International Meeting, SEG, Expanded Abstract, 884-888.

Roberts, A., 2001, Curvature attributes and their application to 3D interpreted horizons: First Break, **19**, 85-99.

Randen, T., Monsen, E., Signer, C., Abrahamsen, A., Hansen, J.O., Saeter, T., Schlaf, J., 2000, Three dimensional texture attributes for seismic data analysis: 70th Annual International Meeting, SEG, Expanded Abstract, 668-671.

Salvador, A., 1991, Origin and development of the Gulf of Mexico basin, *in* Salvador, A., ed., The Gulf of Mexico Basin, The Geology of North America: **J**, Decade of North American Geology, Geological Society of America, 389-444.

Salomon, D., 2005, Curves and Surgaces for Computer Graphics, Springer Verlag, ISBN 0-387-24196-5.

Sigismondi, E. M., and J. C. Soldo, 2003, Curvature attributes and seismic interpretation: Case studies from Argentina basins: The Leading Edge, **22**, 1122-1126.

Stewart, S. A., and T. J.Wynn, 2000, Mapping spatial variation in rock properties in relationship to scale-dependent structure using spectral curvature. Geology: **28**, 691–694.

Sullivan, E. C., K. J. Marfurt, A. Lacazette, and M. Ammerman, 2006, Application of new seismic attributes to collapse chimneys in the Fort Worth Basin: Geophysics, **71**, B111-B119.

Tripathi V. K., B. Dasgupta, K. Deb, 2006. A Computational Method for Viewing Molecular Interactions in Docking. VIEW 2006, 152-16.

LIST OF FIGURES

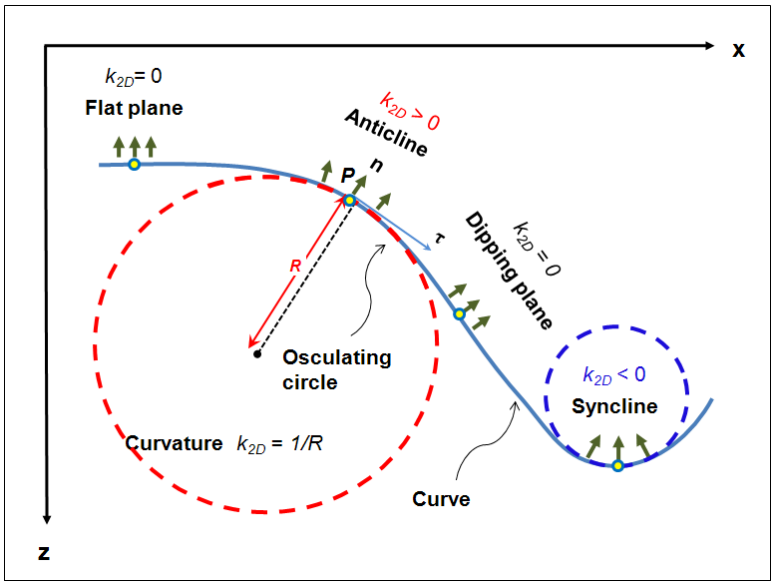


Figure 1. Definition of curvature. For a particular point **P** on a curve. Green arrows indicate normal vectors, **n**, to the curve. ***τ*** is the vector tangent to the curve at point P. Curvature is defined in terms of the radius of the circle tangent to the curve at the analysis point. Anticlinal features have positive curvature (k_{2D}>0), and synclinal features have negative curvature (k_{2D} <0). Planar features (dipping or horizontal) have zero curvature (k_{2D} =0). (Modified after Roberts, 2001).

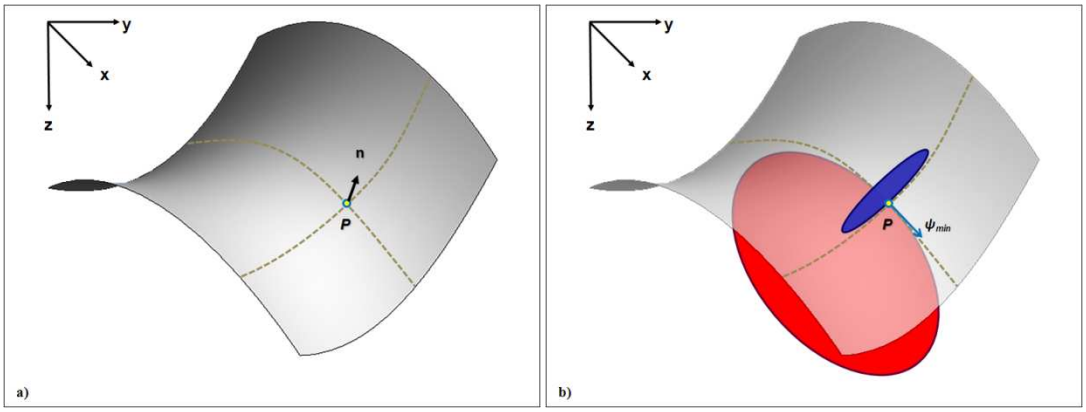


Figure 2. (a) A quadratic surface with the normal, **n**, defined at point *P*. (b) The circle tangent to the surface whose radius is minimum defines the magnitude of the maximum curvature, $|k_{max}| \equiv 1/R_{min}$ (in blue). For a quadratic surface, the plane perpendicular to that containing the previously defined blue circle will contain one whose radius is maximum, which defines the magnitude of the minimum curvature, $|k_{min}| \equiv 1/R_{max}$ (in red). Graphically, the sign of the curvature will be negative if it defines a concave surface and positive if it defines a convex surface. For seismic interpretation, we typically define anticlinal surfaces as being convex up, such that k_{max} has a negative sign and k_{min} has a positive sign in this image.

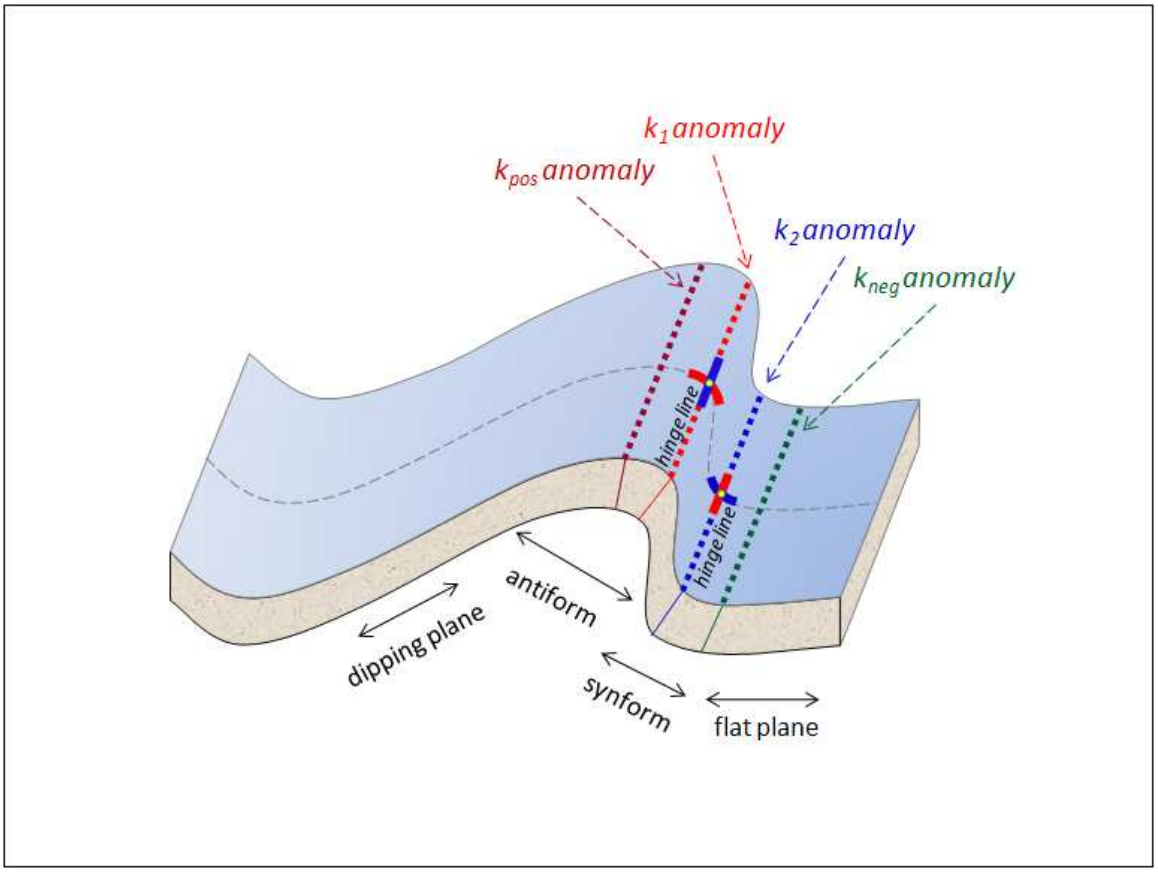


Figure 3. Lateral displacement of most-positive (k_{pos}) and most-negative curvature (k_{neg}) anomalies, correlating the crest and trough of the folded structure from what we denote as the most-positive and most-negative principal curvature anomalies (k_1 and k_2) which correlate to the more geologically relevant anticlinal and synclinal fold axes. For this image with approximately 2D symmetry in the vertical plane, the anomalies for k_{max} would be identical in location and sign for those of k_1 and k_2, such that the major anomalies could be efficiently mapped using a single (rather than two) attributes.

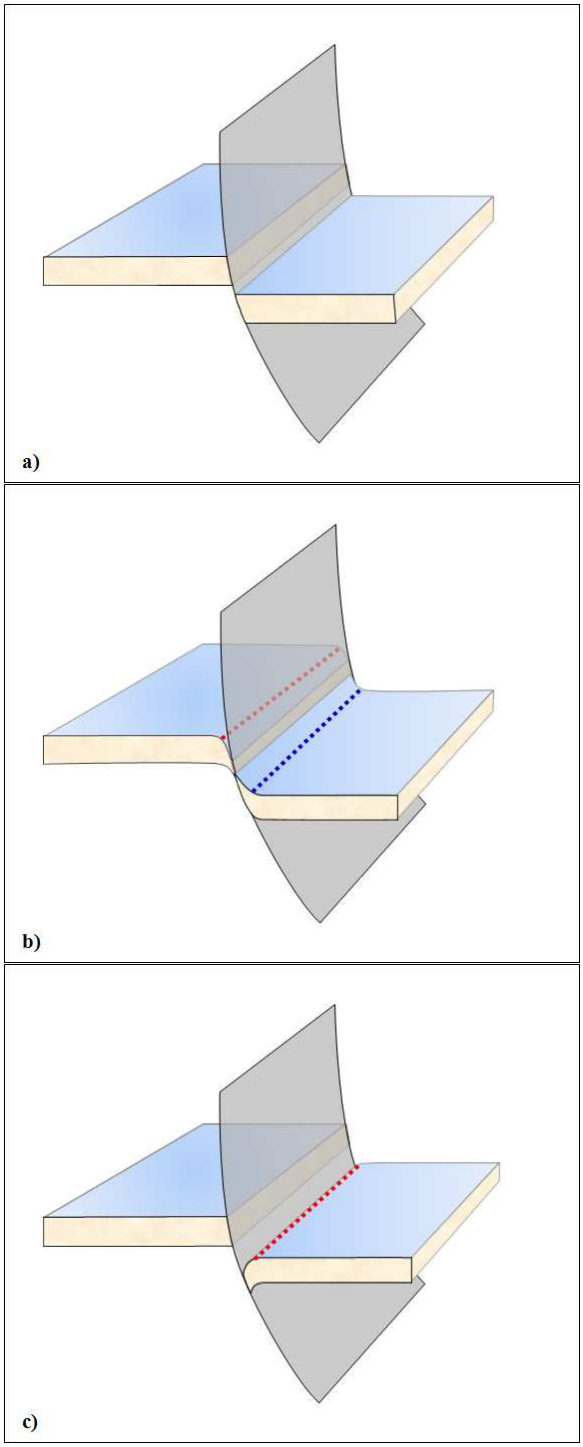


Figure 4. Normal faults expressing different mechanisms: (a) a fault showing simple displacement with no drag, that would result in a coherence anomaly, but exhibiting no change in dip and hence no volumetric curvature anomalies, (b) a fault with drag on both sides exhibiting no coherence anomalies, but a most-positive principal curvature anomaly on the footwall (in red) and a most-negative principal curvature anomaly on the hanging wall (in blue), and (c) a growth fault with syntectonic deposition, which would exhibit both a coherence anomaly and a most-positive principal curvature anomaly over the roll-over anticline (in red).

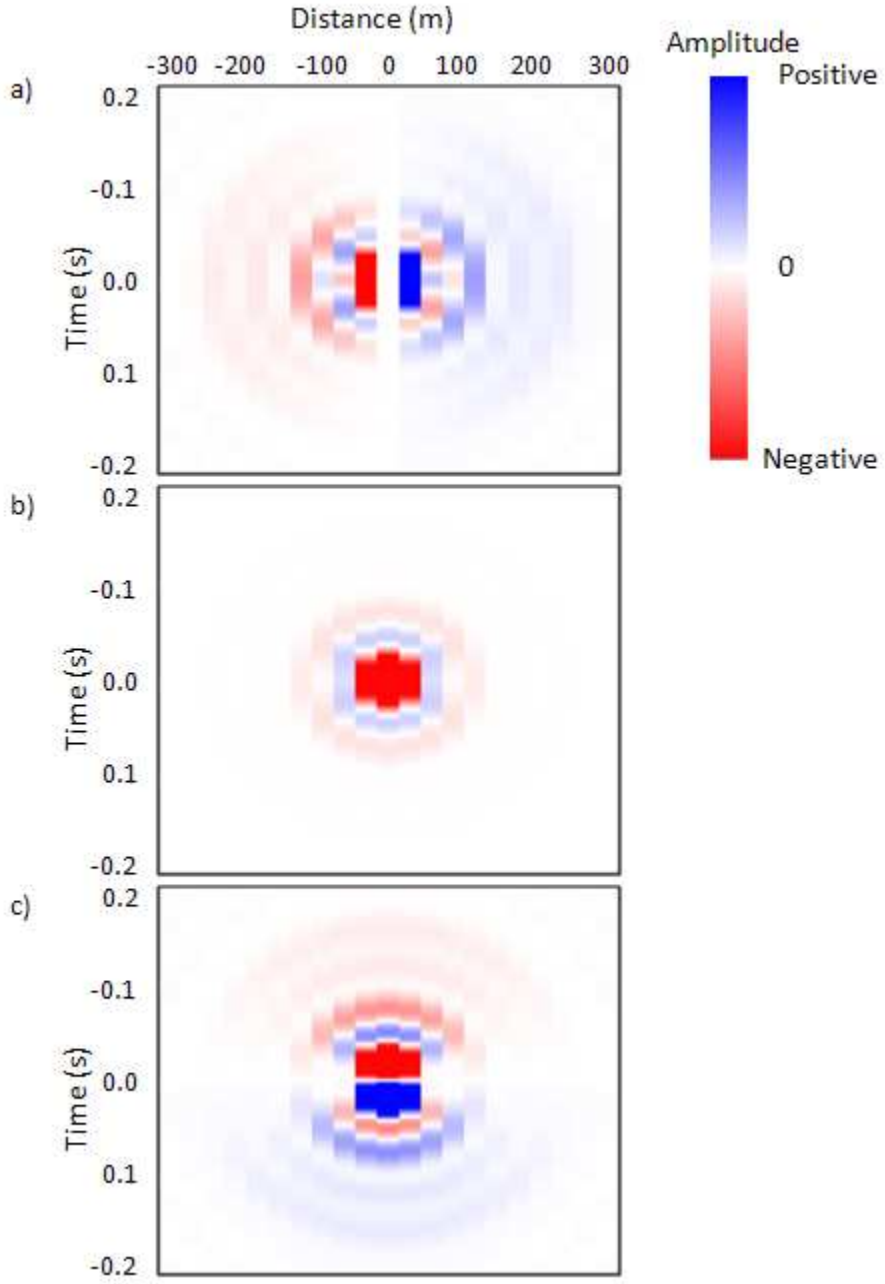


Figure 5. A vertical slice along y=-30 m, of the 3D derivative operator *s* (a) $\partial/\partial x$, (b) $\partial/\partial y$, and (c) $\partial/\partial t$ applied to the inline and crossline components of dip used in volumetric curvature computation for data sampled at Δx=30 m, Δy=30 m, and Δt=2 ms. The operator $\partial/\partial t$ is computed from $\partial/\partial z$ using a constant reference velocity. The value of $\partial/\partial y$ along $y=0$ is identically zero.

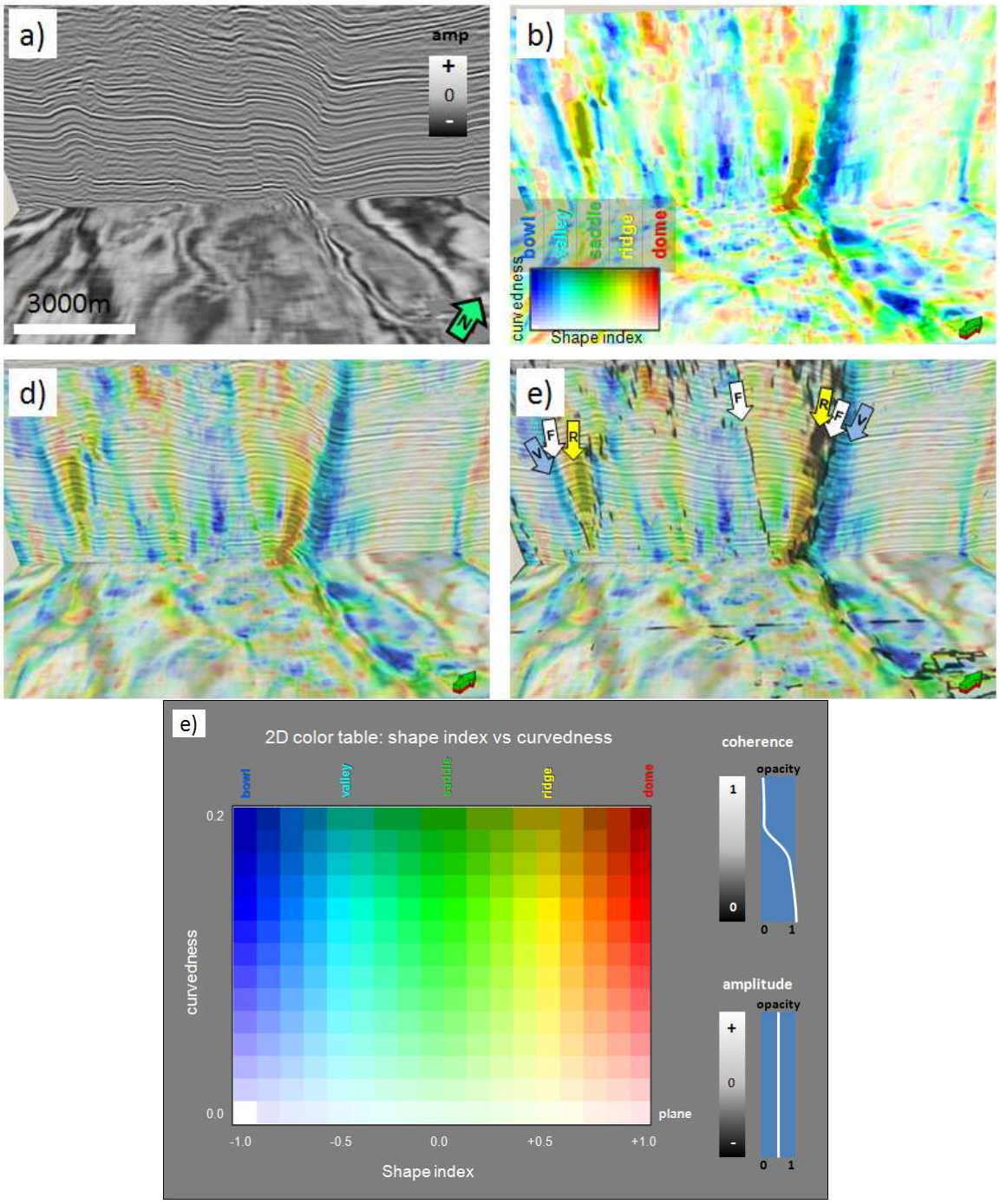


Figure 6. (a) Representative seismic amplitude vertical and time slice. On the same slices, I co-render (b) shape index modulated by curvedness with (c) seismic amplitude and (d) coherence and seismic. The seismic amplitude is set to be 50% transparent. White arrows indicate faults, blue arrows indicate valleys, and yellow arrows indicate ridge features. (e) 2D color table used in shape index modulated by curvedness, and color legend for coherence and seismic amplitude.

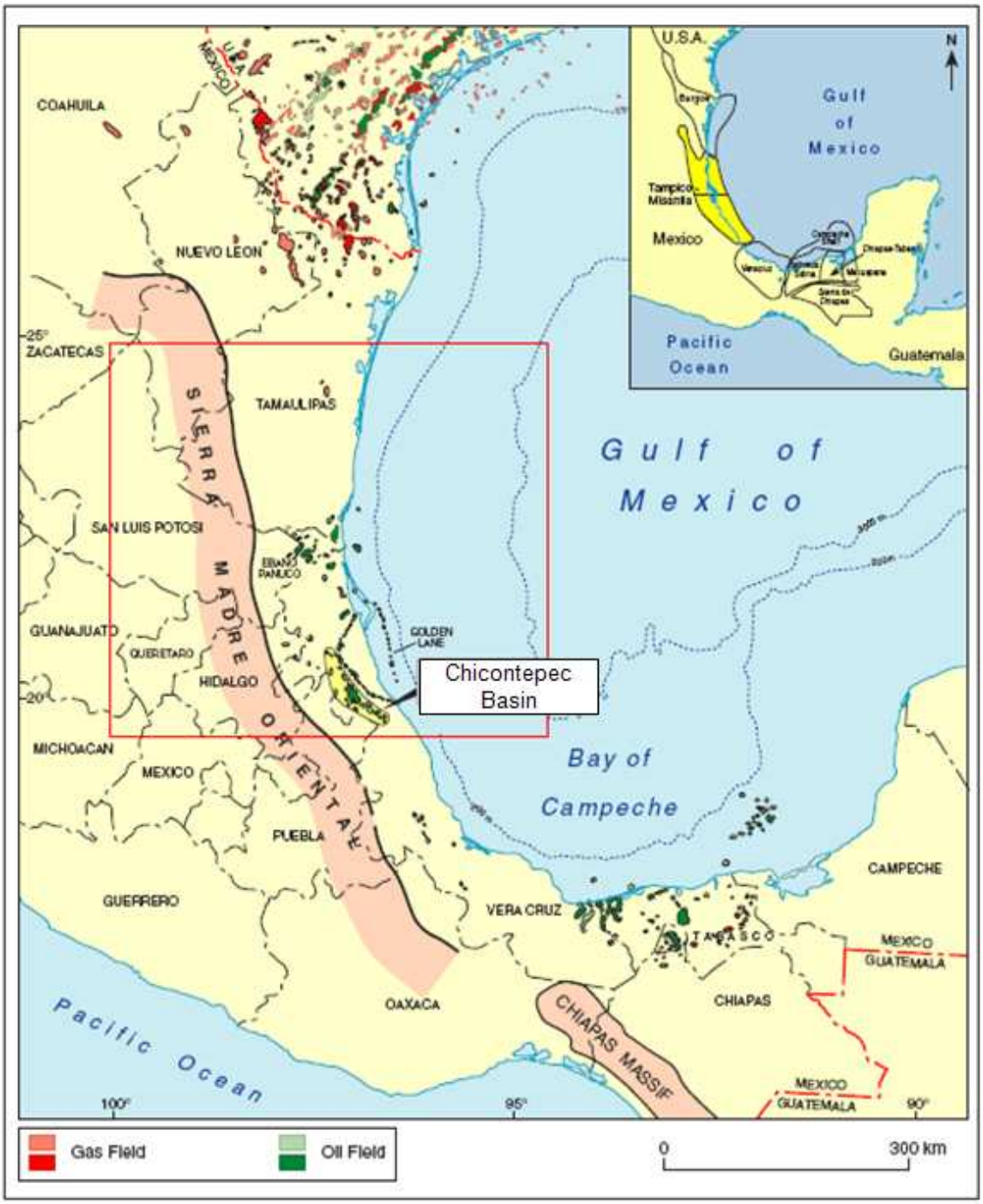


Figure 7. Location of Chicontepec basin, Mexico. (After Salvador, 1991).

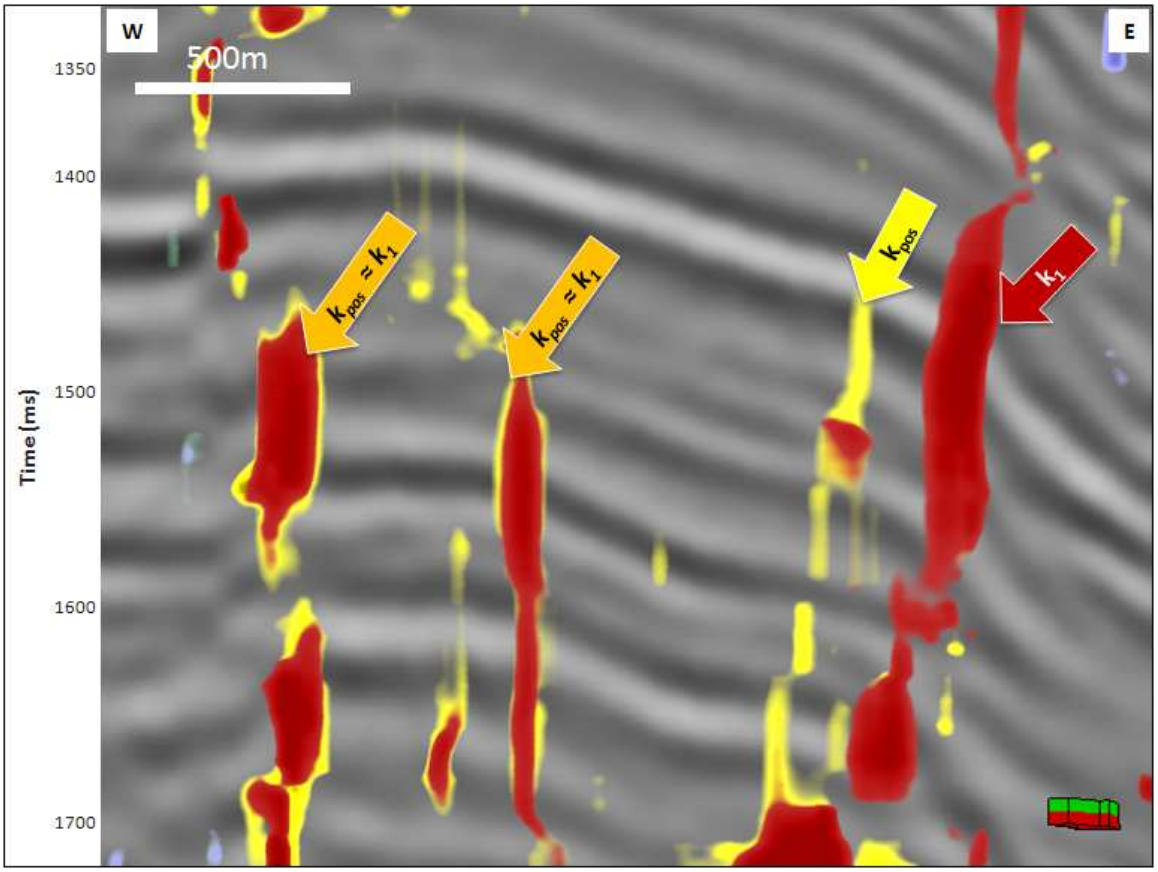


Figure 8. Most-positive curvature anomalies (yellow) co-rendered with most-positive principal curvature anomalies (red). Note how the anomalies are aligned in the western, flatter part of the image.

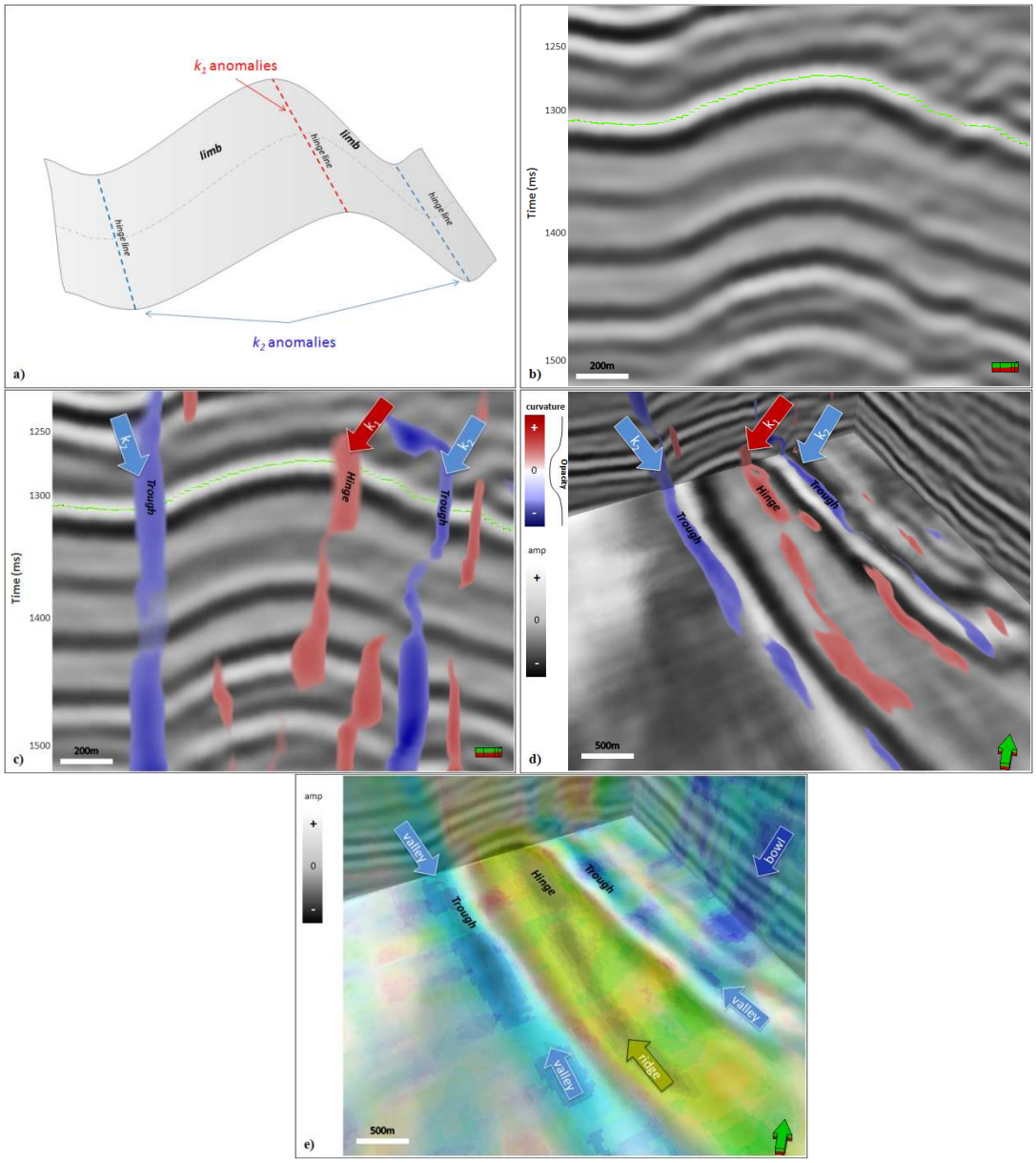


Figure 9. (a) A cartoon of a fold. Anticlinal feature with most-positive principal curvature anomalies, k_1, in red, delineating the anticline's hinge line, and most-negative principal curvature anomalies, k_2, in blue, corresponding to the synclinal axes of the fold. There are no significant coherence anomalies. (b) Representative vertical slice through the seismic amplitude volume showing a fold. (c) Seismic amplitude co-rendered with most-positive and most-negative principal curvatures. (d) 3D view of a vertical and time slice through the amplitude data co-rendered with most-positive and most-negative principal curvature. (e) The shape index modulated by curvedness, co-rendered with seismic amplitude. 2D color legend same as Figure 6e.

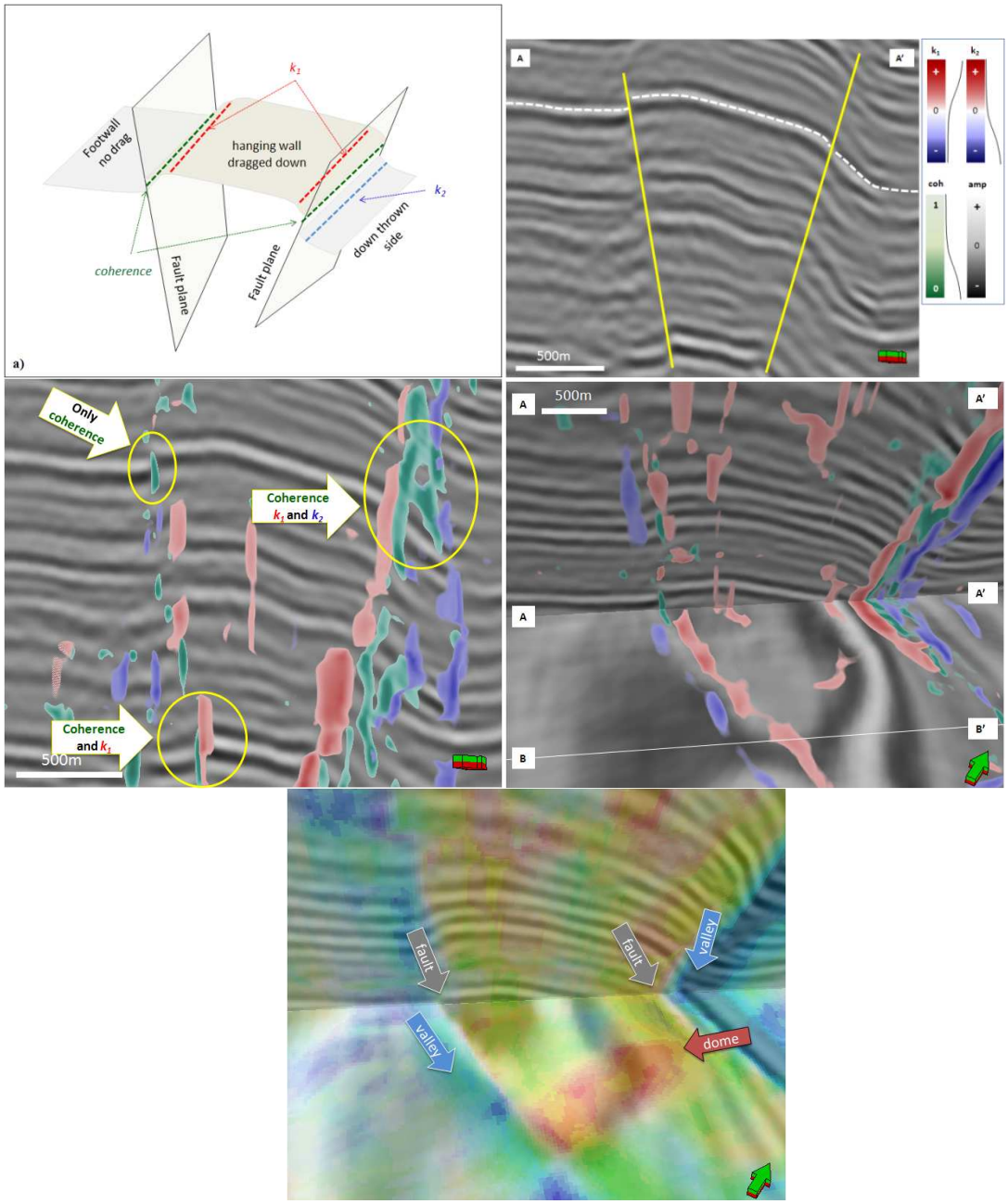


Figure 10. (a) Cartoon of a pop-up structure showing two faults giving rise to coherence (green) anomalies separating most-positive principal curvature (red), and most-negative principal curvature (blue) anomalies. (b) Vertical section through the seismic amplitude data showing a pop-up block. (c) Seismic amplitude co-rendered with most-positive and most-negative principal curvatures and coherence. (d) 3D view of a vertical and time slice through the amplitude data co-rendered with most-positive and most-negative principal curvature and coherence. (e) The shape index modulated by curvedness, co-rendered with coherence and seismic amplitude. 2D color legend same as Figure 6e.

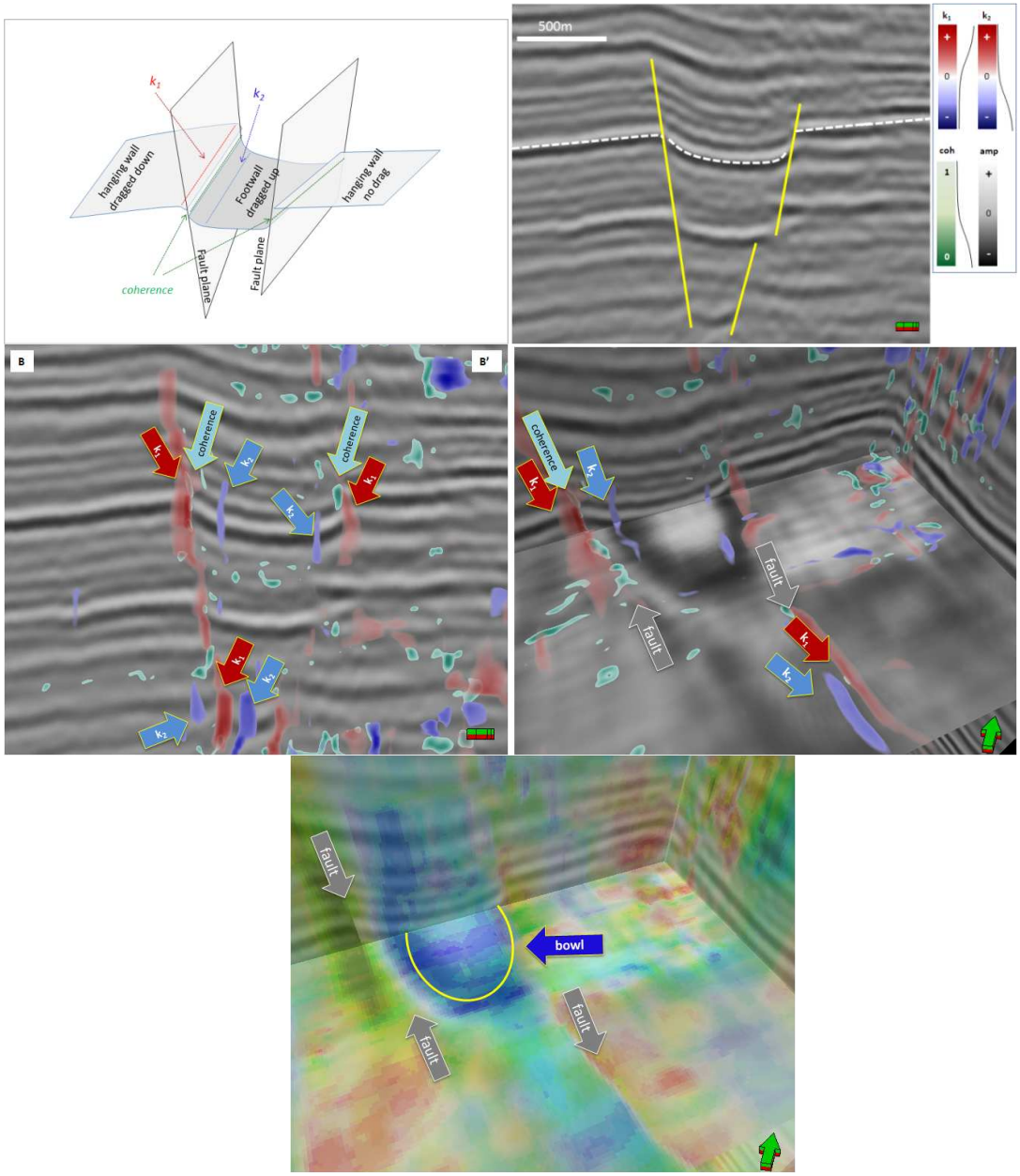


Figure 11. (a) Cartoon of a graben structure showing two faults giving rise to coherence (green) anomalies separating most-positive principal curvature (red), and most-negative principal curvature (blue) anomalies. (b) Vertical section through the seismic amplitude data showing graben. (c) Seismic amplitude co-rendered with most-positive and most-negative principal curvatures and coherence. (d) 3D view of a vertical and time slice through the amplitude data co-rendered with most-positive and most-negative principal curvature and coherence. (e) The shape index modulated by curvedness, co-rendered with coherence and seismic amplitude. 2D color legend same as Figure 6e.

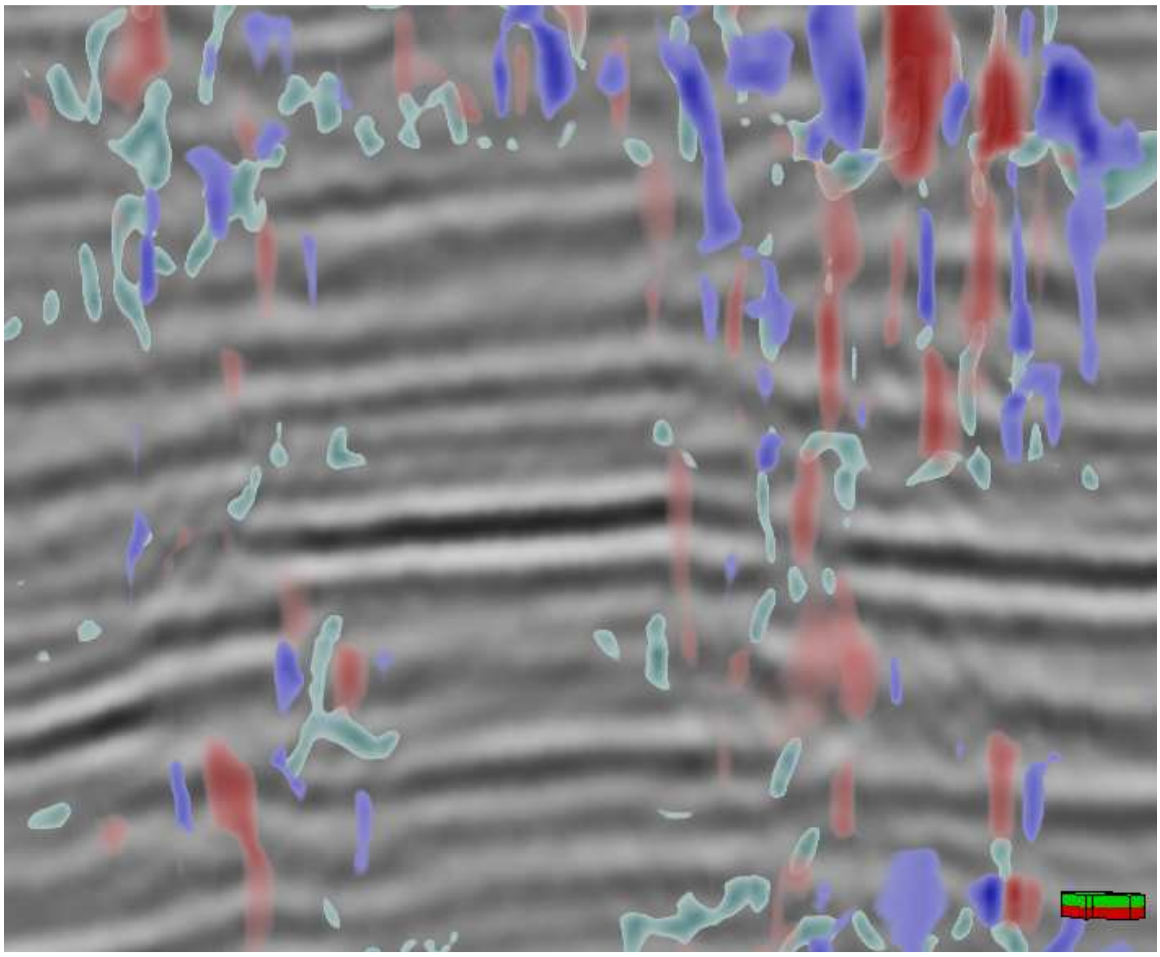


Figure 12. Seismic artifacts due to shallow volcanic and low fold giving rise to curvature and coherence anomalies.

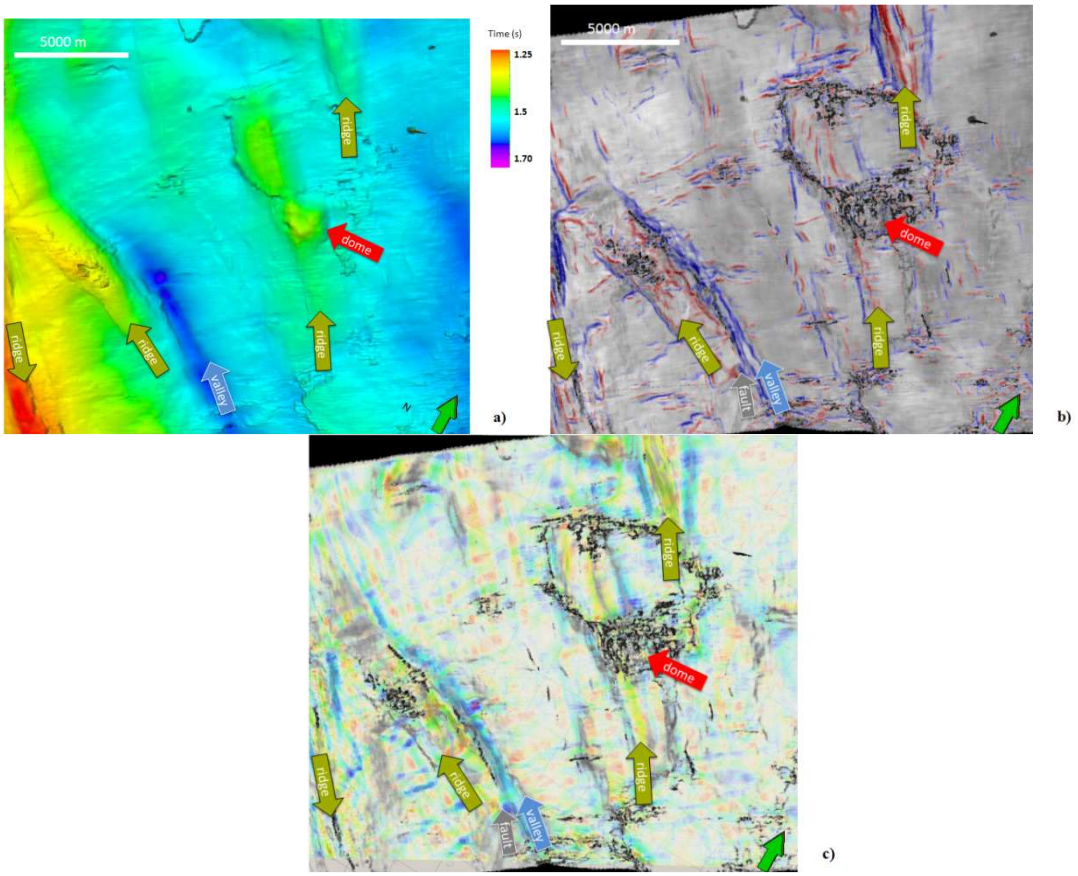


Figure 13. (a) Time-structure map of the top-Cretaceous horizon. (b) Horizon slice through coherence along the top-Cretaceous co-rendered with corresponding most-positive and most-negative principal curvature slices. (c) Horizon slice through coherence along the top-Cretaceous co-rendered with the shape-index modulated by curvedness slice. 2D color legend same as Figure 6e.

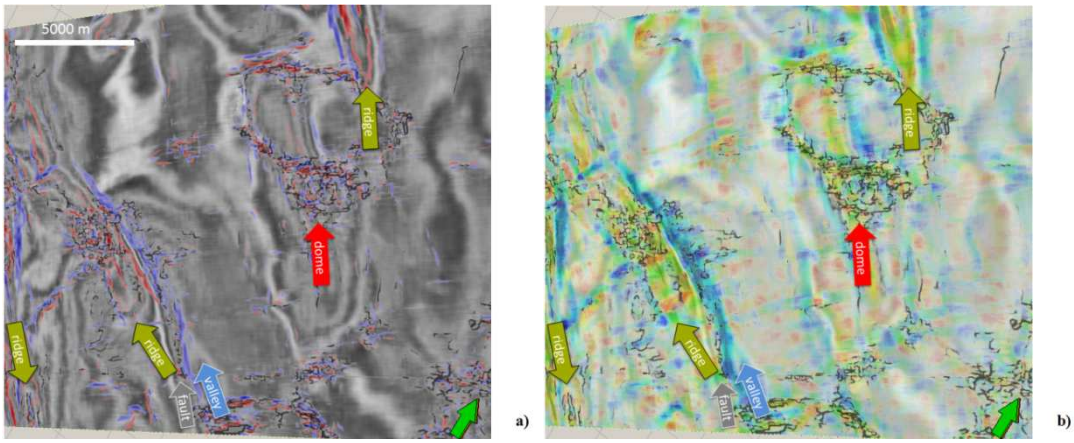


Figure 14. (a) Time slice at 1.5s at the approximate top Cretaceous level though seismic amplitude, co-rendered with corresponding most-positive and most-negative principal curvature slices. (b) Time slice at 1.5s at the approximate top Cretaceous level though coherence along the top-Cretaceous co-rendered with the shape-index modulated by curvedness slice. 2D color legend same as Figure 6e.

Chapter 6 Use of seismic attributes in structural interpretation

Summary

In this chapter, I include a suite of published abstracts that illustrate effective work flows using volumetric estimates of curvature, structure lineaments, rose diagrams and other tools to data volumes from Canada, Mexico, USA, and Vietnam:

- Mai, H. T., and K. J. Marfurt, 2008, Attribute Illumination of Basement Faults, Cuu Long Basin, Vietnam: 78th Annual International Meeting, SEG, Expanded Abstract, **27**, 909-913.
- Mai, H. T., O. O. Elebiju, K. J. Marfurt, 2008, Attribute illumination of basement faults, examples from Cuu Long Basin basement, Vietnam and the Midcontinent, USA: 2nd International Fractured Basement Reservoir Conference, Petro Vietnam, Proceedings, 181-190.
- Mai, H. T., C.F. Russian, K. J. Marfurt, R. A. Young, A. W. Small, 2009, Curvatures lineament and multi-attribute display of full-stack PP, SS, and Acoustic Impedance seismic data – Diamond-M field, West Texas: 79th Annual International Meeting, SEG, Expanded Abstract, **28**, 1112-1116.
- Mai, H. T., K. J. Marfurt, S. Chávez-Pérez, 2009, Coherence and volumetric curvatures and their spatial relationship to faults and folds, an example from Chicontepec basin, Mexico: 79th Annual International Meeting, SEG, Expanded Abstract, **28**, 1063-1067.
- Chopra S., K. J. Marfurt, H. T. Mai, 2009, Using 3D Rose diagrams for correlation of seismic fracture lineaments with similar lineaments from attributes and well log data: 79th Annual International Meeting, SEG, Expanded Abstract, **28**, 3574-3578.

- Mai, H. T., K. J. Marfurt, M. T. Tan, 2009, Multi-attributes display and rose diagrams for interpretation of seismic fracture lineaments, example from Cuu Long basin, Vietnam: 9th SEGJ International Symposium, SEGJ, Paper 0093.
- Chopra S., K. J. Marfurt, H. T. Mai, 2009, Using automatically generated 3D rose diagrams for correlation of seismic fracture lineaments with similar lineaments from attributes and well log data: First Break, **27**, 37-42.

Attribute Illumination of basement faults, Cuu Long Basin, Vietnam

Ha T. Mai and Kurt J. Marfurt, University of Oklahoma, Norman, USA*

Summary

Geometric attributes such as coherence and curvature have been very successful in delineating faults in sedimentary basins. While not a common exploration objective, fractured and faulted basement forms important reservoirs in Mexico, India, Yemen, and Vietnam. Because of the absence of stratified, coherent reflectors, illumination of basement faults is more problematic than illumination of faults within the sedimentary column. In order to address these limitations we make simple modifications to well-established vector attributes including structural dip and azimuth, amplitude gradients, and maximum and minimum curvature, to provide greater interpreter interaction. We apply these modifications to better characterize faults in the granite basement of the Cuu Long Basin, Vietnam, that form an unconventional, but very important oil reservoir.

Introduction

Faults play an important role in forming effective fracture porosity for hydrocarbon traps in the granite basement of the Cuu Long Basin, Vietnam. Mapping fault/fracture intensity and orientation can help delineate sweet spots and better aid horizontal drilling. In the Cuu Long Basin, faults and fractures tend to be planar and steeply dipping, such that we expect to see them more distinctly by viewing them perpendicular to their strike. Interactive shaded-relief maps of picked horizons are provided in nearly all 3D seismic interpretation software packages. Although most easily understood as sun-shading with locally higher relief features creating shadows that enhance the appearance of subtle dips, mathematically, shaded-relief maps comprise simple axis rotations and projection of the two orthogonal dip components of the surface with the direction of illumination

Barnes (2003) showed how volumetric estimates of structural dip and azimuth can be used to generate shaded-relief volumes. We imitate this work and generate directional structural dip, amplitude gradient, and curvature volumes and evaluate the results in terms of basement fault illumination in the Cuu Long basin.

Method

A planar surface such as dipping horizon or faults can be presented by its true dip azimuth θ and strike ψ. The true dip θ can be presented by apparent dips θ_x and θ_y along the *x* and *y* axes (Figure 1).

For time-migrated seismic data, it's more convenient to measure apparent seismic time dips (px, py) components along inline and crossline directions in s/ft or s/m. For depth-migrated seismic data such as our Cuu Long survey, we simply compute θ_x and θ_y and display them either as components or as dip magnitude, θ, and dip azimuth, ψ, or alternatively as dimensionless (px, py) measured in ft/ft or m/m.

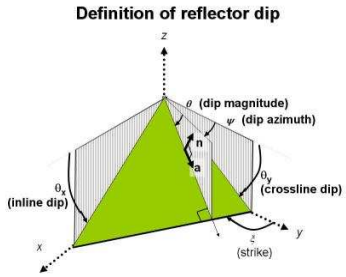


Figure 1: Mathematical, geologic, and seismic nomenclature used in defining reflector dip. By convention, **n** = unit vector normal to the reflector; **a** = unit vector dip along the reflector; θ = dip magnitude; ψ = dip azimuth; ξ = strike; θx = the apparent dip in the xz plane; and θy = the apparent dip in the yz plane. (after Chopra and Marfurt 2007)

There are several popular means of computing volumetric dip components, including those based on weighted versions of the instantaneous frequency and wave-numbers (Barnes, 2002), on the gradient structure tensor (Randen et al., 2000) and on discrete semblance-based dip searches (Marfurt, 2006). The relationship between apparent seismic time/depth dips and apparent angle dips are:

$$p_x = 2 * \tan(\phi_x) / v\,, \qquad (1a)$$

$$p_y = 2 * \tan(\phi_y) / v\,, \qquad (1b)$$

where v is an average time to depth conversion velocity.

We can compute apparent dip at any angle ψ from North through a simple trigonometric rotation:

$$p_\psi = p_x \cos(\psi - \varphi) + p_y \sin(\psi - \varphi)\,, \qquad (2)$$

where ϕ is the angle of the inline seismic axis from North.

Marfurt (2006) also describes an amplitude gradient vector attribute that has inline and crossline components (g_x, g_y). We can therefore compute an amplitude gradient at any angle, ψ, from North:

$$g_\psi = g_x \cos(\psi - \phi) + g_y \sin(\psi - \phi)\,. \qquad (3)$$

To compute the apparent curvature at an angle, δ, from the azimuth of minimum curvature, χ, we slightly modify Roberts' (2001) description of Euler's formula:

$$k_\delta = k_{\max} \sin^2 \delta + k_{\min} \cos^2 \delta\,, \qquad (4)$$

where k_{min} and k_{max} are the minimum and maximum curvatures. To compute the apparent curvature at an angle ψ, from North we write:

$$k_{\psi} = k_{\max} \sin^2(\psi - \chi) + k_{\min} \cos^2(\psi - \chi) . \quad (5)$$

Using equations 2, 3, and 5, we are able to animate through a suite of apparent dip, amplitude gradient, and curvature images at increments of 15^0 to see which perspective best illuminates structural features of interest.

Application

We compute apparent dip, energy-weighted amplitude-gradient methods, and curvature for our 3D post-stack depth-migrated seismic dataset from the Cuu Long basin, Vietnam.

The structure of Pre-Cenozoic basement of the Cuu Long Basin is very complex, and is mainly composed of magmatic rocks. Under the influence of tectonic activity, the basement was broken into a suite of fault systems. This faulting provided favorable conditions for hydrocarbons from a laterally deeper Oligocene-Miocene formation to migrate and accumulate in the basement high.

Since the nature of this basement is magmatic rocks, the seismic signal is very weak and noisy. Applying different methods to enhance the faults signatures will aid our seismic interpretation, with the ultimate goal of estimate fracture location, density, and orientation.

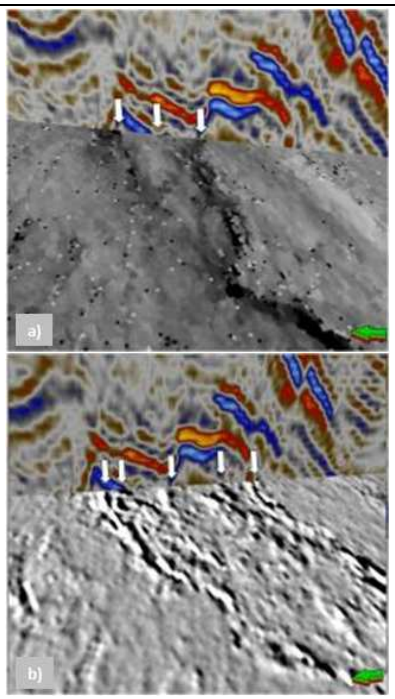


Figure 2: Seismic section on (a) apparent dip depth slice and (b) amplitude gradient. The white arrows show location where the attributes help interpreting fault features

The top of basement was highly compressed, forming a high angle push-up to about 2500 m (Figure 3). The top of this basement high dips to the east and west at about 60^o. Faults were formed along all four sides and cut deep into the basement (Figure 2).

In Figure 3 we display depth slices at 2750 m through the apparent dip volume, p_{ψ}, as a function of azimuth. We used equation 2 to compute images at ψ = 0^O, 30^O, 60^O, 90^O, 120^O, and 150^O.. White arrows indicate the major NE-SW trending main faults, while yellow arrows indicate more subtle faults cutting across them.

In Figure 4 we display depth slices at 2750 m through apparent the amplitude gradient volume, g_{ψ}, as a function of azimuth. We used equation 3 to compute images at ψ = 0^O, 30^O, 60^O, 90^O, 120^O, and 150^O. White arrows indicate lineaments that we interpret to be indicative of subtle faults and fractures. Close to the north azimuth, we see a suite of NE-SW dipping features, which include faults and top basement boundary. The basement edge is dipping rapidly at an angle of about 70^O or more at this location. There are many faults running along this edge that propagate into the shallower sedimentary column.

In Figures 4d and 4e, nearly perpendicular to inline direction, we recognize many NW-SE trending features, which are believed to be faults cutting across the basement. These features did not appear in the apparent gradient images parallel to the features.

Apparent curvature is computed from the maximum, minimum curvatures and the azimuth of minimum curvature shown in Figure 5.

Conclusions

Several modern attributes, including volumetric computation of structural dip and azimuth, structural curvature, amplitude gradients, and amplitude curvature, are multi-component in nature and are thus amenable to visualization from different user-controlled perspectives. Precomputing every desired azimuthal view results in consumption of significant disk storage. However, through the use of 'fast-batch' spreadsheet-like attribute calculators available in several 3D interpretation software packages, such manipulation can now be put under user control. Eventually, we envision generating truly interactive azimuthal visualization software, thereby enabling the interpret to extract as much information from the data as possible.

Acknowledgments

We thank PetroVietnam and Cuu Long JOC for permission to publish the seismic data used in this paper. The rotation of the images was achieved through the use of Schlumberger's Petrel 'Attribute Calculator'.

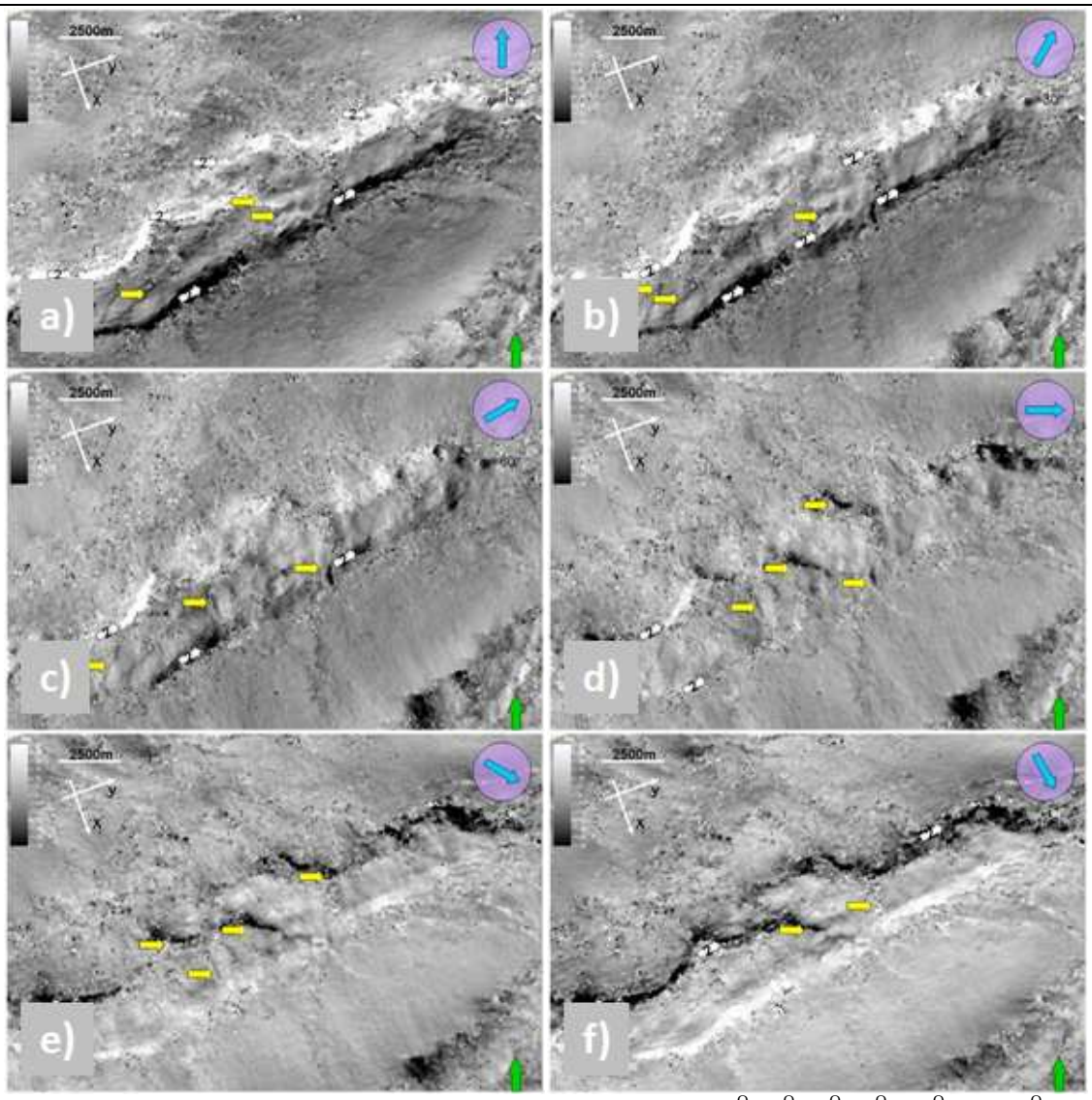


Figure 3: Depth slices at z=2750 m through apparent dip, p_{ψ}, computed at ψ=0^{O}, 30^{O}, 60^{O}, 90^{O}, 120^{O}, and 150$^{O.}$ from North. Block white arrows indicate lineaments that we interpret to be associated with faults and fractures. Several meandering channel segments can be seen in the sedimentary section to the SE.

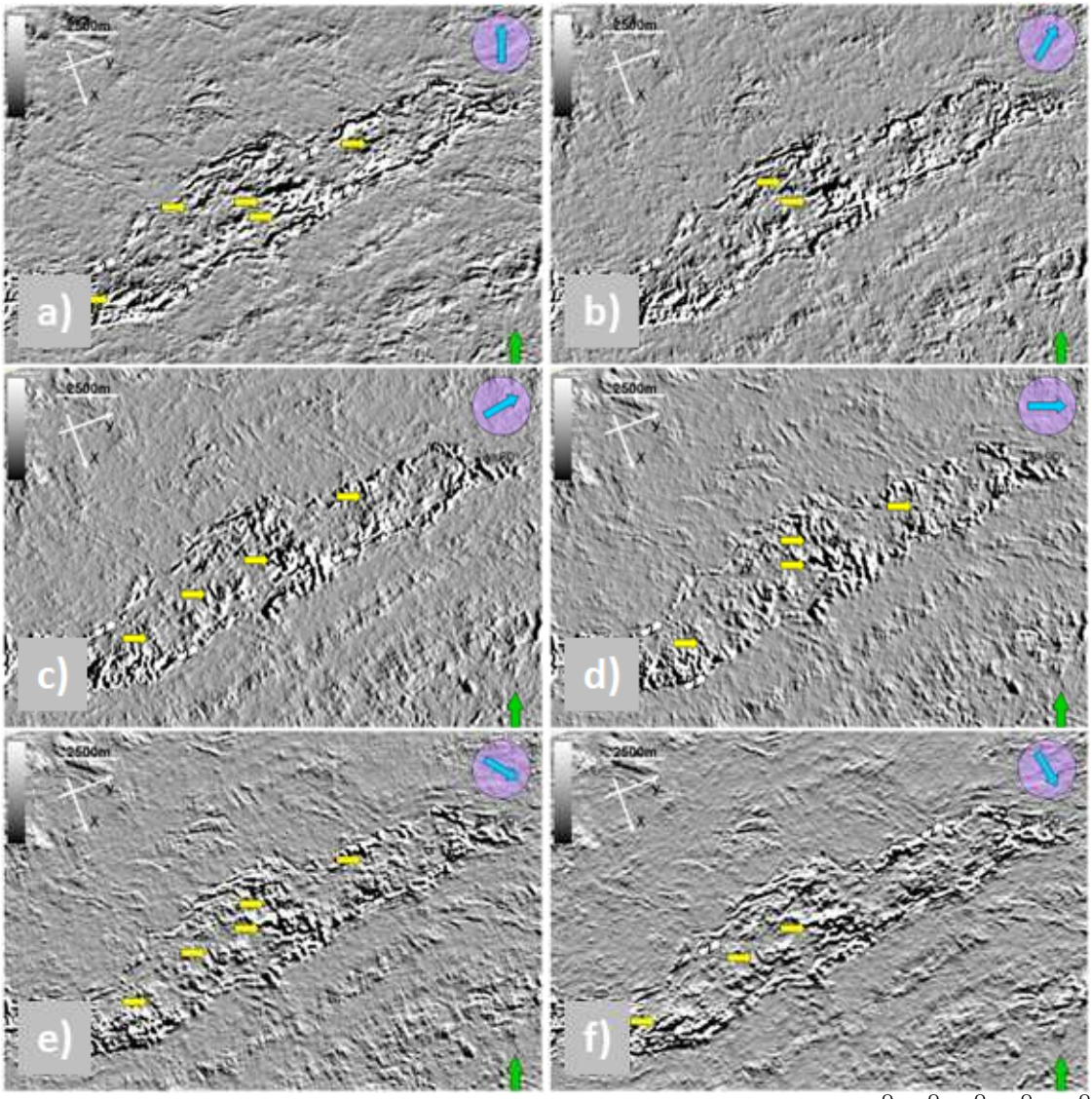


Figure 4: Depth slices at z=2750 m through apparent amplitude gradients, g_{ψ}, computed at ψ=0^{O}, 30^{O}, 60^{O}, 90^{O}, 120^{O}, and 150$^{O.}$ from North. Block white arrows indicate lineaments that we interpret to be associated with faults and fractures. Several meandering channel segments can be seen in the sedimentary section to the SE.



Figure 5: Depth slices at z=2750 m through (a) maximum curvature (b) minimum curvatures and (c) azimuth of minimum curvature.

REFERENCES

Barnes, A. E., 1996, Theory of two-dimensional complex seismic trace analysis: Geophysics, **61**, 264–272.
_____, 2000, Weighted average seismic attributes: Geophysics, **65**, 275–285.
2003, Shaded relief seismic attribute: Geophysics, **68**, 1281–1285.
_____, 2006, Robust estimates of 3D reflector dip and azimuth: Geophysics, **71**, 29–40.
_____, 2007, Seismic attributes for prospect identification and reservoir characterization: SEG.
Chopra, S., and K. J. Marfurt, 2007, Seismic attributes for prospect identification and reservoir characterization: SEG.
Randen, T., E. Monsen, C. Signer, A. Abrahamsen, J. O. Hansen, T. Soeter, J. Schlaf, and L. Sonneland, 2000, Threedimensional texture attributes for seismic data analysis: Presented at the 70th Annual International Meeting, SEG.
Roberts, A., 2001, Curvature attributes and their application to 3D interpreted horizons: First Break, **19**, 85–99.

Attribute illumination of basement faults, examples from Cuu Long Basin basement, Vietnam and the Midcontinent, USA

Ha T. Mai, Olubunmi O. Elebiju, and Kurt J. Marfurt, University of Oklahoma, Norman, USA

Abstract

Geometric attributes such as coherence and curvature have been very successful in delineating faults in sedimentary basins. While not a common exploration objective, fractured and faulted basement forms important reservoirs in Southern California, Mexico, India, Yemen, and Vietnam. Basement faulting controls hydrothermally-altered dolomite in the Appalachian Basin of the USA, and is suspected to play a role in diagenetic alteration of carbonates in the Fort Worth Basin of north Texas where copper has been found in some wells, as well as in Osage County, OK, not far from the classic Mississippi type lead-zinc deposits. Because of the absence of stratified, coherent reflectors, illumination of basement faults is more problematic than illumination of faults within the sedimentary column. In order to address these limitations we make simple modifications to well-established vector attributes including structural dip and azimuth, amplitude gradients, and minimum and maximum curvature, to provide greater interpreter interaction. Using this workflow, we can better illuminate fracture 'sweet spots' and estimate their density and orientation. We apply this workflow to better characterize faults and build fracture models in the granite basement of the Cuu Long Basin, Vietnam, and the granite and rhyolite-metarhyolite basement of Osage County, Oklahoma, USA. Cuu Long forms an important unconventional reservoir. In Osage County, we suspect basement control of shallower fractures in the Mississippi chat deposits.

Introduction

Faults play an important role in forming effective fracture porosity for hydrocarbon traps in the granite basement of the Cuu Long Basin, Vietnam. Mapping fault/fracture intensity and orientation can help delineate sweet spots and better aid horizontal drilling. In the Cuu Long Basin, faults and fractures tend to be planar and steeply dipping, such that we expect to see them more distinctly by viewing them perpendicular to their strike. Interactive shaded-relief maps of picked horizons are provided in nearly all 3D seismic interpretation software packages. Although most easily understood as sun-shading with locally higher relief features creating shadows that enhance the appearance of subtle dips, mathematically, shaded-relief maps comprise simple axis rotations and projection of the two orthogonal dip components of the surface with the direction of illumination

Barnes (2003) showed how volumetric estimates of structural dip and azimuth can be used to generate shaded-relief volumes. We imitate this work, and generate directional structural dip, amplitude gradient, and directional curvature volumes and evaluate the results in terms of basement fault illumination of Cuu Long Basin, Vietnam, and in Osage County, in the Midcontinent region of Oklahoma, USA.

Recently, Singh et al. (2008) showed that the major faults delineated by seismic attributes may not be those associated with fracture permeability. They used an ant-tracking filter to highlight those faults having an azimuth consistent with fractures seen in image logs. Here, we use a simple rotational filter to illuminate faults and fractures having different orientations in an animation loop.

Method

A planar surface such as dipping horizon or faults can be presented by its true dip azimuth θ and strike ψ. The true dip θ can be presented by apparent dips θ_x and θ_y along the x and y axes (Figure 1).

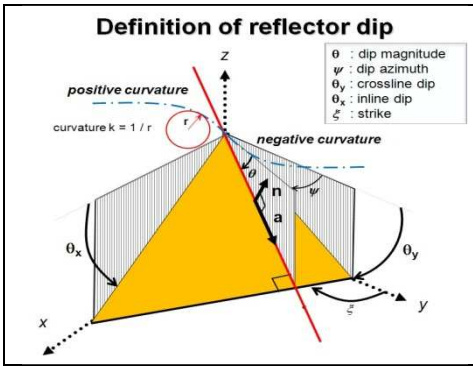


Figure 1: Mathematical, geologic, and seismic nomenclature used in defining reflector dip. By convention, **n** = unit vector normal to the reflector; **a** = unit vector dip along the reflector; θ = dip magnitude; ψ = dip azimuth; ξ = strike; θ_x = the apparent dip in the xz plane; and θ_y = the apparent dip in the yz plane. (after Chopra and Marfurt 2007)

Attribute illumination of basement faults, examples from Cuu Long Basin basement, Vietnam and the Midcontinent, USA

For time-migrated seismic data, it's more convenient to measure apparent seismic time dips (p_x, p_y) components along inline and crossline directions in *s/ft* or *s/m*. For depth-migrated seismic data such as our Cuu Long survey, we simply compute θ_x and θ_y and display them either as components or as dip magnitude, θ, and dip azimuth, ψ, or alternatively as dimensionless (p_x, p_y) measured in ft/ft or m/m.

There are several popular means of computing volumetric dip components, including those based on weighted versions of the instantaneous frequency and wave-numbers (Barnes, 2002), on the gradient structure tensor (Randen et al., 2000) and on discrete semblance-based dip searches (Marfurt, 2006). The relationship between apparent seismic time/depth dips and apparent angle dips are:

$$p_x = 2 * \tan\theta_x \ / \ v, \tag{1a}$$

$$p_x = 2 * \tan\theta_y \ / \ v, \tag{1b}$$

where v is an average time to depth conversion velocity.

We can compute apparent dip at any angle ψ from North through a simple trigonometric rotation:

$$p_\psi = p_x \cos(\psi - \phi) + p_y \sin(\psi - \phi), \tag{2}$$

where ϕ is the angle of the inline seismic axis from North.

Marfurt (2006) also describes an amplitude gradient vector attribute that has inline and crossline components (g_x, g_y). We can therefore compute an amplitude gradient at any angle, ψ, from North:

$$g_\psi = g_x \cos(\psi - \varphi) + g_y \sin(\psi - \varphi). \tag{3}$$

To compute the apparent curvature at an angle, δ, from the azimuth of minimum curvature, χ, we slightly modify Roberts' (2001) description of Euler's formula:

$$k_\delta = k_{\max} \sin^2 \delta + k_{\min} \cos^2 \delta, \tag{4}$$

where k_{min} and k_{max} are the minimum and maximum curvatures. To compute the apparent curvature at an angle ψ, from North we write:

$$k_\psi = k_{\max} \sin^2 (\psi - \chi) + k_{\min} \cos^2 (\psi - \chi) \tag{5}$$

Using equations 2, 3, and 5, we are able to animate through a suite of apparent dip, amplitude gradient, and curvature images at increments of 15^0 to see which perspective best illuminates structural features of interest.

Positive curvature attribute indicate concave downward features, and negative attribute indicate concave upward features. With respect to fault plane, they are usually on one side of the plane, where the reflection boundary is curving most.

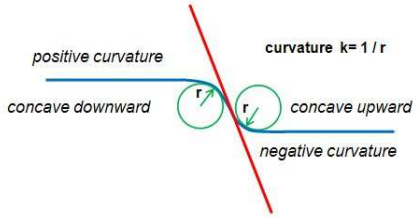


Figure 2: An illustrated definition of 2D curvature. Concave downward features have a positive value while concave upward features have a negative value.

Application

We begin by computing apparent dip, energy-weighted amplitude-gradient methods, and curvature for our 3D post-stack depth-migrated seismic dataset from the Cuu Long basin, Vietnam. The structure of Pre-Cenozoic basement of the Cuu Long Basin is very complex, and is mainly composed of magmatic rocks. Under the influence of tectonic activity, the basement was broken into a suite of fault systems. This faulting provided favorable conditions for hydrocarbons from a laterally deeper Oligocene-Miocene formation to migrate and accumulate in the basement high.

The basement is un-layered granitic rocks, such that the seismic signal appears to be very weak and noisy. We apply our workflow to enhance the faults signatures will aid our seismic interpretation, with the ultimate goal of estimating fracture location, density, and orientation.

The top of basement was highly compressed, forming a high angle push-up to about 2500 m (Figure 3). The top of this basement high dips to the east and west at about 60°. Faults were formed along all sides and cut into the basement (Figure 3).

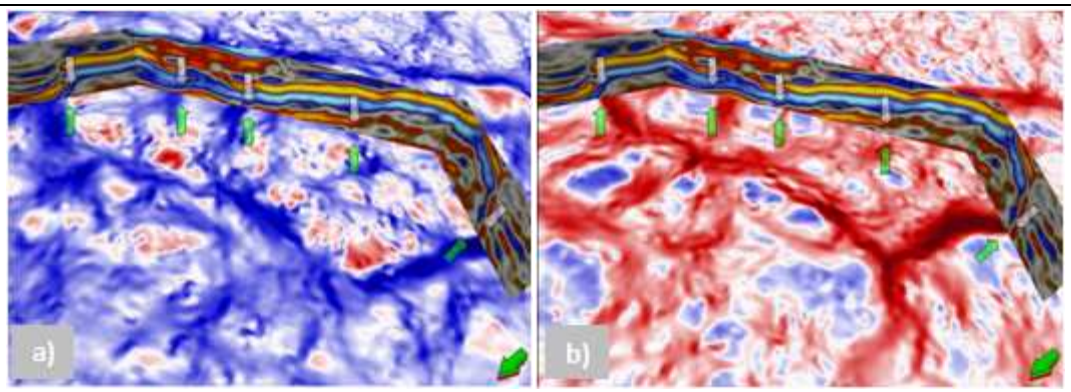


Figure 3: Seismic section on (a) negative curvature and (b) positive curvature depth slice. The arrows show location where the attributes help interpreting fault features

Figure 4 shows depth slices at 2750 m through the apparent dip volume, p_ψ, as a function of azimuth. We used equation 2 to compute images at $\psi = 0^O$, 30^O, 60^O, 90^O, 120^O, and 150^O. White arrows indicate the major NE-SW trending main faults, while yellow arrows indicate more subtle faults cutting across them.

Figure 5 shows depth slices at 2750 m through the apparent amplitude gradient volume, g_ψ, as a function of azimuth. We used equation 3 to compute images at $\psi = 0^O$, 30^O, 60^O, 90^O, 120^O, and 150^O. White arrows indicate lineaments that we interpret to be indicative of subtle faults and fractures. Close to the north azimuth, we see a suite of NE-SW dipping features, which include faults and top basement boundary. The basement edge is dipping rapidly at an angle of about 70^O or more at this location. There are many faults running along this edge that propagate into the shallower sedimentary column. In Figures 5d and 5e, nearly perpendicular to inline direction, we recognize many NW-SE trending features, which we intepret as faults cutting across the basement. These features did not appear in the apparent gradient images parallel to the features.

Investigating the detail faults direction $\psi=0^O$ from North in apparent dip image (Figure 6), we can distinguesh the main SW-NE fault trend. The major faults have a mean direction of 74^0 from North, nearly perpendicular to the 0^O apparent dip direction.

Investigating the detail faults direction $\psi=90^O$ from North in apperant dip image (Figure 7), the SW-NE fault trend becomes less distinguisable. Insread, the faults in N-S trend can be recoginized easier. The major faults have a mean strike of 161^0 from North, nearly perpendicular to the 90^O aparent dip direction.

The apparent amplitude gradients maps behave in an analoguous facture, delineatingfeatures that strike perpendicular to the direction of investigation.. In Figure 8, $\psi=0^O$, the major faults trend 69^0 from North, and at $\psi=90^O$ (Figure 9), the major fault trends at 157^0 from North.

Figure 10 shows depth slices at 2750m through the original seismic, variance, most positive curvature and most negative curvature volumes. The fractured features inside the basement are clearly delineated. White arrows indicate the major NE-SW trending main faults, paralleling and adjacent to the sides of the basement uplift, while yellow arrows indicate more subtle faults cutting across them. Most of the inside faults cutting across the basement are in NW-SE direction.

The Osage county, Oklahoma encompassing the Osage Indian Reservation is located west of Ozark uplift and east of the Nemaha uplift. Within the Indian reservation, Precambrian basement surface is an irregular erosional surface with series of domes overlain by Paleozoic rocks (Thorman et al., 1979). Precambrian structure identified (The Labette fault) within the basement has a predominantly NE-SW trending direction (Denison, 1981).

Previous work within this areas have suggested a possible reactivation of these structure and other Paleozoic structures such as the Nemaha Uplift (locally referred to as the Humboldt Fault) (Luza et al., 1983). The Nemaha uplift consists of complex units of crustal uplift with NE, NW trending structures. An E-W trending dextral strike-slip fault supported by aeromagnetic data has been inferred south of the Labette fault. This structure is suggested to offset the Nemaha Uplift

Figure 11 shows the complex nature of faults and fractures that plaque the Osage county sedimentary section. Comparing the basement feature at approximately 700 ms and networks of lineaments seen at about 630 ms indicates that in addition to the NE-SW and dominantly E-W trending lineaments seen within the basement, NW-SW lineaments predominates the sedimentary section at 630 ms which might correspond to the Arbuckle group.

The NW-SE lineaments cross cut the other lineaments present and we suggest that it is younger in age. Thus, the NW-SE lineaments represent the latest event in the area. The presence of such lineament in both basement and sedimentary section, suggested that they post-date both basement and the penetrated sedimentary section. It will be interesting to see if the location of such NW-SE lineaments coincides with the weak zone of intensely sheared or mylonitized Precambrian basement. Luza et al. (1983) have revealed that the Precambrian basement beneath the Nemaha fault is strongly mylonitized and sheared.

Figure 12 shows a time slices at 700 ms, right below the Precambrian basement, through seismic, variance, most positive curvature and most negative curvature volumes from Osage county. The white arrows indicate distinctive primary fault features in NE-SW direction and yellow arrows indicate the later faults in E-W or ESE-WNW direction The faults extend upward into the sedimentary layers above the basement. Figure 13 shows times slices at 630ms, above basement top, thought the same volumes. We can see the same faults pattern in NE-SW and E-W directions, in a higher contrast, as of the less-complexity of the sedimentary layers.

Figure 14 shows an NE-SW and in E-W trending lineament over inline and crossline amplitude gradient at 700ms (bellow basement top) and 630ms (above basement top).

Evidently, we suggested that the NW-SE features as part of the reactivated faults that crosscut inherent NE-SW network basement lineaments. From magnetic study, similar NW trending fault (e.g Creek County Fault) is identified southwest of the Osage Indian Reservation area.

The attribute analysis has helped us to identify basement lineament, which will not have been possible in ordinary seismic data. The correlation of basement lineaments with sedimentary lineament might suggest a basement influence on some of the sedimentary lineaments.

Conclusions

Volumetric computation of structural dip and azimuth, structural curvature, amplitude gradients, and amplitude curvature, are multi-component in nature and are thus amenable to visualization from different user-controlled perspectives. By defining a suite of azimuths to investigate, the interpreter can enhance subtle faults and fractures that might otherwise be missed, or that are more likely to be open rather than sealed.

Acknowledgments

We thank PetroVietnam and Cuu Long JOC, as well as the Osage Indian Nation for providing seismic data, and allowing us to publish the results used in this report. The rotation of the images was achieved through the use Stanford's SEPlib mathematic utility, and the slice images are generated using of Schlumberger's Petrel. The Rose diagrams were generated using Dr. R. J. Holocombe's GEOrient software.

References

Barnes, A. E., 1996, Theory of two-dimensional complex seismic trace analysis: Geophysics, **61**, 264-272.

_____, 2000, Weighted average seismic attributes: Geophysics, **65**, 275–285.

_____, 2003, Shaded relief seismic attribute: Geophysics, **68**, 1281–1285.

Chopra, S., and K.J. Marfurt, 2007, Seismic attributes for prospect identification and reservoir characterization: Geophysical Developments 11, Society of Exploration Geophysicists.

Denison, R. E., 1981, Basement rocks in Northeast Oklahoma: Oklahoma Geological Survey Circular **84**.

Luza, K. V., and J.E. Lawson, 1983, Seismicity and tectonic relationships of the Nemaha Uplift in Oklahoma Part V.

Marfurt, K. J., 2006, Robust estimates of 3D reflector dip and azimuth: Geophysics, **71**, 29-40.

Randen, T., E. Monsen, C. Signer, A. Abrahamsen, J. O. Hansen, T. Soeter, J. Schlaf, and L. Sonneland: 2000, Three-dimensional texture attributes for seismic data analysis, 70th International Meeting, SEG, Expanded Abstracts, 19, 668-671.

Roberts, A., 2001, Curvature attributes and their application to 3D interpreted horizons. First Break, **19**, 85-99.

Singh, S. K., H. Abu_Habbiel, B. Khan, M. Akbar, A. Etchecopar, and B.Montaron, 2008, Mapping fracture corridors in naturally fractured reservoirs: an example from Middle East carbonates: First Break, **26**, no. 5, 109-113.

Thorman, C. H., and M.H. Hibpshman, 1979, Status of mineral resource information for the Osage Indian Reservation, Oklahoma: Administrative Report BIA-47, U.S. Geological Survey and Bureau of Mines.

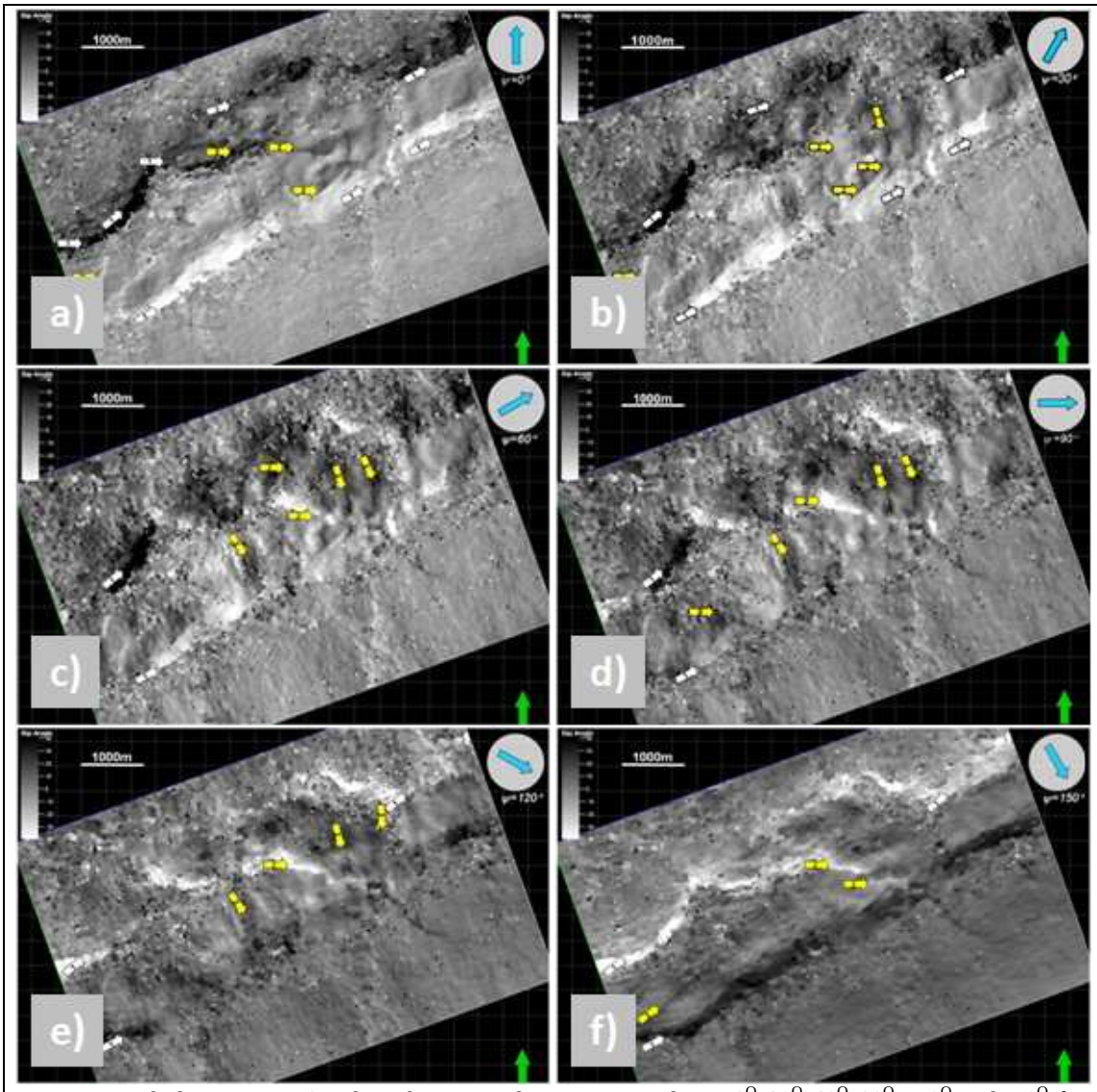


Figure 4: Depth slices at z=2750 m through apparent dip, p_ψ, computed at ψ=0^O, 30^O, 60^O, 90^O, 120^O, and 150$^{O.}$ from North. Block white arrows indicate lineaments that we interpret to be associated with faults and fractures. Several meandering channel segments can be seen in the sedimentary section to the SE. Cuu Long basin

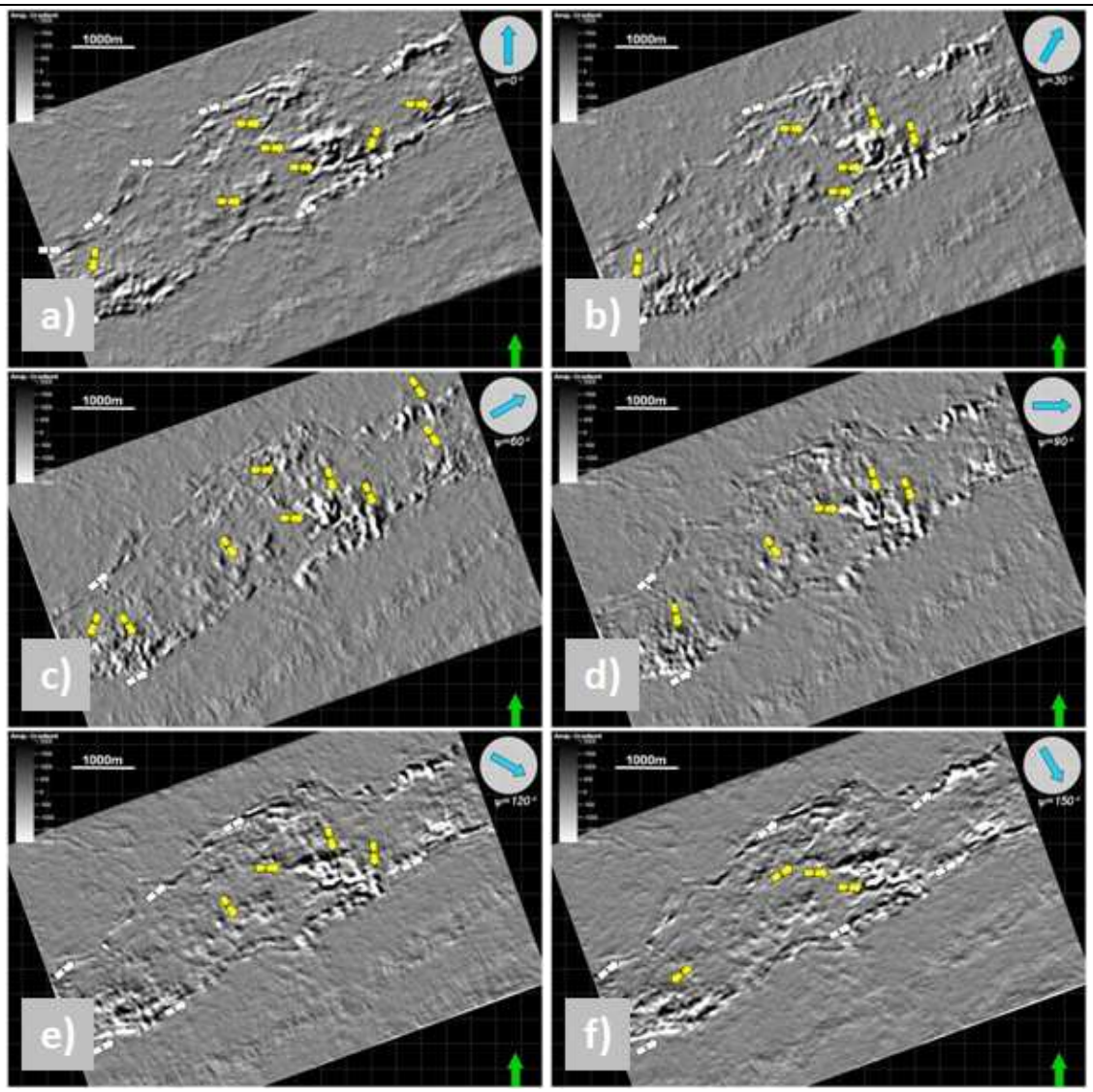


Figure 5: Depth slices at z=2750 m through apparent amplitude gradients, g_{ψ}, computed at ψ=0^{O}, 30^{O}, 60^{O}, 90^{O}, 120^{O}, and 150$^{O.}$ from North. Block white arrows indicate lineaments that we interpret to be associated with faults and fractures. Several meandering channel segments can be seen in the sedimentary section to the SE. Cuu Long basin

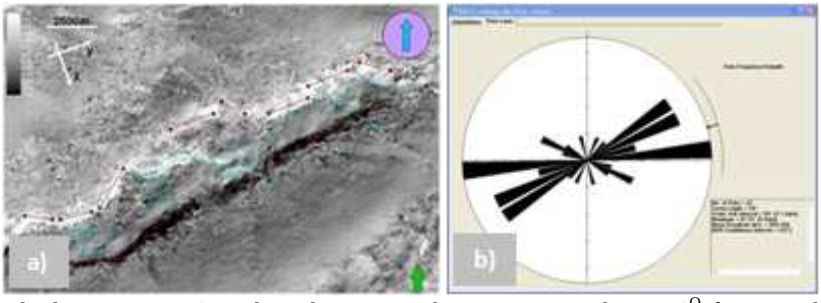


Figure 6: (a) Depth slices at z=2750 m through apparent dip, p_{ψ}, computed at ψ=0^{O} from North. (b) Major fault frequency detected in direction ψ=0^{O}. Mean direction of faults detected in this case is about 74^{0}. Cuu Long basin

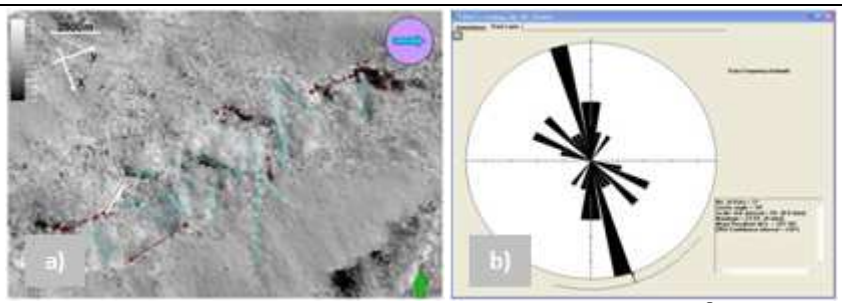


Figure 7: (a) Depth slices at z=2750 m through apparent dip, p_ψ, computed at ψ=90^O from North. (b) Major fault frequency detected in direction ψ=90^O. Mean direction of faults detected in this case is about 161^0. Cuu Long basin

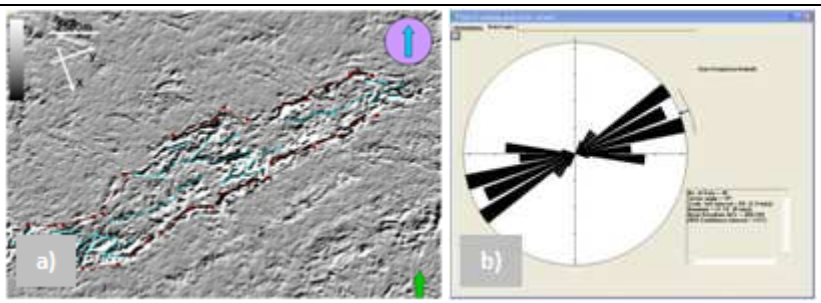


Figure 8: (a) Depth slices at z=2750 m through apparent amplitude gradients, p_ψ, computed at ψ=0^O from North. (b) Major fault frequency detected in direction ψ=0^O. Mean direction of faults detected in this case is about 69^0. Cuu Long basin

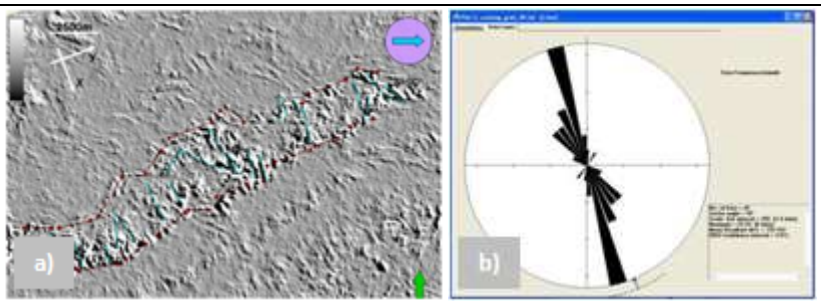


Figure 9: (a) Depth slices at z=2750 m through apparent amplitude gradients, p_ψ, computed at ψ=90^O from North. (b) Major fault frequency detected in direction ψ=90^O. Mean direction of faults detected in this case is about 157^0. Cuu Long basin

Attribute illumination of basement faults, examples from Cuu Long Basin basement, Vietnam and the Midcontinent, USA

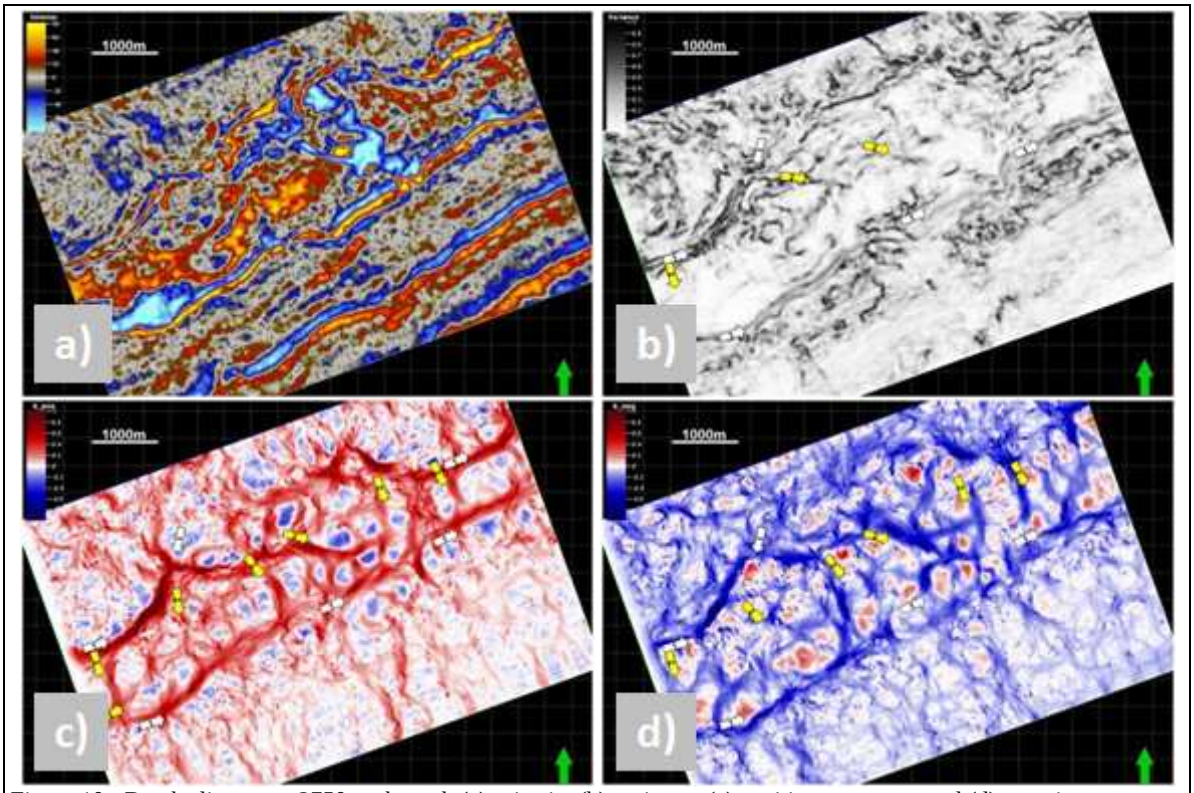


Figure 10: Depth slices at z=2750 m through (a) seismic, (b) variance, (c) positive curvature, and (d) negative curvature – Cuu Long basin

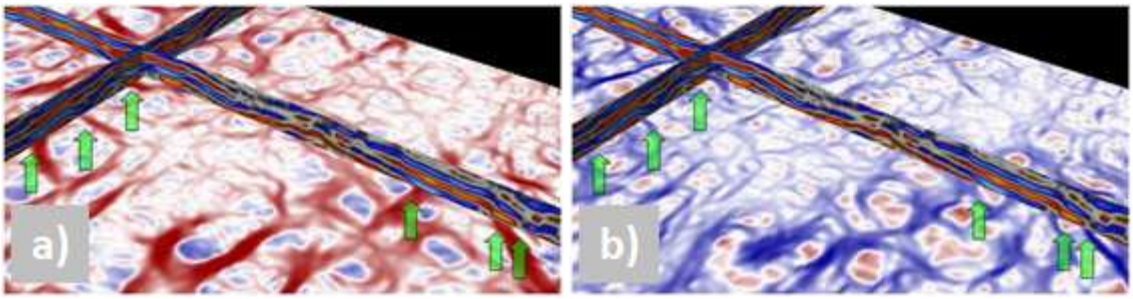


Figure 11: Seismic section on (a) negative curvature and (b) positive curvature time slice. The arrows show location where the attributes aided fault interpretation - Osage county

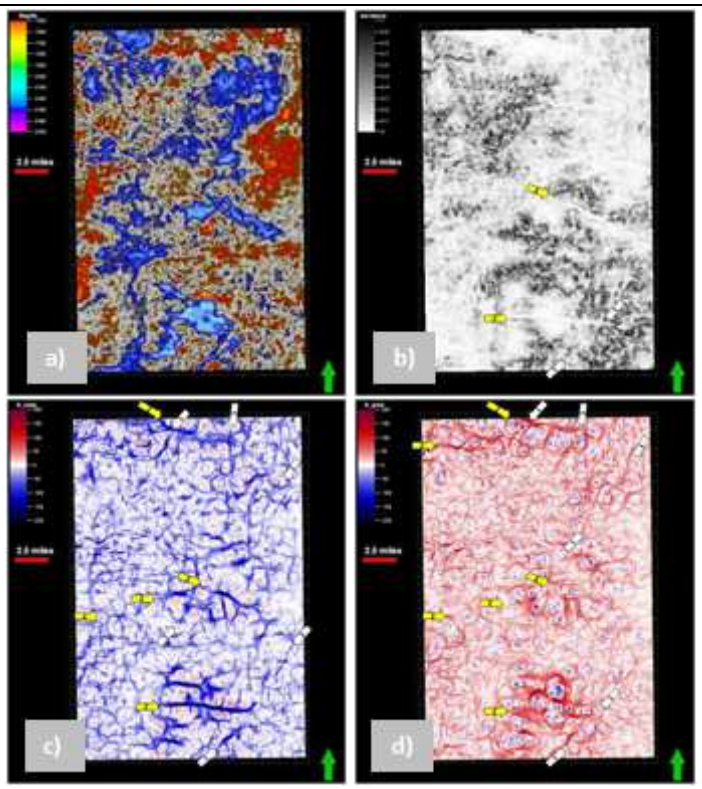


Figure 12: Time slices at z=700ms through (a) seismic, (b) variance, (c) negative curvature, and (d) positive curvature. Osage county

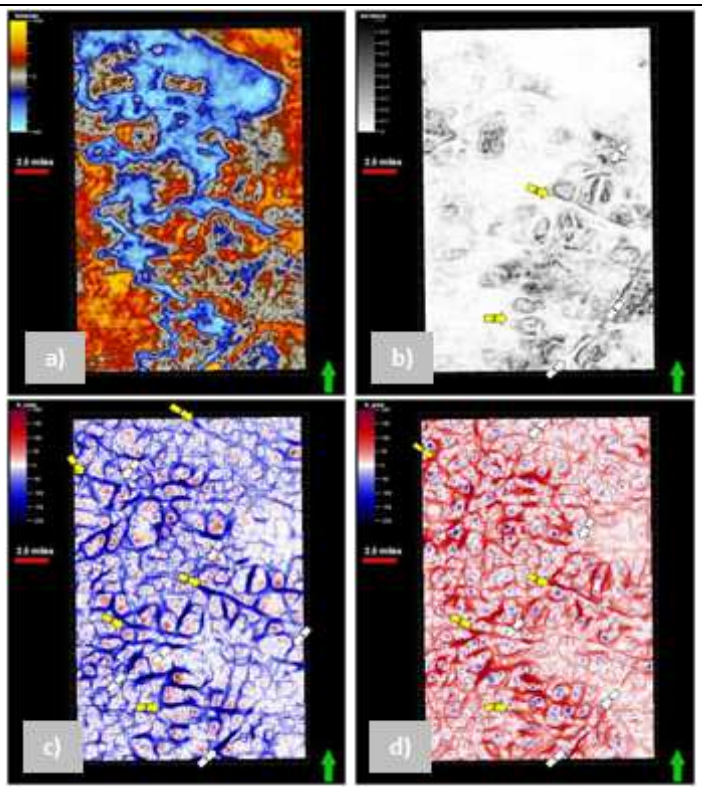


Figure 13: Time slices at z=630 ms through (a) seismic, (b) variance, (c) negative curvature, and (d) positive curvature. Osage county

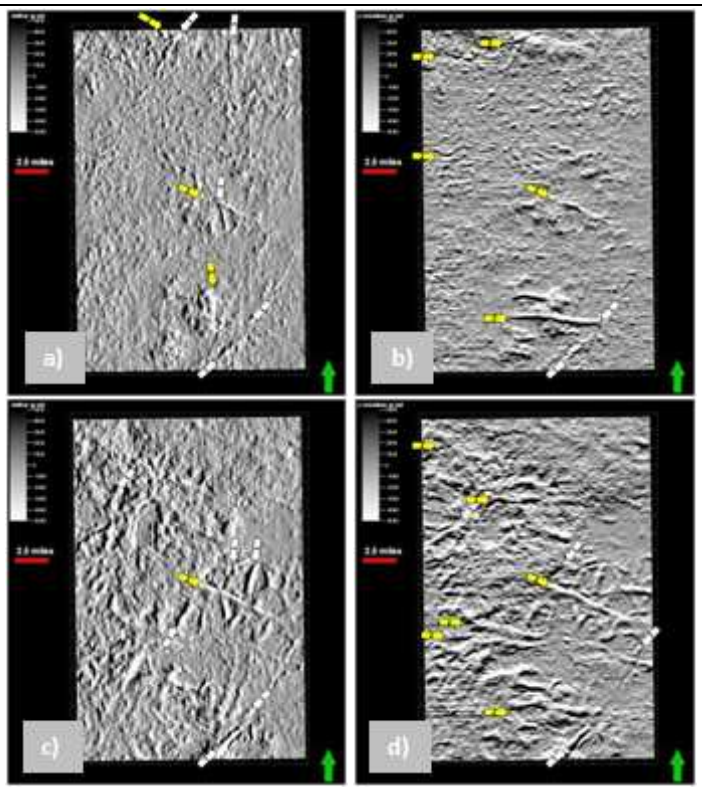


Figure 14: Time slices at 700ms through (a) inline amplitude gradient, (b) crossline amplitude gradient and Time slices at 630ms through (a) inline amplitude gradient, (b) crossline amplitude gradient. Osage county

Curvature lineaments and multi-attribute display of full-stack PP, SS, and acoustic impedance seismic data – Diamond-M field, West Texas

Ha T. Mai, Carlos F. Russian, Kurt J. Marfurt, Roger A. Young, University of Oklahoma, Norman, USA; Alison Weir Small, Parallel Petroleum Corp.*

Summary

Geometric attributes are routinely used in mapping tectonic deformation and geomorphology. AVO and inversion analysis is routinely used to map lithology and the presence of hydrocarbons. We apply geometric attributes to angle-stack and full-stack PP and SS as well as acoustic impedance inversion volumes over the Diamond M survey, Horseshoe Atoll, west Texas, and find lineaments corresponding to the edges of the Pennsylvanian-age reef structure.

Introduction

The large subsurface feature termed the Horseshoe Atoll, located in the Midland Basin of west Texas, is a series of primarily Missourian and Virgilian-age carbonate reservoirs (Reid, 2001). The data available for this research covers part of the Diamond-M field which lies in the Scurry Reef Trend in Scurry Co., Texas (Figure 1). Since the development of the Kelly-Snyder oil field, exploration has moved southeast of the atoll in search of small reef bodies (Jumper and Pardue, 1996). Our goal is to evaluate the effectiveness of curvature-related lineaments in better defining reef edges as well as internal fractures within the reefs.

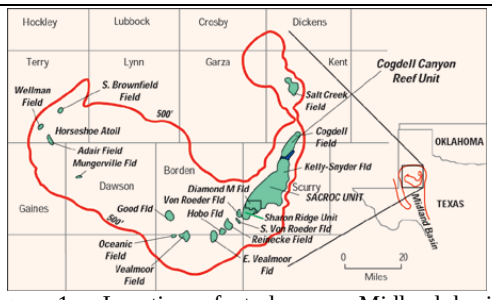


Figure 1: Location of study area, Midland basin, Texas. (after WorldOil.com)

Theory and Method

Curvature of a surface is measured by the radius of two circles tangent to it. The circle with the tightest radius defines the maximum curvature (k_{max}) while the circle perpendicular to it defines the minimum curvature (k_{min}). In further clarification, k_{max} of a surface with an anticlinal shape has a positive value, while k_{max} of a surface with synclinal shape has a negative value (Figure 2). Also, the intersection of the plane containing the circle defining minimum curvature with the horizontal defines a strike, which is commonly referred to as the azimuth of minimum curvature, ψ_{min}.

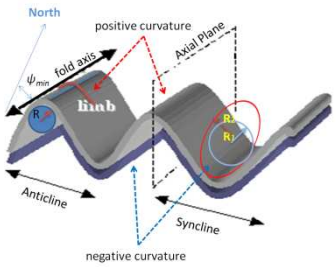


Figure 2: An illustrated definition of 3D curvature. Synclinal features have negative curvature and anticlinal features have positive curvature. (After Lisle, 1994).

A folded surface can be further defined as having a certain shape, measured by the shape index (e.g Roberts, 2001). Furthermore, the long axis of elongated domes, ridges, saddles, valleys, or elongated bowls corresponds to ψ_{min}. By modulating the shape indices with the curvedness, c, (where $c^2=k_{min}^2+k_{max}^2$) Al-Dossary and Marfurt (2006) show how we can generate different shape components.

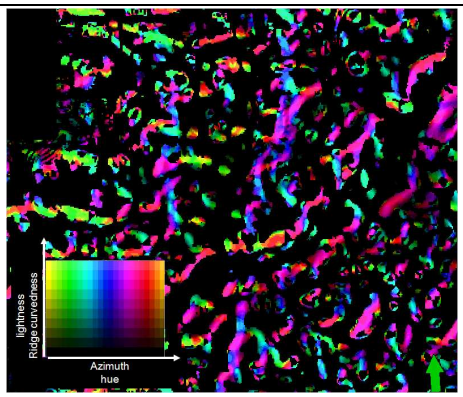


Figure 3: 2D multi-attribute display. The ridge component of curvedness is plotted against lightness and modulates the azimuth of minimum curvatures, ψ_{min}, plotted against hue.

Combining multiple attributes in a single image allows us to visually 'cluster' mathematically different attributes that are sensitive to the same underlying geology. In Figure 3, we show a composite image of the ridge component of curvedness, c_r, and ψ_{min}.

For a more conventional display of these lineaments, we generate rose diagrams for any defined *n-inline* by *m-crossline* analysis window. Within each analysis window, we threshold the ridge or valley components

of curvedness, c_r, or c_v,, bin each voxel according to its azimuth, ψ_{min}, and sum the threshold-clipped values of the ridge or valley components, thereby generating volumetric rose diagrams over a suite of windows spanning the entire seismic volume (Figure 4).

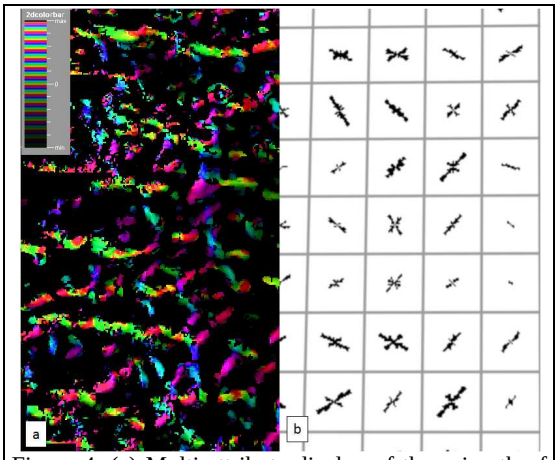


Figure 4: (a) Multi-attribute display of the azimuth of minimum-curvature, ψ_{min}, modulated by the ridge component of curvedness and (b) the corresponding rose diagrams.

Data

We apply this simple work flow to three different data types for this project: the PP full stack, the SS full stack, and the acoustic impedance (AI) derived from a model-based sequential inversion. The zone of interest is isolated to a single time slice below the top of the Canyon Reef Formation where isolated reef build-up structures can be found. To this end, we analyze both the conventional P-wave and the more experimental S-wave (SH-SH) data volumes over the approximately 25 mi^2 (~65 km^2) of the Diamond M field described by Small et al. (2007). Both data volumes have a high signal-to-noise ratio and have been pre-stack time migrated onto 75 ft x 75 ft (22 x 22 m) CMP bins.

The P-wave data was subjected to a model-based impedance inversion that used the well control to increase the overall bandwidth of the data. We anticipate that attributes computed from this acoustic impedance volume may illuminate structural lineaments not seen on the seismic reflection data.

Interpretation

The time-structure map corresponding to the top of the Canyon Reef Formation (Figure 5) gives a general idea of structure alignment related to the reef build up formation. The map shows a central big reef that expands laterally towards the eastern portion of the survey. Also, in the SE portion of the survey we can identify a smaller reef build up. Using the previously-defined workflow, we are not only able to estimate the outer most edges of the reef structure but also lineaments that might suggest the inner fabric and depositional control of this Pennsylvanian-age reef.

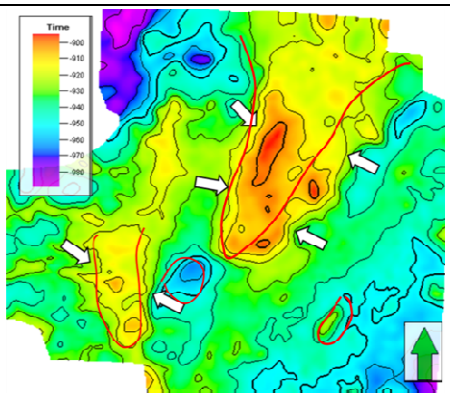


Figure 5: Time structure map coresponding to top of Pennsivanian age Canyon Reef formation, interpreted from the PP seismic data.

Nissen et al. (2007) have shown that volumetric curvature can delineate karst-enhanced fractures in the Fort Worth Basin, Central Kansas, and Western Kansas. Our goal here is to apply the described workflow to the three different data sets, thereby highlighting structural features such as minor reef build-ups or karst-enhanced fractures not previously seen.

We begin our interpretation with the PP data set, and include interpretation of what the authors interpret to be reef associated lineaments (Figure 6). Note the correlation of the most positive curvature anomalies and the edges of the central reef. Furthermore, interpretation of the western portion of the survey suggests that the previously identified reef structure continues to the west. This trend is also seen on the most negative curvature image. In most-positive and most-negative curvature blended image (Figure 6c), besides edges of the reef, we see indications of a reef talus slope deposited in the eastern flank of the central reef (white arrows) correlating to high amplitude respond on the amplitude map. In addition, we generate 2D multi-attribute display, combining ridge curvedness with minimum curvature azimuth, and overlaying with volumetric rose diagrams (Figure 6d). This composite display, helps visualizing lineaments, with their intensity and orientation, which not only corresponds to the reef's edges, but also potentially indicates inner-structure compartmentalization of the reef.

Although the lineaments from the PP and SS data volumes are similar, detailed comparison suggests that lineaments differ in some areas. In Figure 7, it can be seen that the most westerly lineaments (green arrows) cannot be detected and a central valley (black arrow) is not apparent. On the other hand, the SS dataset allows improved interpretation of the central "main" reef since the edges are better resolved and defined. Subsequent rose diagrams (Figure 7d) better define lineaments associated to the central reef.

Interpretation over acoustic impedance can lead to a more straight forward definition of lineaments, since the wavelet side lobes are strongly attenuated in the inversion process. Hence, the better delineation of the lineaments associated with the central main reef in Figure 8 (a-d), western reef build up, valley between the buildup reef previously denoted on Figure 7, and SE smaller patch reef showing very symmetrical and circular lineaments. As would be expected on the acoustic impedance results, there is a better definition of intensity and orientation when analyzing the rose diagrams (Figure 8d).

Conclusions

Volumetric curvature for lineament determination and multi-attribute display shows differences on the three different surveys: PP, SS, and Acoustic Impedance. Reef related structures were identified as their edges correspond to curvature lineaments. Sub-lineaments cutting reef edges suggest the possibility of compartmentalization, an interpretation that needs to be confirmed with production data. Curvature lineaments are more continuous in the acoustic impedance inversion volume.

Acknowledgments

The authors would like to acknowledge Parallel Petroleum Corporation for providing the data for this research, and the sponsors of the OU Attribute Assisted Seismic Processing and Interpretation (AASPI) consortium. Thanks to Schlumberger for providing OU with licenses to Petrel used in the interpretation and display.

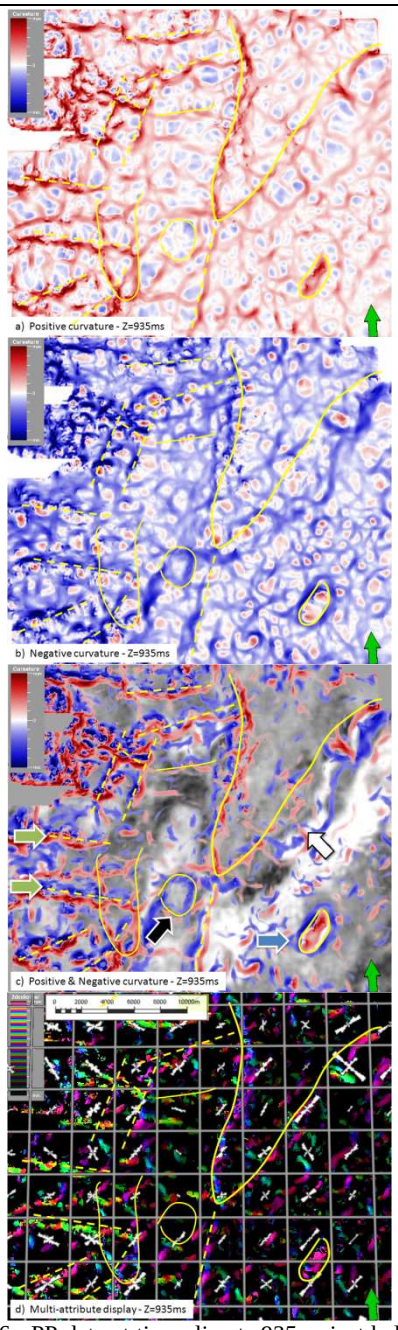


Figure 6: PP data at time slice *t=935ms* just below the top of the Canyon Reef Fm through (a) most-positive and (b) most- negative curvature volumes. (c) Multi-attribute display using transparency to show anomalous features seen in (a) and (b) on top of the seismic amplitude time slice. (d) Multi-attribute ridge-ψ_{min}› display described in Figure 3 overlain by rose diagrams (in white).

Curvatures lineament and multi-attribute display of full-stack PP, SS, and Acoustic Impedance seismic data – Diamond-M field, West Texas

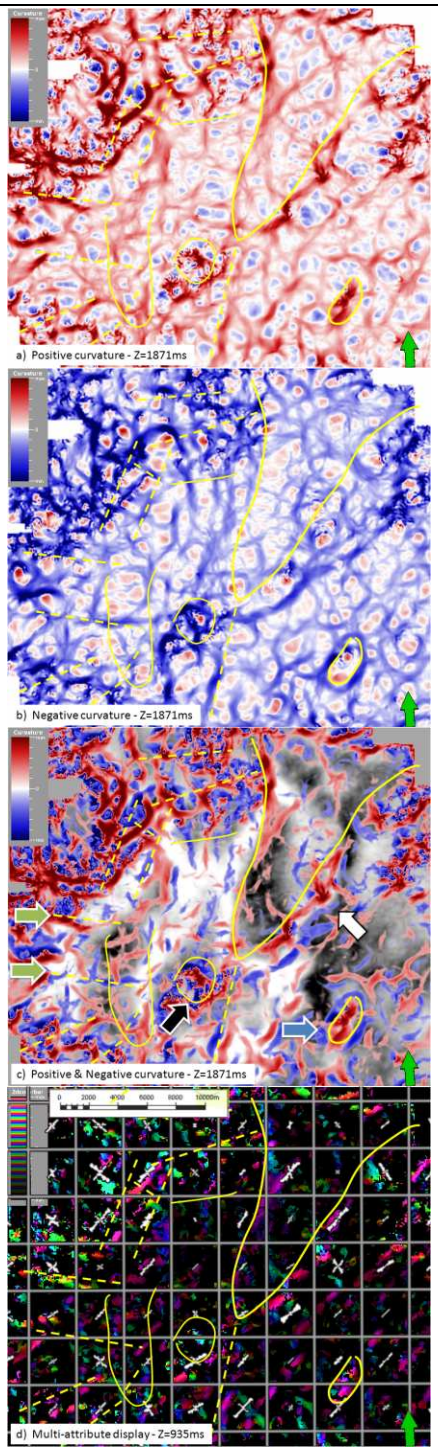


Figure 7: SS data at time slice *t=1871ms* (just below the top of the Canyon Reef Fm and equivalent to 935ms in PP data) through Reef Fm through (a) most-positive and (b) most- negative curvature volumes. (c) Multi-attribute display using transparency to show anomalous features seen in (a) and (b) on top of the seismic amplitude time slice. (d) Multi-attribute ridge-ψ_{min}, display overlain by rose diagrams (in white).

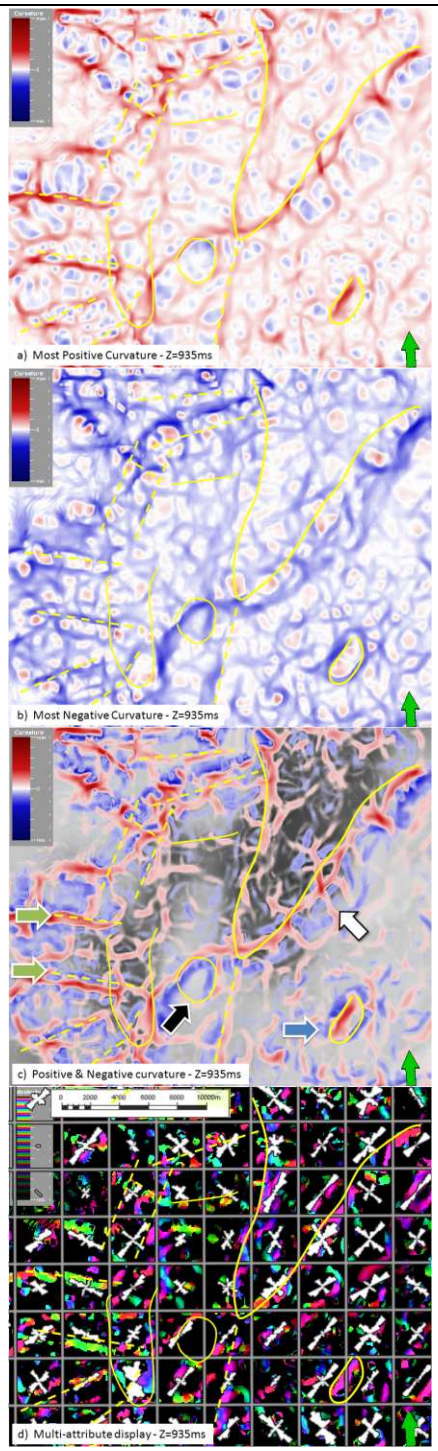


Figure 8: Acoustic Impedance data at time slice *t=935ms* just below the top of the Canyon Reef Fm through (a) most-positive and (b) most- negative curvature volumes. (c) Multi-attribute display using transparency to show anomalous features seen in (a) and (b) on top of the seismic amplitude time slice. (d) Multi-attribute ridge-ψ_{min}, display overlain by rose diagrams (in white).

REFERENCES

Al-Dossary, S., and K. J. Marfurt, 2006, 3-D volumetric multispectral estimates of reflector curvature and rotation: Geophysics,**71**, no. 5, P41–P51.

Blumentritt, C. H., K. J. Marfurt, and E. C. Sullivan, 2006, Volume-based curvature computations illuminate fracture orientations Early to mid-Paleozoic, Central Basin Platform, west Texas: Geophysics, **71**, no. 5, B159–B166.

Lisle, R. J., 1994, Detection of zones of abnormal strains in structures using Gaussian curvature analysis: AAPG Bulletin, **78**,1811–1819.

Nissen, S. E., E. C. Sullivan, K. J. Marfurt, and T. R. Carr, 2007, Improving reservoir characterization of karst-modified reservoirs with 3-D geometric seismic attributes: Mid-Continent Section Meeting, AAPG, Abstract.

Reid, A. M., S. T. Reid, S. J., Mazzullo, and S. T. Robbins, 1988, Revised fusulinid biostratigraphic zonation and depositional sequence correlation, subsurface Permian Basin: AAPG Bulletin, **72**, no. 1, 102.

Jumper, S. C., and H. W. Pardue, 1996, A 3-D case history in the Horseshoe Atoll area of Scurry County, Texas: Applications of 3-D seismic data to exploration and production: AAPG Studies in Geology, **42**, 155–159.

Small A. W., J. W. Thomas, S. Conway, C. Mosher, R. Olson, and D. Whitmore, 2007, HFVS technology applied to a 3D multicomponent seismic project: 77th Annual International Meeting, SEG, Expanded Abstracts, 1014–1018.

Coherence and volumetric curvature and their spatial relationship to faults and folds, an example from Chicontepec basin, Mexico

Ha T. Mai, Kurt J. Marfurt, University of Oklahoma, Norman, USA, Sergio Chávez-Pérez, Instituto Mexicano del Petróleo*

Summary

Geometric attributes such as coherence and volumetric curvature are commonly used in delineating faults and folds. While fault patterns seen in coherence, most-positive curvature and most-negative curvature are easily recognized on time slices, they are often laterally shifted from each other. The kind and degree of lateral shift is an indication of the underlying tectonic deformation. In this tutorial, we document some of these relationships when applied to the structurally-complex section within the Chicontepec Basin, Mexico.

Introduction

While coherence attributes measure lateral changes in the waveform and allow us to map reflector offsets, lateral changes in stratigraphy, and chaotic depositional features, volumetric curvature attributes measure lateral changes in dip magnitude and dip azimuth, and are thus allows us to map folds, flexures, buildups, collapse features, and differential compaction. Both attributes are used widely in detecting faults with each attribute has its advantages and disadvantages. Coherence accurately tracks vertical faults cutting coherent seismic reflectors. For dipping faults, coherence exhibits a vertically-smeared stair-step appearance, due to most implementations being computed on vertical seismic traces. Where there is fault drag, or sub-seismic resolution antithetic faulting that appears as fault drag, coherence may not illuminate the fault at all. For faults with very small displacement, the reflectors appear to have subtle change in dip, have no coherence anomaly, and rather appear as a slight flexure which appears as a curvature anomaly. For faults having significant offset, curvature anomalies track the folds on either side of a fault, where drag, antithetic faulting, or syntectonic deposition results in slightly folded reflectors. For this reason, curvature anomalies often do not align with faults.

Since faults are often more easily visualized on attribute time slices, we will use a complexly folded and faulted survey acquired in the Chinconetepec Basis, Mexico, to illustrate some of these interpretational features..

Theory

Curvature in 2D is defined by the radius of a circle tangent to a curve (Figure 1, after Roberts, 2001). In 3D, we need to fit two circles tangent to a surface (Figure 2). The circle with minimum radius is the maximum curvature (k_{max}) and the circle with maximum radius is the minimum curvature (k_{min}). In relation to geology, anticlinal features will have positive maximum curvature, and a synclinal feature will have negative maximum curvature.

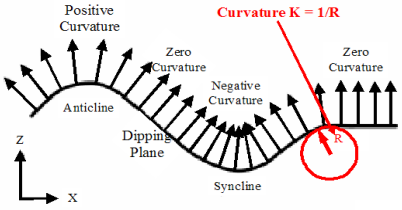


Figure 1: An illustrated definition of 3D curvature. Synclinal features have negative curvature and anticlinal features have positive curvature

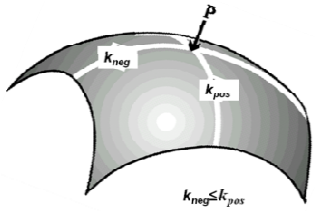


Figure 2: Most-positive and most-negative curvatures (Modified from Lisle, 1994)

The interpretation of curvature volumes computed over folded geologies is straightforward. For anticlines, we see a positive curvature lineament along the fold axis and two negative curvature lineaments at the limbs. For synclines, we see a negative curvature lineament along the fold axis and two positive curvature lineaments along the limbs (Figure 3). Since the layers are continuous, the waveform is also continuous along the fold, such that discontinuity measurements such as coherence do not show any anomalies.

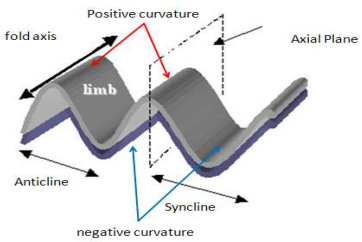


Figure 3: Illustration of fold with positive and negative curvature.

The attribute expression of faults can be considerably more complicated. For normal faults with vertical displacements greater than half a seismic wavelength, we often see a discrete discontinuity that is clearly delineated by a low coherence lineament. For highly competent rocks we may see no curvature anomalies associated with a simple normal fault. However, more commonly we see drag on either side of the fault, which may be either through plastic deformation or through a suite of conjugate faults. Parallel to the fault strike, we often have ramp structures. For an excellent outcrop analysis of such features we direct the reader to a recent publication by Ferrill and Morris (2008). A schematic of curvature associated with normal faults is shown in Figure 4.

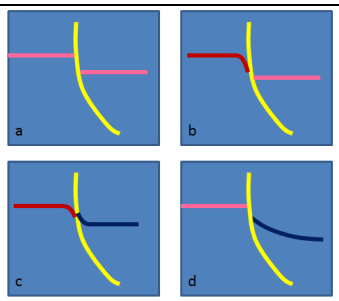


Figure 4: An illustration of normal faults with positive and negative curvature: (a) simple displacement with no drag, (b) fault with drag on one side, (c) fault with drag on two sides, and (d) fault with syntectonic depositions.

Listric faults geometries associated with syntectonic deposition can be considerably more complicated. On the footwall, we may see very little deformation, with the sediments maintaining their original attitude at some angle to the fault face. On the hanging wall, the reflectors rotate with depth, often maintaining a near-normal relation to the fault face. We may also see a positive curvature anomaly over the roll-over anticline if one exists. Coherence does a good job of delineating the fault dislocation. Deeper in the section, as the fault begins to sole out, both coherence and curvature images become noisy and less easily interpreted.

Alternative definitions of maximum and minimum curvature

Most references (in both mathematics and geology) define the maximum curvature to be the tightest (highest absolute value) of the two principal curvatures, k_1 and k_2:

$$k_{max} = k_1 \text{ and } k_{min}=k_2, \text{ if } |k_1| > |k_2|$$
$$k_{max} = k_2 \text{ and } k_{min}=k_1, \text{ if } |k_2| > |k_1|.$$

Many interpreters find this definition to be an effective means of mapping fault throw from time slices (e.g. Sigisumundi and Soldo, 2003). However, other workers (e.g. Rich, 2008) find it to be interpretationally useful to define $k_{max} = MAX(k_1,k_2)$ and $k_{min} = MIN(k_1,k_2)$.

The second author has long favored most-positive and most-negative curvature since they provide images of karst and differential compaction that are interpretational simpler to understand. Rich (2008) points out that this 2nd (less common) definition, produces images similar to most-positive and most-negative curvature, but take account of the reflector rotation.

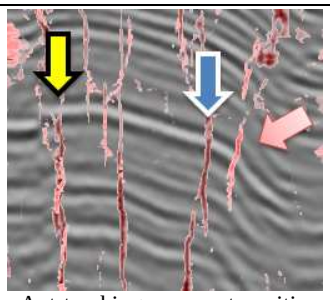


Figure 5: Ant-tracking on most-positive curvature (red, with blue arrow) and on new defined maximum curvature (pink, with pink arrow).

Figure 5 shows the results of ant-tracking applied to most-positive and the newly-defined maximum curvature. The latter shows the axis of a dipping flexure (pink arrow) while the most-positive shows the axis of a less geologically-interesting fold with respect to the horizontal. In gently dipping areas such as in the Fort Worth Basin, k_{max} and k_{pos} are nearly identical (Figure 5, yellow arrow).

Example from Chicontepec basin, Mexico

In order to illustrate the lateral relationship of our new definitions of maximum and minimum curvature with and coherence, we use 3D seismic data from Amatitlán, Chicontepec basin.

Multiple volumetric attributes (k_{pos}, k_{neg}, k_{max}, k_{min}, ψ_{min}, energy ratio coherence, and variance) were calculated from the seismic volume. Where indicated in the captions, a commercial "ant-tracking" image processing algorithm was applied to the attributes to "skeletonize" the image, thereby increasing the visual continuity for interpretation purposes.

Figure 6 shows an anticlinal feature. Since there is no interruptions present along the interpreted horizon (white dashed line), there are no significant coherence anomalies present. However, the dip does change along the horizon such that we see maximum curvatures anomalies along the fold axis, and minimum curvature anomalies along the fold limbs.

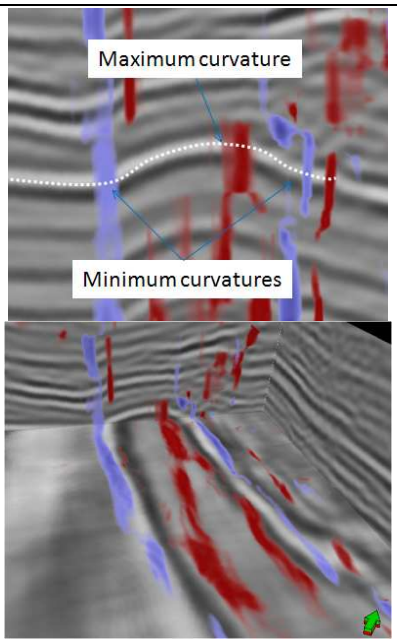


Figure 6: Anticlinal feature. Minumum curvature features (blue) delineate the two limbs of the fold, while maximum curvature (red) delineate the axial plane.. There are no significant coherence anomalies.

For fault features, the interpretation is much more complicated. Figures 7 and 9 show several reverse fault features. We note a center pop-up block, with the reflectors bent down along the east side of the west fault. The maximum curvature anomaly appears to the right of the coherence anomaly (Figure 7, red arrow). To the west side of the fault, due to fault drag, the curvature anomaly is broader, with the minimum curvature anomaly a some distance from the fault, as well as from maximum curvature and coherence anomalies. Figure 9 shows the same features, with coherence, maximum and minimum curvatures on vertical and time slices. Following the fault to the east, the minimum curvature lineament approaches to the most-positive curvature lineament, indicating folding or drag, creating a pair of maximum/minimum curvatures with coherence in the middle, thereby defining the fault.

Figures 8 and 10 shows normal faults delineating a graben. Again, we see a pair of maximum curvature and coherence next to each other, and a minimum curvature lineament at a distance. This are the same geometries discussed by Sigusmondi and Soldo (2003). Vertically, the curvatures appear to be more continuous, and more easily interpreted than the coherence anomaly which tends to be discontinuous and vertically smeared.

Conclusions

Discontinuity measurements such as coherence are not sensitive to smooth folding, and often result in anomalies that are discontinuous when viewed in the vertical section. Where they are not vertically smeared, they accurately locate the discontinuity. In contrast, curvature lineaments are more continuous on the vertical section and maps folds and flexures. With fault drag and/or antithetic faulting, volumetric curvature will commonly bracket faults with maximum and minimum anomalies but does not give exact fault location. Co-rendering curvature with coherence along with the seismic amplitude data provides a superior interpretation product.

Acknowledgments

We thank PEMEX Exploración y Producción for permission to publish this work and particularly to Juan M. Berlanga, Proyecto Aceite Terciario del Golfo, PEMEX Exploración y Producción, for making our work possible through access to seismic data, support for the data reprocessing and bits of help along the way. Thanks to the sponsors of the OU Attribute-Assisted Seismic Processing and Interpretaion (AASPI) consortium. Thanks to Schlumberger for providing OU with licenses to Petrel used in the interpretation, ant-tracking, and 3D multi-attribute co-rendering.

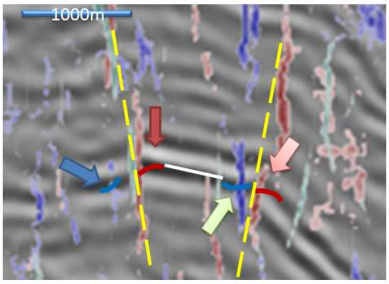


Figure 7: Intepreted faults (yellow) on a pop-up feature bound by coherence (green), maximum curvature (red), minimum curvature (blue) anomalies.

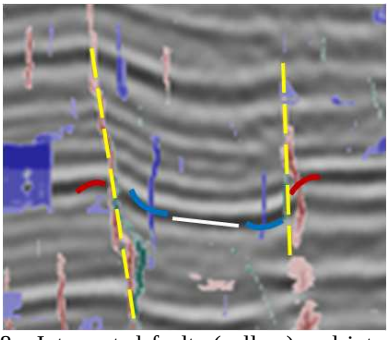


Figure 8: Interpreted faults (yellow) and intervening graben delineated by maximum curvature (red) and minimum curvature and coherence (green).

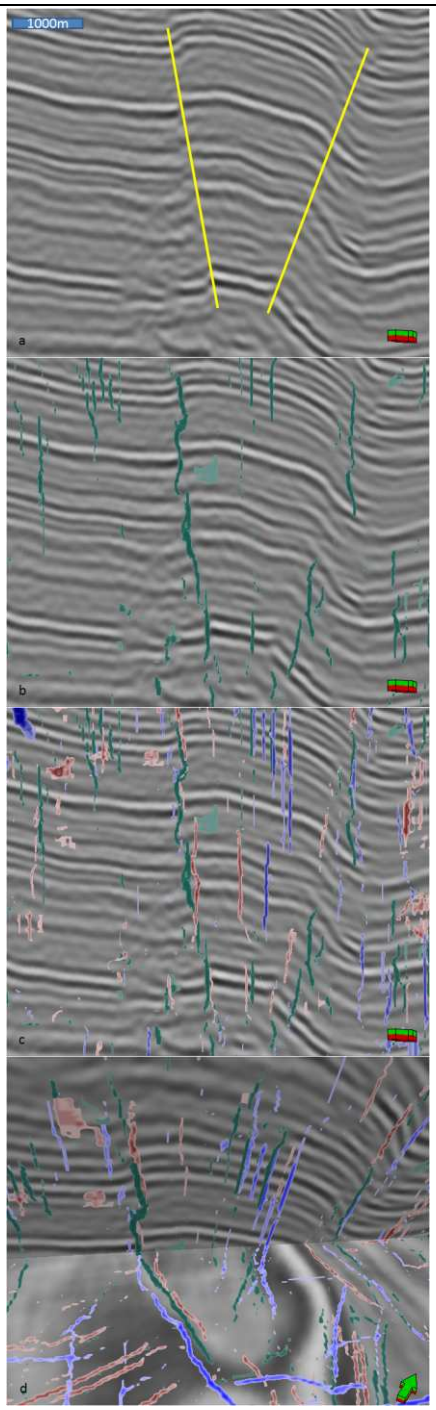


Figure 9: A representative seismic line with (a) interpreted faults, (b) coherence, (c) co-rendered ant-tracked maximum curvature, minimum curvature and coherence with the vertical seismic line, and (d) with an itersecting time slice as well. Intepreted faults (yellow) on a pop-up feature bound by coherence (green), maximum curvature (red), minimum curvature (blue) anomalies.

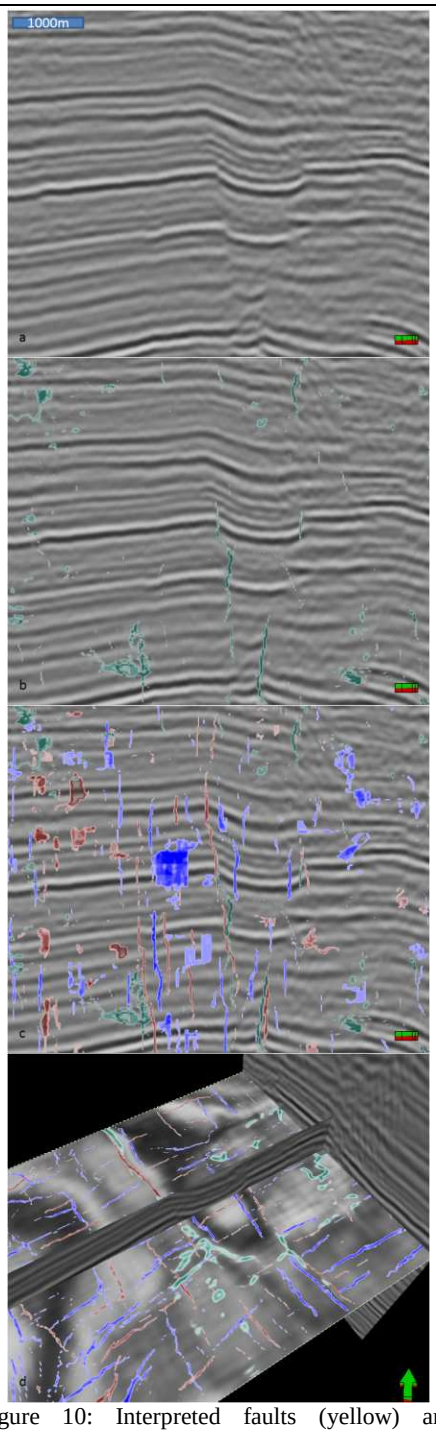


Figure 10: Interpreted faults (yellow) and intervening graben delineated by maximum curvature (red) and minimum curvature and coherence (green): (a) seismic line with interpreted fault (b) coherence, c) ant-tracked maximum curvature, minimum curvature and coherence on seismic line, d) their horizontally extend.

REFERENCES

Chopra, S., and K. J. Marfurt, 2007, Seismic attributes for prospect identification and reservoir characterization: Geophysical Developments No. **11**, SEG.

Ferrill, D. A., and A. P. Morris, 2008, Fault zone deformation controlled by carbonate mechanical stratigraphy, Balcones fault system, Texas: AAPG Bulletin, **92**, 359–380.

Lisle, R. J., 1994, Detection of zones of abnormal strains in structures using Gaussian curvature analysis: AAPG Bulletin, **78**, 1811–1819.

Rich, J., 2008, Expanding the applicability of curvature attributes through clarification of ambiguities in derivation and terminology: 78th Annual International Meeting, SEG, Expanded Abstracts, 884–888

Roberts, A., 2001, Curvature attributes and their application to 3D interpreted horizons: First Break, **19**, 85-99.

Salvador, A., 1991, Origin and development of the Gulf of Mexico basin, *in* Salvador, A., ed., The Gulf of Mexico Basin, The geology of North America: Decade of North American Geology, J, Geological Society of America, 389-444.

Sigismondi, E. M., and C. J. Soldo, 2003, Curvature attributes and seismic interpretation: Case studies from Argentina basins: The Leading Edge, **22**, 1122–1126.

Using 3D rose diagrams for correlation of seismic fracture lineaments with similar lineaments from attributes and well log data

Satinder Chopra+, Kurt J. Marfurt† and Ha T. Mai†*

+Arcis Corporation, Calgary; †The University of Oklahoma, Norman

Summary

Fractures can enhance permeability in reservoirs and hence impact the productivity and recovery efficiency in those areas. Consequently, the detection and characterization of fractures in reservoirs is of great interest which is driving significant improvements in azimuthal anisotropy velocity analysis, azimuthal AVO, image-log breakout interpretation, and seismic attribute analysis. Surface seismic data have long been used for detecting faults and large fractures, but recent developments in seismic attribute analysis have shown promise in identifying groups of closely spaced fractures or interconnected fracture networks. Coherence and curvature are two important seismic attributes that are used for such analysis. Curvature attributes in particular exhibit detailed patterns for fracture networks that can be correlated with image log and production data to ascertain their authenticity. One way to do this correlation is to manually pick the lineaments seen on the curvature displays for a localized area around the boreholes falling on the seismic volume, and then transform these lineaments into rose diagrams. These rose diagrams are then compared with similar rose diagrams obtained from image logs. Favorable comparison of these rose diagrams lends confidence to the interpretation of fractures.

In this work we report the automated generation of rose diagrams from seismic attributes throughout the 3D volume which can then be 'visualizually' correlated to the lineaments seen on different seismic attributes like coherence but also be compared to the rose diagrams available from image logs. Since these rose diagrams are generated at selected regular grid points areally, at every time sample, these are essentially 3D rose diagrams. Appropriate visualization of these 3D rose diagrams with the seismic attribute volumes helps with interpreting the fracture lineaments confidently.

Coherence and curvature attributes for fracture detection

Coherence detection has been used for detection of faults and fractures for over a decade. With the evolution of the eigenstructure algorithms, coherence is able to further improve the lateral resolution and produce relatively sharp and crisp definition of faults and fractures. However, volume curvature attributes have shown promise in helping us with fracture characterization (Al-Dossary and Marfurt, 2006; Chopra and Marfurt, 2007a). By first estimating the volumetric reflector dip and azimuth that represents the best single dip for each sample in the volume, followed by computation of curvature from adjacent measures of dip and azimuth, a full 3D volume of curvature values is produced. There are many curvature measures that can be computed, but the most-positive and most-negative curvature measures are the most useful in mapping subtle flexures and folds associated with fractures in deformed strata. In addition to faults and fractures, stratigraphic features such as levees and bars and diagenetic features such a karst collapse and hydrothermallyaltered dolomites also appear to be well-defined on curvature displays.

Multi-spectral curvature estimates introduced by Bergbauer et al. (2003) and extended to volumetric calculations by Al Dossary and Marfurt (2006) can yield both long and short wavelength curvature images, allowing an interpreter to enhance geologic features having different scales. Long-wavelength curvature often enhances subtle flexures on the scale of 100-200 traces that are difficult to see in conventional seismic, but are often correlated to fracture zones that are below seismic resolution, as well as to collapse features and diagenetic alterations that result in broader bowls.

The quality of these attributes is directly proportional to the quality of the input seismic data. So it is advisable that the data going into attribute computation is cleaned up. We make use of structure-oriented filtering (PC-filtering) for this purpose and obtain results that exhibit more coherent reflections exhibiting sharper lateral discontinuities.

Calibration with well log data

It is always a good idea to calibrate the interpretation on curvature displays with log data if possible. One promising way is to interpret the lineaments in a fractured zone and then transform them into a rose diagram. Such rose diagrams can then be compared with similar rose diagrams that are obtained from image logs to gain confidence in the seismic –to-well calibration. Once a favorable match is obtained, the interpretation of fault/fracture orientations and the thicknesses over which they extend can be used with greater confidence for more quantitative reservoir analysis. Needless to mention such calibrations need to be carried out in localized areas around the wells for accurate comparisons.

Rose diagrams

Fractures are characterized by lineaments that are oriented in different directions. Rather than view individual lineament orientation at a given point, it is possible to combine the various orientations in all

directions into a single rose diagram with angles ranging from 0 to 180 degrees. The length of each petal of the rose is dependent on the frequency of lineaments falling along any angle. Rose diagrams are commonly used for depicting orientations of specific lineaments and are preferred due to their ease of comprehension (Wells, 2000).

Figure 1 shows hand-picked lineaments on the most-positive curvature display in yellow-colored line segments discussed in an earlier paper (Chopra and Marfurt (2007b)). These are then transformed into a rose diagram shown in the inset. Notice, in one single display it is possible to see the orientation of fractures and their density on this surface. Ideally, this rose diagram should be generated at a localized area around a given borehole, instead of over the whole area of the seismic volume.

3D rose diagrams

The curvedness, *c*, of a surface is defined as $c^2 = kmin^2 + kmax^2$ where *kmin* and *kmax* are the minimum and maximum curvature (Roberts, 2001). The curvedness attributes that are directly related to lineaments are the ridge and valley attributes. So a combination of the ridge component of curvedness (Al Dossary and Marfurt, 2006) and axis of the folding plane (strike, corresponding to minimum curvature azimuth ψmin), can visually interpret lineaments.

For a more conventional display and qualification of lineaments, we generate rose diagrams for any gridded-square area defined by an *n-inline* by *m-crossline* analysis window, for each horizontal time slice. Within each analysis window, we bin each pixel into rose petals according to its azimuth ψmin, weighted by its threshold-clipped ridge or valley components of curvedness, then sum and scale them into rose diagrams. The process is repeated for the whole data volume. After that, the rose diagrams are mapped to a rose volume which is equivalent to the data volume, and centered in the analysis window, located at the same location as in input data volume. A robust generation of rose diagrams for the whole lineament volume (corresponding to the seismic volume) is computed, yielding intensity and orientation of lineaments.

Thus 3D rose diagrams are generated from two significant attributes namely the azimuth of minimum curvature and as stated above another attribute that would have a good measure of the shape of the features. This attribute could be the valley attribute or the ridge attribute. Figure 2 shows the generation of the rose diagrams from these attributes as well as the azimuth of the minimum curvature attribute. The displays correlate well with the lineaments seen on coherence aligning with the rose petals; conversely, where there are no lineaments seen on the coherence display, the rose petals do not exhibit significant size.

As the size and lateral spacing of rose generation can be controlled, an optimum spread of the roses needs to be ascertained. To do so, in Figure 3 we show the roses generated at a specific choice of the search radius. In this example, the roses with a radius of 600m appear to have their spread reasonably matching the lineaments on the coherence. However, the correlation of lineaments computed from curvature to those seen on coherence depend strongly on the tectonic deformation. For example, NS en echelon reverse faults may be linked by nearly perpendicular folds. Strike-slip faults may have subparallel folding on one side and almost perpendicular folding on the other (e.g. Rich, 2008).

As shown in the foregoing examples, a significant advantage of the volumetric generation of roses at grid nodes is that it is possible to merge them with a suitable attribute volume. Figure 4 shows the merge of a stratal volume from coherence with the rose volume. It is possible to animate through this volume to the desired level and then examine how the lineaments match the rose petals. A blowup of the rose diagram volume is shown in Figure 5. Such 3D roses help the interpreter notice, within the thickness of the strat-cube shown, if the orientation of the fractures is the same or if it changes. There are at least five roses marked with arrows that indicate changes in orientation of fractures with depth.

Finally, another advantage of such a composite visualization is that in multi-level fracture zones of interest, it is possible to animate to these desired fracture zones. Figure 6 shows stratslices at 50 ms and 100 ms below a marker horizon. Notice how nicely the petal orientations match the low coherence lineaments seen on these displays.

Conclusions

3D rose diagrams can be generated as a volume using either the ridge or the valley shape attribute in combination with the azimuth of minimum curvature attribute. Such a volume can be merged with any other attribute volume that has been generated to study the fracture lineaments and their orientation. We have illustrated this application through examples from a real seismic data volume from Alberta, Canada. Visualization of these volumetric 3D rose diagrams with other discontinuity attributes lends confidence to the interpretation of fracture lineaments. Finally, such 3D rose diagrams can be correlated with similar rose diagrams from image logs, with azimuthal anisotropy velocity data, with tracer data and with production data

Acknowledgements

We wish to thank Arcis Corporation for permission to publish this work.

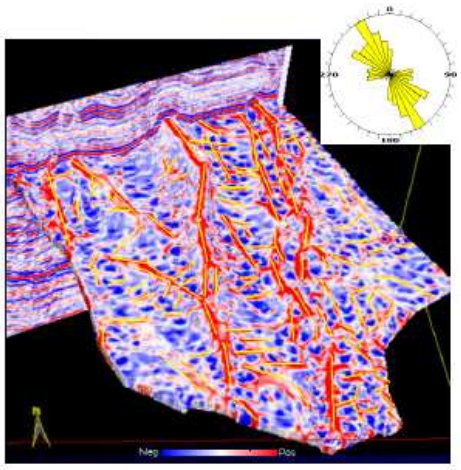


Figure 1. *Lineaments on most-positive curvature horizon slice manually-interpreted as yellow line segments and transformed into a rose diagram shown in the inset.(After Chopra and Marfurt, 2007b).*

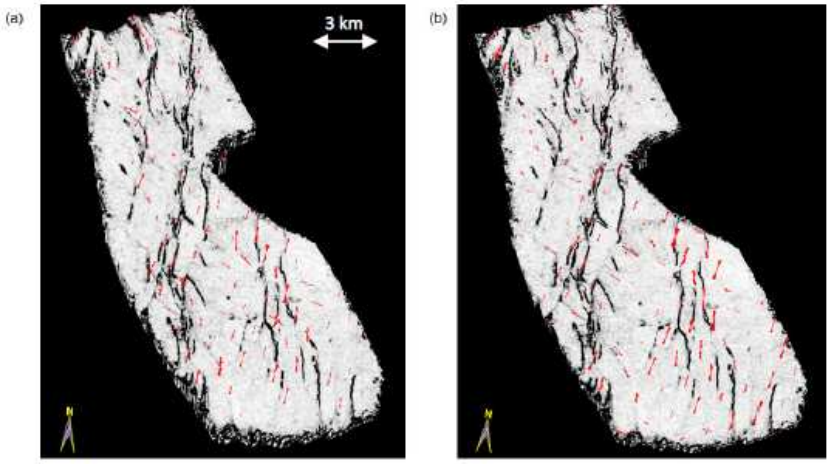


Figure 2. *Strat-slice from coherence volume displayed at a marker horizon and merged with 3D rose diagrams (in red) generated with a search radius of 600 m. In (a) the rose diagrams were generated with the ridge attribute and in (b) the roses were generated with the valley attribute. Notice that there are slight differences in their amplitudes but the orientations seem to be close.*

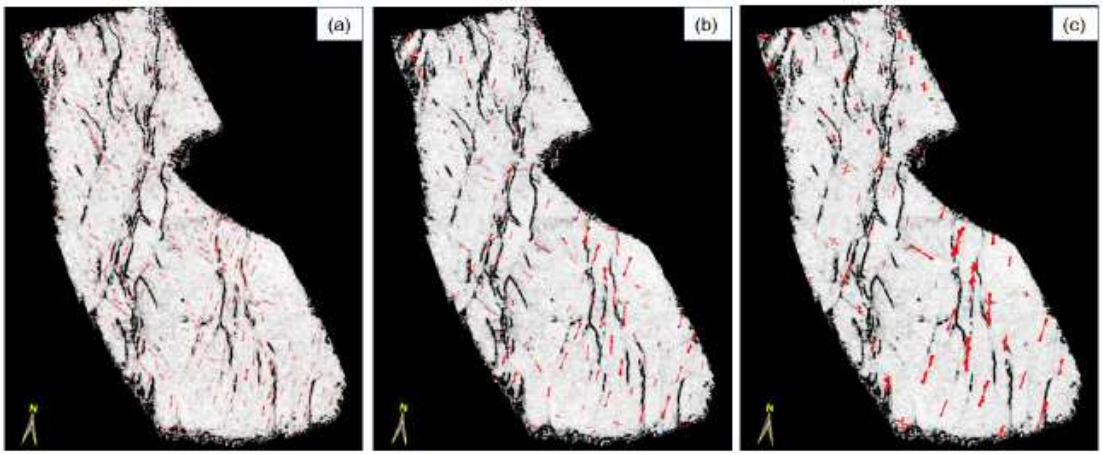


Figure 3. *Strat-slice from coherence volume displayed at a marker horizon and merged with 3D rose diagrams (in red) generated with a search radius of (a) 300m, (b) 600 m, and (c) 100m. In all cases the valley attribute was used besides the azimuth of minimum curvature. Notice that this choice will depend to a large extent on the features on the horizon or time slices being viewed.*

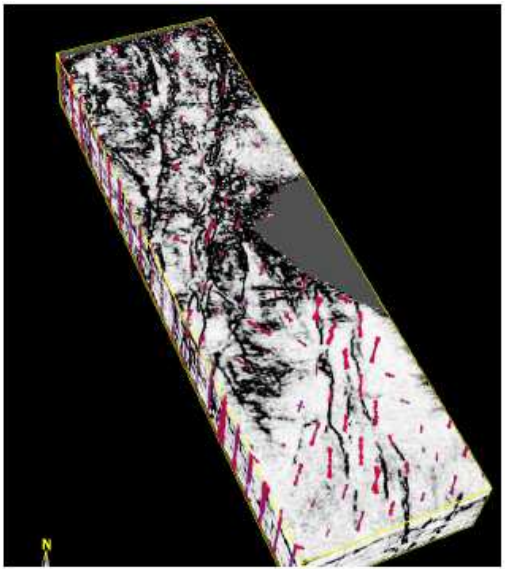


Figure 4. *3D rose diagrams merged with a truncated coherence volume. This composite volume can now be animated to view the alignment and orientation of the features seen on the coherence with roses generated from different attributes and eventually with similar roses from image logs.*

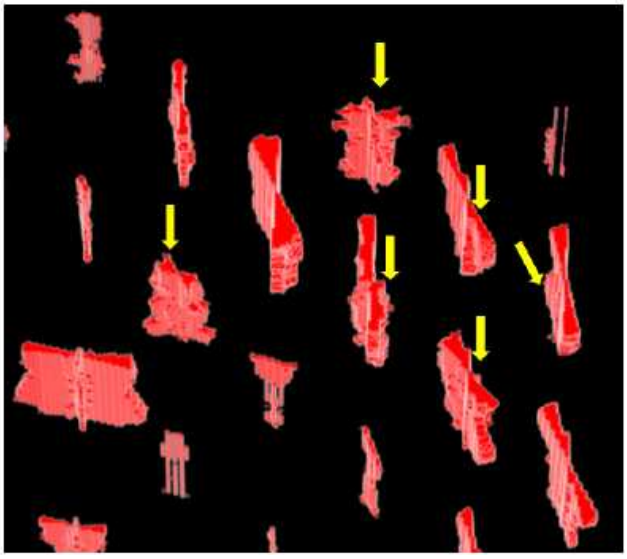


Figure 5. *A blow up of the 3D Rose diagrams at individual points in the 3D volume. Notice the alignment of the petals is not the same within the thickness of the strat-cube, and the changes in orientation of fractures with time are indicated with yellow arrows.*

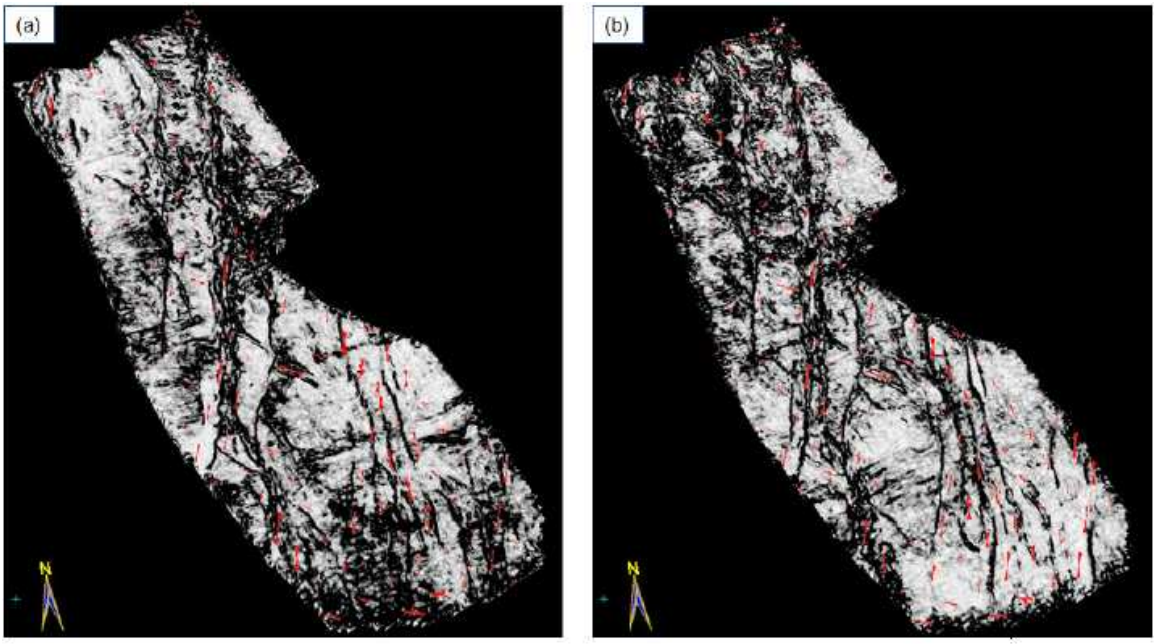


Figure 6. *Strat-cube from a merged volume comprising the 3D rose diagrams as well as the coherence attribute, shown in (a) at 50 ms, and (b) 100 ms below a marker horizon. This composite volume can now be animated to view the alignment and orientation of the features seen on the coherence with roses shown and eventually with similar roses from image logs.*

REFERENCES

Al-Dossary, S., and K. J. Marfurt, 2006, 3D volumetric multispectral estimates of reflector curvature and rotation: Geophysics, **71**, no. 5, P41–P51.

Bergbauer, S., T. Mukerji, and P. Hennings, 2003, Improving curvature analyses of deformed horizons using scale-dependent filtering techniques: AAPG Bulletin, **87**, 1255–1272.

Chopra, S., and K. J. Marfurt, 2007a, Seismic attributes for prospect identification and reservoir characterization: SEG.

Chopra, S., and K. J. Marfurt, 2007b, Volumetric curvature attributes adding value to 3D seismic data interpretation: The Leading Edge, **26**, 856–867.

Rich, J., 2008, Expanding the applicability of curvature attributes through clarification of ambiguities in derivation and terminology: 78th Annual International Meeting, SEG, Expanded Abstracts, 884–887.

Roberts, A., 2001, Curvature attributes and their application to 3-D interpreted horizons: First Break, **19**, 85–99.

Wells, N. A., 2000, Are there better alternatives to standard rose diagrams?: Journal of Sedimentary Research, **70**, 37–46.

Multi-attribute display and rose diagrams for interpretation of seismic fracture lineaments, example from the Cuu Long Basin, Vietnam

Ha T. Mai [(1)], Kurt J. Marfurt [(1)], and Mai Thanh Tan [(2)*]

[(1)] The University of Oklahoma, USA (mtha@ou.edu), [(2)] Hanoi University of Mining and Geology, Vietnam

ABSTRACT

Faults and fractures play a key role in forming effective porosity for hydrocarbon traps in the granite basement of the Cuu Long Basin, Vietnam. Mapping the location, intensity, and orientation of these faults and fractures can help delineate sweet spots and aid in the positioning of horizontal wells. We use volumetric curvature attributes including maximum and minimum curvature, ridge and valley shape components, and the azimuth of minimum curvature to provide not only good fault images but also a quantitative estimate of fractures as a function of strike.

In this work, we co-render multiple attributes in a single composite volume, to visually cluster attributes that delineate different components of the fracture system. For more convenient display of these lineaments, we report a new method to automatically generate volumetric rose diagrams on user-defined n-inline by m-crossline analysis windows spanning the entire seismic volume. A 3D depth-migrated seismic volume acquired over the Cuu Long Basin in Vietnam, was used to present these analysis techniques, and show lineaments corresponding to the granite basement's faults and fractures.

KEYWORDS: Seismic, interpretation, attributes, curvatures, rose diagrams.

INTRODUCTION

The granite basement of Vietnam is composed of Late-Triassic Cretaceous intrusive batholiths. Due to tectonic rifting, the basement is strongly faulted and fractured, with large open fractures coupled with secondary micro-fracturing. Together, the primary and secondary fractures form "damaged zones", which create effective fracture porosity, thereby enhancing the permeability in the hydrocarbon reservoir. In this work, we evaluate the effectiveness of curvature-related lineaments in defining major trends of faults and fractures, by co-rendering of multiple attributes in a composite display, and by automatic generation of 3D rose diagrams from shape component attributes. The 3D rose diagrams and seismic attribute volumes are validated using the tectonic deformation model to help us confidently interpret fracture lineaments.

METHODOLOGY

Curvature of a surface is defined by two orthogonal circles tangent to the surface. The circle with the shortest radius defines the maximum curvature (k_{max}) while the circle perpendicular to it defines the minimum curvature (k_{min}) (Figure 1). The intersection of the plane containing the circle defining minimum curvature with the horizontal plane defines a strike, which is commonly referred to as the azimuth of minimum curvature, ψ_{min}

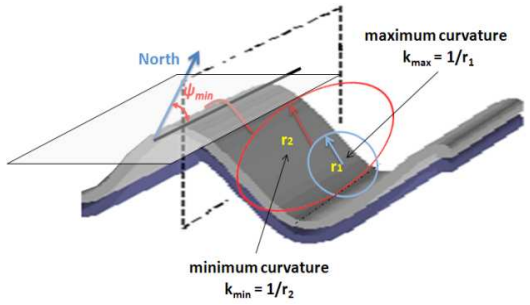


Figure *1*. An illustrated definition of 3D curvature. Maximum curvature has shortest radius and minimum curvature has largest radius. Minumum curvature azimuth is the direction of minumum curvature. (After Lisle, 1994)

The curvedness, c, is defined as

$$c^2 = k_{min}^2 + k_{max}^2 \quad (1)$$

where k_{min} and k_{max} are the minimum and maximum curvature (Roberts, 2001).

Roberts (2001) also shows the usage of the shape index and defines domes, bowls, saddles, valleys, or ridges (Figure 2). The long axes of these shapes correspond to ψ_{min}. By modulating the shape index with the curvedness, c, Al-Dossary and Marfurt (2006) show how we can generate different shape components. For a plane, the curvatures would be zeros. For

elongated anticlinal features, $_{kpos}$ is greater than zero, and k_{neg} is equal to zero, and we define this component of curvedness for this case as ridge component, c_r. Similarly, valley component of curvedness is defined where k_{pos} is equal to zero, and k_{neg} is smaller than zero.

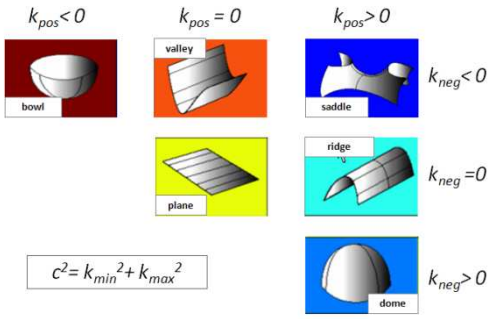


Figure *2.* Geometry of of some folded surfaces. By definition, $k_{neg} \leq k_{pos}$. If $k_{pos} = 0$ and $k_{neg} < 0$, we have a valley shape, and if $k_{pos} > 0$ and $k_{neg} = 0$, we have a ridge shape. (After Bergbauer et al, 2003)

Combining multiple attributes in a single image allows us to visually 'cluster' mathematically different attributes that are sensitive to the same underlying geology, which in our case are faults/fracture lineaments. Since the ridge or the valley component of curvatures might be related to the up-thrown size or down-thrown side of faults, and minimum curvature azimuth in this case is the extending direction of faults, we are going to combine these attributes, and represent the results with two methods, as a 2D color display (Figure 3a), and a rose diagram (Figure 3b). We have developed a module to do this task.

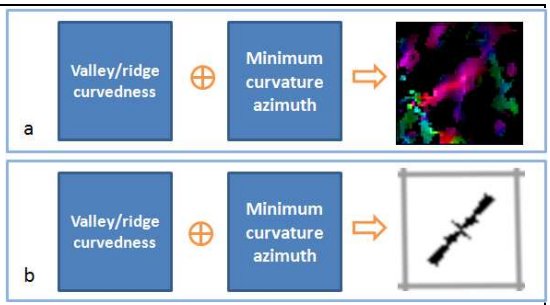


Figure *3.* Combination of the azimuth of minimum-curvature, ψ_{min}, and the ridge component of curvedness to create multi-attribute display and rose diagrams.

In Figure 4, we show a composite image of the ridge component of curvedness, c_r, and minimum curvature azimuth, ψ_{min}. The lightness represents the lineament component of curvedness, which in this case is ridge, and color represents the azimuth of minimum curvature.

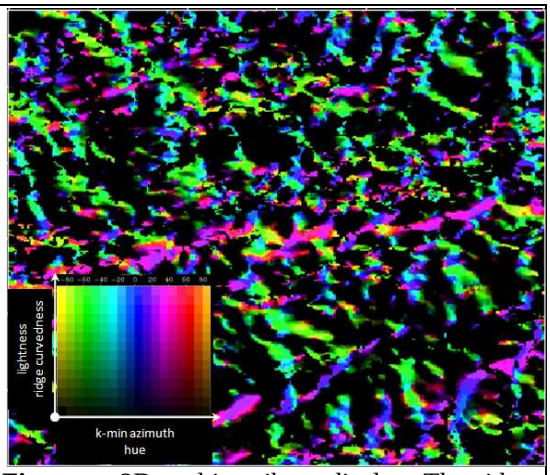


Figure *4.* 2D multi-attribute display. The ridge component of curvedness is plotted against lightness and modulates the azimuth of minimum curvatures, ψ_{min}, plotted against hue.

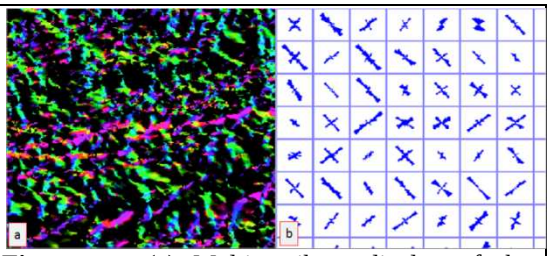


Figure *5.* (a) Multi-attribute display of the azimuth of minimum-curvature, ψ_{min}, modulated by the ridge component of curvedness and (b) the corresponding rose diagrams.

For a more conventional display of these lineaments, we generate rose diagrams for any defined *n-inline* by *m-crossline* analysis window. Within each analysis window, we threshold the ridge (or valley) components of curvedness, c_r (or c_v), bin each voxel according to its azimuth, ψ_{min}, and sum the threshold-clipped values of the ridge or valley components, thereby generating volumetric rose diagrams over a suite of windows spanning the entire seismic volume. A time slice of a representative rose diagram volume is displayed in Figure 5.

CUU LONG BASIN

In the study area, the basement is composed of Pre-Cenozoic magmatic rocks. Due to special characteristics of the area, with multi-phase deformation, the structure of granite

basement was rifted, highly deformed, faulted and fractured. The fractured system provides favorable conditions for hydrocarbons from a laterally deeper Oligocene-Miocene formation to migrate to and accumulate in the basement high.

The most important tectonic deformation occurred during late Oligocene – early Miocene, creating normal faults trending NE-SW and open fractures. A younger major event was during the Miocene, creating strike-slip fault trends in E-W and NW-SE direction. Figure 6a is a depth slice through the seismic amplitude volume; the boundary of the top basement is in white dashed lines, while faults appear as black and yellow dashed lines.

INTERPRETATION

Figure 6b shows a multi-attribute display combining the ridge component of curvedness and the azimuth of minimum curvature. The colors represent lineament's azimuth, with blue showing features in the N-S direction, pink or red showing lineaments features in the NE-SW direction, and green showing lineaments in the NW-SE direction. The lightness is proportional to the intensity of deformation. In this composite display, we see two trends of lineament in the NE-SW and NW-SE directions, which agrees with the geological faulting orientation of the area. The blended rose diagram (Figure 6c) provides a more conventional, more easily quantified display of the lineaments showing the lineament orientation and frequency of occurrence within each analysis window. The NE-SW faults was present along the top of basement, while the younger faults in NW-SE direction are more concentrated in the center section, indicated by yellow arrows in Figure 6c.

The rose diagrams are generated in each analysis window for the whole 3D volume, and exported as a new 3D attribute volume; thereby provide a means of importing them into commercial visualization software. We are thus able to co-render the rose diagrams with suitable attribute volumes, and animate through these volumes to the desired level to better understand the lineaments. Figure 7 shows such an image, with the 3D rose diagrams co-rendered with a seismic amplitude sub-volume (Figure 7a) or with a depth/structure map of top basement (Figure 7b).

The length of the rose's petals represents the intensity of lineaments within the analysis window. Notice that, in some zones above the top of basement, the rose petal length does not vary within a thickness (figure 7b, while arrow), which indicates a consistency in lineament orientation. When the orientation of fractures is consistent over a thickness, it implies a consistent mechanism of fracture over a long period of time. The intensity of lineament varies more, when the analysis window is near the top of basement (figure 7b, blue arrows). This indicates a complication in fracture lineaments of the area. The yellow arrow shows a strong NW-SE lineament, compares with a NE-SW trend that could indicate a big fault cutting across the top of basement.

These results agree with previous studies of the area. However, in order to calibrate the results, it is necessary to compare the interpretation with log data, if possible. When we obtain a good match between seismic-generated rose diagrams and image logs, interpretation of faults/fractures orientation and their vertical extension can be made with higher confidence, for more quantitative reservoir analysis.

CONCLUSIONS

Volumetric curvature as displayed in multi-attribute composite and rose diagrams can be used to illuminate and enhance the signature of fault/fracture lineaments. 3D rose diagrams can be generated and merged with any other attribute volume to study fracture lineaments and their orientations. Calibration with well log is necessary to validate the results. We have implemented this new developed application though a real seismic data volume from the Cuu Long basin, Vietnam.

ACKNOWLEDGEMENTS

The authors would like to acknowledge PetroVietnam for providing the data for this research. Thanks to the sponsors of the OU's Attribute Assisted Seismic Processing and Interpretation (AASPI) consortium. Thanks to Schlumberger for providing University of Oklahoma with licenses for Petrel used in the interpretation and display.

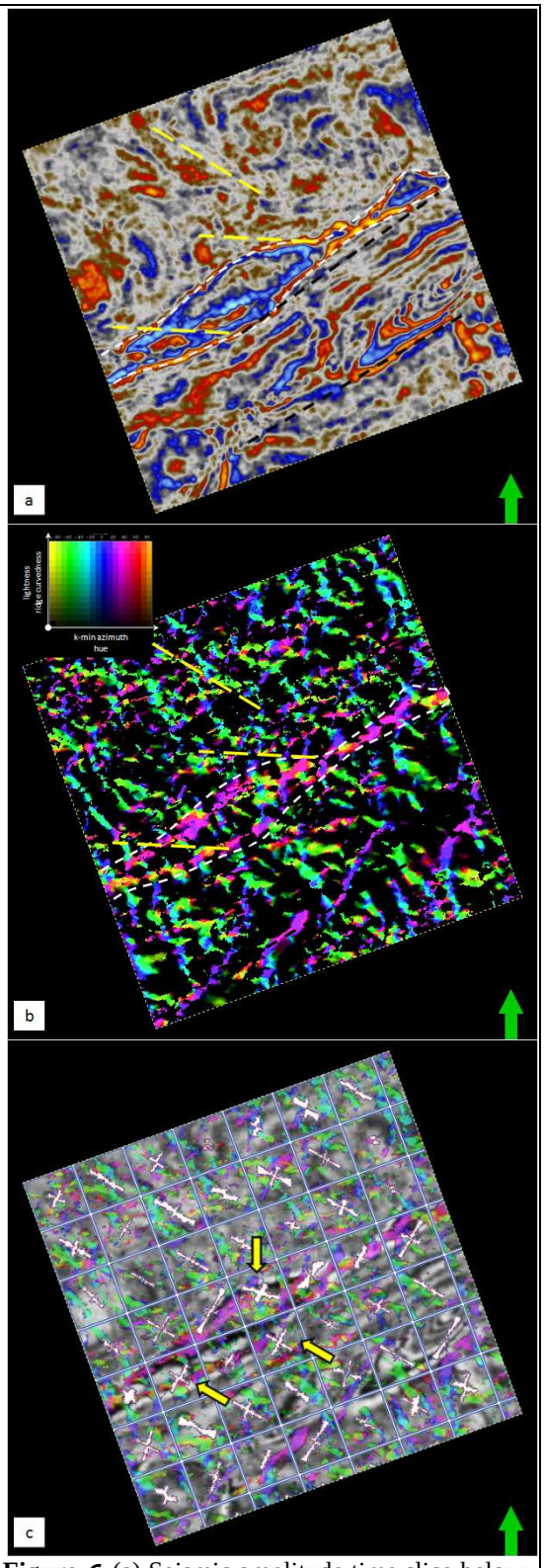


Figure *6.* (a) Seismic amplitude time slice below top of granite basement, (b) Multi-attribute display of ψ_{min} modulated by the ridge curvedness, (c) the blended images with rose diagrams (white).

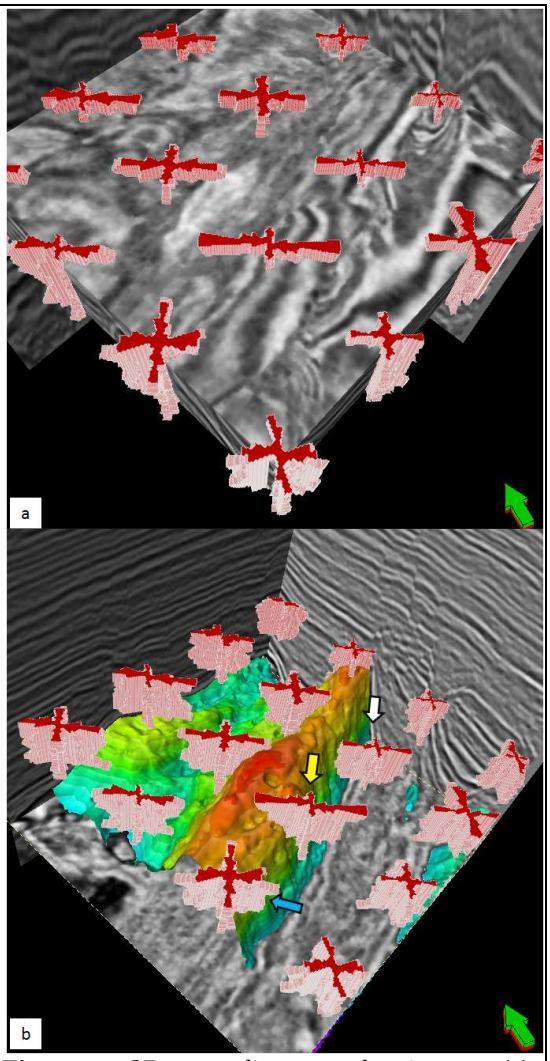


Figure *7.* 3D rose diagrams showing on (a) truncated seismic volume, (b) depth structure map of top basement.

REFERENCES

Al-Dossary, S. and K. J. Marfurt, 2006, *3-D volumetric multispectral estimates of reflector curvature and rotation*: Geophysics, **71**, 41-51.

Bergbauer, S., T. Mukerji, and P. Hennings, 2003, *Improving curvature analyses of deformed horizons using scale-dependent filtering techniques*: AAPG Bulletin, **87**, 1255-1272.

Lisle, R. J., 1994, *Detection of zones of abnormal strains in structures using Gaussian curvature analysis*: AAPG Bulletin, **78**, 1811-1819.

Roberts, A., 2001, *Curvature attributes and their application to 3D interpreted horizons.* First Break, **19**, 85-99.

Using automatically generated 3D rose diagrams for correlation of seismic fracture lineaments with similar lineaments from attributes and well log data

Satinder Chopra,[1*] Kurt J. Marfurt[2] and Ha T. Mai[2]

[1] *Arcis Corporation, 2600, 111-5th Avenue SW, Calgary, Alberta, Canada T2P 3Y6.*
[2] *ConocoPhillips School of Geology and Geophysics, University of Oklahoma, 100 East Boyd Street, Norman, OK 73019, USA.*
[*] *Corresponding author, E-mail: schopra@arcis.com*

Abstract

Detection and characterization of fractures in reservoirs is of great importance for maximizing hydrocarbon productivity and recovery efficiency. Coherence and curvature are two seismic attributes that have shown promise in identifying groups of closely spaced fractures or interconnected fracture networks. Curvature attributes, in particular, exhibit detailed patterns from fracture networks. We report the automated generation of rose diagrams from seismic attributes throughout the 3D volume which can be visually correlated to the lineaments seen on different seismic attributes like coherence and quantitatively correlated to the rose diagrams available from image logs. Since these rose diagrams are generated at regular grid points on each time slice, they are essentially 3D rose diagrams. Visualization of these volumetric 3D rose diagrams with other discontinuity attributes lends confidence to the interpretation of fracture lineaments.

Introduction

Fractures can enhance permeability in reservoirs and hence impact hydrocarbon productivity and recovery efficiency. Consequently, the need to detect and characterize fractures in reservoirs is of great interest and is driving significant improvements in azimuthal anisotropy velocity analysis, azimuthal amplitude-versus-offset (AVO) analysis, image-log breakout interpretation, and seismic attribute analysis.

Surface seismic data have long been used for detecting faults and large fractures, but recent developments in seismic attribute analysis have shown promise in identifying groups of closely spaced fractures or interconnected fracture networks. Coherence and curvature are two important seismic attributes that are used for such analysis. Curvature attributes in particular exhibit detailed patterns for fracture networks that can be correlated with image logs and production data to ascertain their authenticity. One way to do this correlation is to manually pick the lineaments seen on the curvature displays for a localized area around the boreholes falling on the seismic volume, and then transform these lineaments into rose diagrams. These rose diagrams are then compared with similar rose diagrams obtained from image logs. Favourable comparison of these rose diagrams lends confidence to the interpretation of fractures.

In this article we report the automated generation of rose diagrams from seismic attributes throughout the 3D volume. Not only can these rose diagrams be 'visually' correlated to the lineaments seen on different seismic attributes like coherence, but they can also be quantitatively correlated to the rose diagrams available from image logs. Since these rose diagrams are generated at a selected regular grid of points in the horizontal plane, at every time sample, these are essentially 3D rose diagrams. Appropriate visualization of these 3D rose diagrams with the seismic attribute volumes, coupled with an appropriate tectonic deformation model, facilitates confident interpretation of the fracture lineaments.

Coherence and curvature attributes for fracture detection

Coherence has been used for detection of faults and fractures for over a decade. With the evolution of the eigen-structure algorithms, coherence is able to further improve the lateral resolution and produce relatively sharp and crisp definition of faults and fractures. However, volume curvature attributes have shown promise in helping us with fracture characterization (Al-Dossary and Marfurt, 2006; Chopra and Marfurt, 2007a). By first estimating the volumetric reflector dip and azimuth that represents the best single dip for each sample in the volume, followed by computation of curvature from adjacent measures of dip and azimuth, a full 3D volume of curvature values is produced. There are many curvature measures that can be computed, but the most-positive and most-negative curvature measures are the most useful in mapping subtle flexures and folds associated with fractures in deformed strata. In addition to faults and fractures, stratigraphic features, such as levees and bars, and

diagenetic features such as karst collapse and hydrothermally-altered dolomites, also appear to be well defined on curvature displays.

Multi-spectral curvature estimates introduced by Bergbauer et al. (2003) and extended to volumetric calculations by Al-Dossary and Marfurt (2006) can yield both long- and short-wavelength curvature images, allowing an interpreter to enhance geological features having different scales. Long-wavelength curvature often enhances subtle flexures on the scale of 100−200 traces that are difficult to see in conventional seismic data, but are commonly associated with fracture zones that are below seismic resolution or to collapse features and diagenetic alterations that result in broader bowls. The quality of these attributes is directly proportional to the quality of the input seismic data, so it is advisable that the data going into attribute computation is cleaned up. We make use of structure-oriented filtering (PC-filtering) for this purpose and obtain results that contain more coherent reflections exhibiting sharper lateral discontinuities (Chopra and Marfurt, 2008).

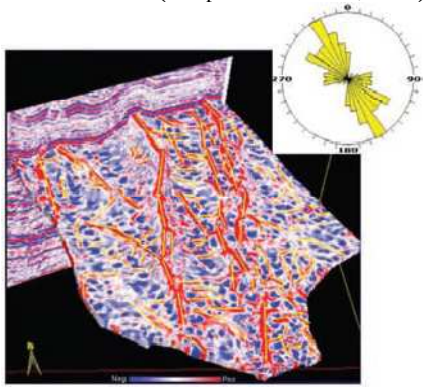


Figure 1. *Horizon slice for the most-positive curvature attribute. Lineaments interpreted as faults are marked as yellow line segments and have been transformed into the rose diagram shown in the inset. (After Chopra and Marfurt, 2007b).*

Calibration with well log data

If possible, it is always a good idea to calibrate the interpretation on curvature displays with log data. One promising way is to interpret the lineaments in a fractured zone and then transform them into a rose diagram. Such rose diagrams can then be compared with similar rose diagrams that are obtained from image logs to gain confidence in the seismic-to-well calibration. Once a favourable match is obtained, the interpretation of fault/fracture orientations and the thicknesses over which they extend can be used with greater confidence for more quantitative reservoir analysis. Needless to mention, such calibrations need to be carried out in localized areas around the wells for accurate comparisons.

Rose diagrams

Fractures are characterized by lineaments that are oriented in different directions. Rather than view individual lineament orientation at a given point, it is possible to combine the various orientations in all directions into a single rose diagram with angles ranging from 0 to 180°. The length of each petal of the rose is dependent on the frequency of lineaments falling along any angle. Rose diagrams are commonly used for depicting orientations of specific lineaments and are preferred due to their ease of comprehension (Wells, 2000).

Figure 1 shows hand-picked lineaments on the most-positive curvature display in yellow-coloured line segments discussed in an earlier paper (Chopra and Marfurt, 2007b). These are then transformed into a rose diagram shown in the inset. Note that in a single display it is possible to see both the orientation of fractures and their density on this surface. Ideally, this rose diagram should be generated at a localized area around a given borehole, instead of over the whole area of the seismic volume.

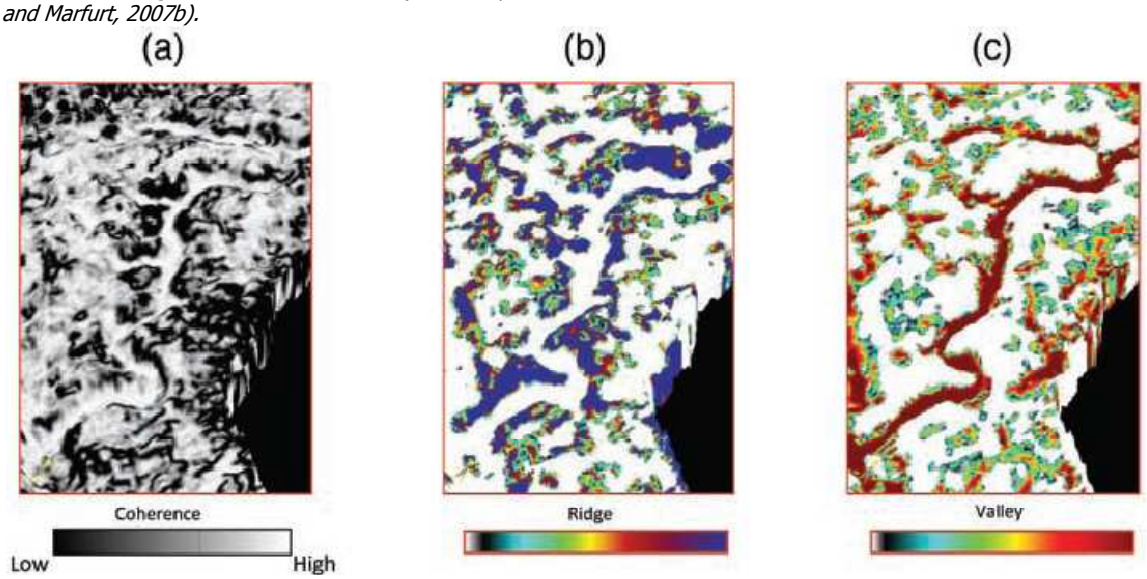


Figure 2. *Horizon slices from (a) coherence, (b) ridge, and (c) valley attributes.*

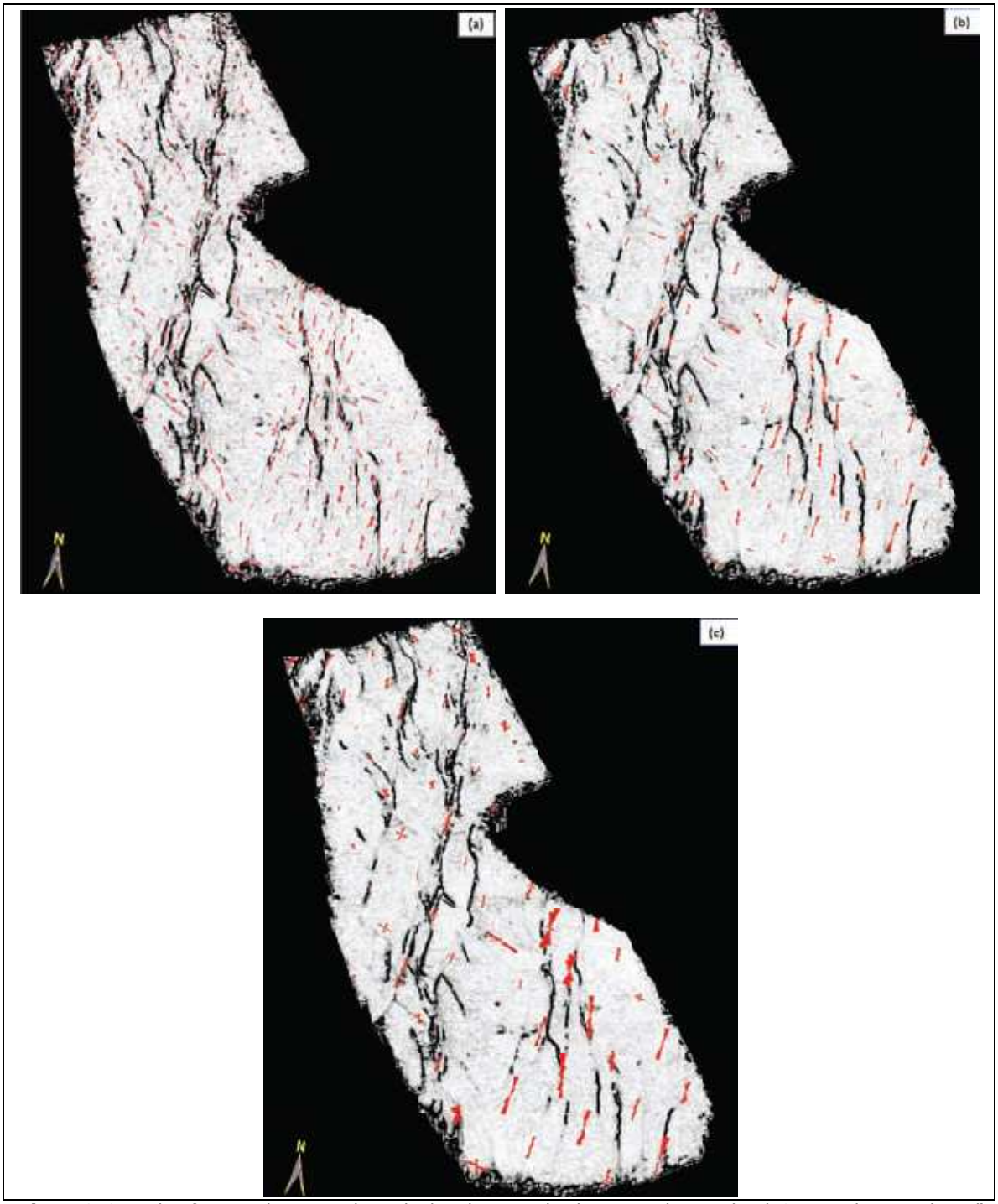


Figure 3. *Strat-slice from a coherence volume displayed at a marker horizon and merged with 3D rose diagrams (in red) generated with a search radius of (a) 300 m, (b) 600 m, and (c) 1000 m. In all cases, the other attribute used was the ridge attribute. Notice that this choice will depend to a large extent on the features on the horizon or time slice being viewed.*

3D rose diagrams

The curvedness, c, of a surface is defined by

$$c^2 = k^2_{min} + k^2_{max} \quad (1)$$

where k_{min} and k_{max} are the minimum and maximum curvature (Roberts, 2001). Roberts (2001) also shows how k_{min} and k_{max} can be used to compute a shape index, s, which defines dome (s = +1), ridge (s = +1/2), saddle (s = 0), valley (s = –1/2), and bowl (s = –1) quadratic surfaces. The curvedness defines the intensity of deformation in generating these shapes, with a planar surface being defined as c = 0. Al-Dossary and Marfurt (2006) showed how the intensity of deformation can be combined with the shape index to generate shape components, with the sum of the components equal to the curvedness. The choice of shape depends on the geological model being used. In Figure 2 we show a comparison of the coherence horizon slice with the valley and the ridge horizon slices. Note that the edges of the channel are accentuated by the ridge attribute and the thalweg of the channel is defined better by the valley attribute. Ridges and valleys (as well as elongated domes and bowls) have a well-defined strike. We will therefore interpret the azimuth of minimum curvature, ψ_{min}, to be a direct measurement of the strike of ridges and valleys.

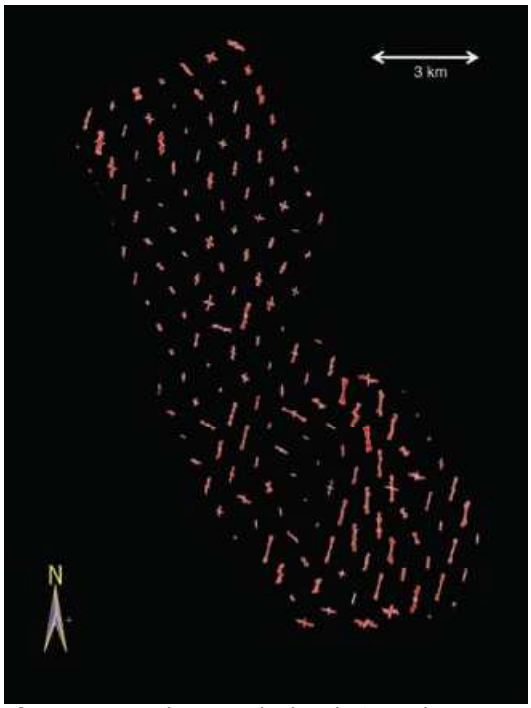


Figure 4. *Rose diagrams displayed 40 ms above a marker horizon.*

For a more conventional display and qualification of lineaments, we generate rose diagrams for any gridded- square area defined by an n-inline by m-crossline analysis window, for each horizontal time slice. Within each analysis window, we bin each pixel into rose petals according to its azimuth, ψ_{min}, weighted by its threshold-clipped ridge or valley components of curvedness, then sum and scale them into rose diagrams. The process is repeated for the whole data volume. After that, the rose diagrams are mapped to a rose volume which is equivalent to the data volume and centred in the analysis window, located at the same location as in the input data volume. A robust generation of rose diagrams for the whole lineament volume (corresponding to the seismic volume) is computed, yielding intensity and orientation of lineaments.

In this manner, we generate 3D rose diagrams from either the ridge or valley component of curvature and the azimuth of minimum curvature. The choice of ridge or valley depends on the geological processes that formed them. Thus, if we wish to generate rose diagrams of a channel-levee system, rose diagrams generated from the valley component of curvature would be a direct measure of the channel axes. Likewise, the valley component of curvature is a direct measure of intensity of karst-enhanced fractures in an otherwise planar carbonate horizon. In structurally deformed areas, the noses of the anticlines are often 'sharper' than the valley lows, such that the ridge component of curvature may provide more useful images (Figure 2). Figure 3 shows the generation of rose diagrams from the ridge component of curvature and the azimuth of the minimum curvature. The displays correlate well with the lineaments seen on coherence aligning with the rose petals; conversely, where there are no lineaments seen on the coherence display, the rose petals do not exhibit significant size. As the size and lateral spacing of rose generation can be controlled, an optimum spread of the roses needs to be ascertained. To do so, in Figure 3 we show the roses generated at a specific choice of the search radius. In this example, the spreads of roses with a radius of 600 m appear to match the lineaments on the coherence reasonably well. However, the correlation between lineaments computed from curvature and those seen on coherence depend strongly on the tectonic deformation. For example, N–S en echelon reverse faults may be linked by nearly perpendicular folds. Strike-slip faults may have subparallel folding on one side and almost perpendicular folding on the other (e.g., Rich, 2008). In Figure 4 we show the 3D rose diagrams 40 ms above a marker horizon, which is a convenient way of correlating these with the rose diagrams.

As shown in the foregoing examples, a significant advantage of the volumetric generation of roses at grid nodes is that it is possible to merge them with a suitable attribute volume. Figure 5 shows the merge of a stratal volume from coherence with the rose volume. It is possible to animate through this volume to the desired level and then examine how the lineaments match the rose petals. A blowup of the rose diagram volume is shown in Figure 6.

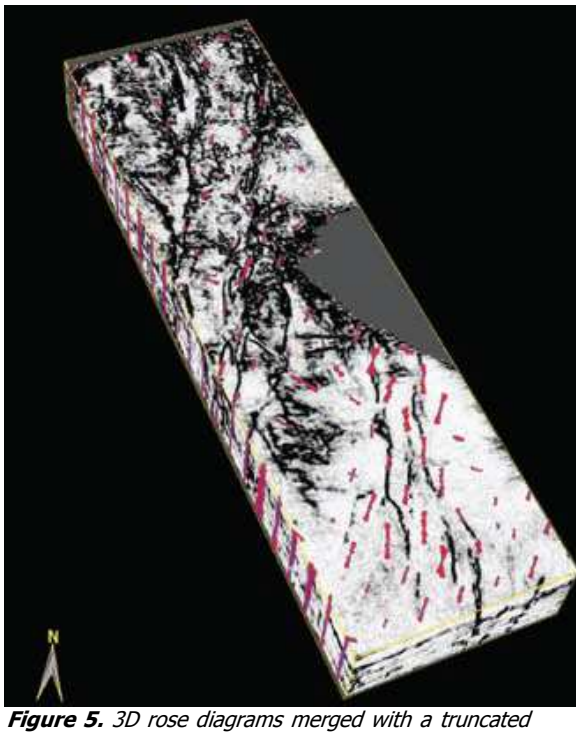


Figure 5. *3D rose diagrams merged with a truncated stratal coherence volume. This composite volume can now be animated to view the alignment and orientation of the features seen on the coherence with roses generated from different attributes and eventually with similar roses from image logs.*

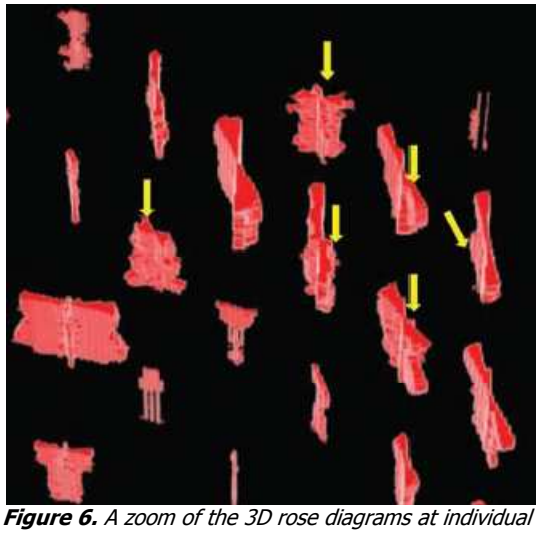


Figure 6. *A zoom of the 3D rose diagrams at individual points in the 3D volume. Notice the alignment of the petals is not the same within the thickness of the strat-cube, and the changes in orientation of fractures with time are indicated with yellow arrows.*

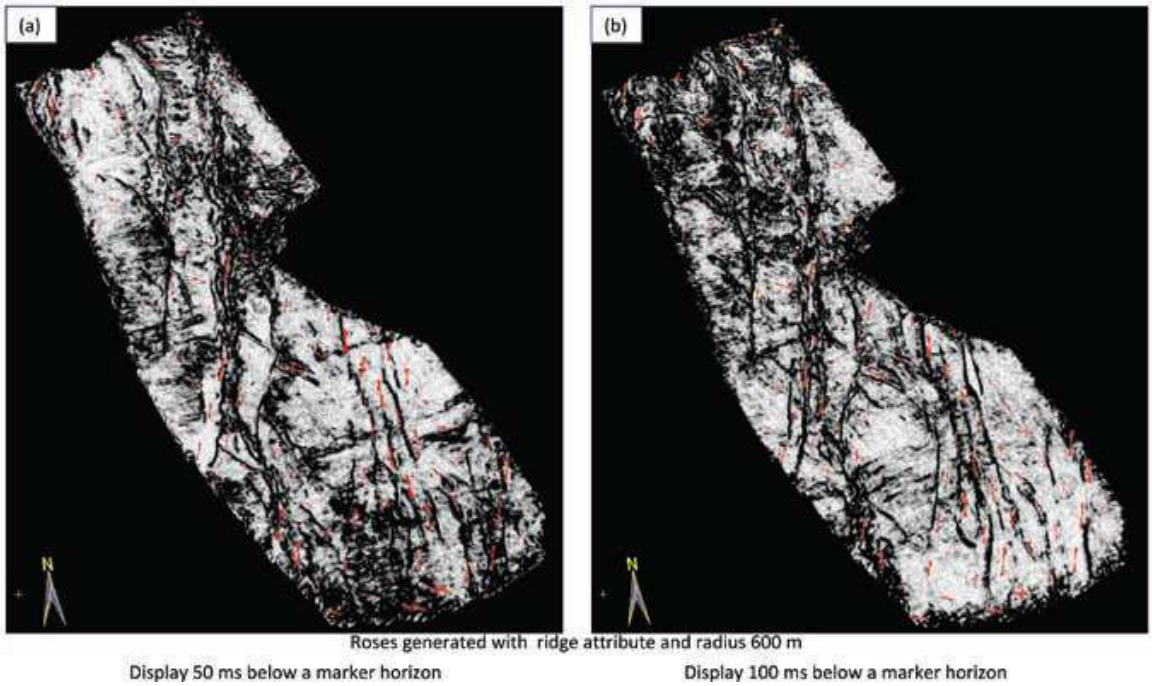


Figure 7. *Strat-cube from a merged volume comprising the 3D rose diagram as well as the coherence attribute, shown in (a) at 50 ms, and in (b) at 100 ms below the marker horizon. This composite volume can now be animated to view the alignment and orientation of the features seen on the coherence with roses generated from different attributes and eventually with similar roses from image logs.*

Such 3D roses help the interpreter notice, within the thickness of the strat-cube shown, if the orientation of the fractures is the same or if it changes. There are at least five roses marked with arrows that indicate changes in orientation of fractures with depth.

Finally, another advantage of such a composite visualization is that in multi-level fracture zones of interest, it is possible to animate to these desired fracture zones. Figure 7 shows strat-slices at 50 ms and 100 ms below a marker horizon. Notice how nicely the petal orientations match the low coherence lineaments seen on these displays.

Conclusions

3D rose diagrams can be generated as a volume using either the ridge or the valley shape attribute in combination with the azimuth of minimum curvature attribute. Such a volume can be merged with any other attribute volume that has been generated to study the fracture lineaments and their orientation. We have illustrated this application through examples from a real seismic data volume from Alberta, Canada. Visualization of these volumetric 3D rose diagrams with other discontinuity attributes lends confidence to the interpretation of fracture lineaments. Finally, such 3D rose diagrams can be correlated with similar rose diagrams from image logs, with azimuthal anisotropy velocity data, with tracer data, and with production data.

Acknowledgements

We thank Arcis Corp. for permission to publish this work.

References

Al-Dossary, S. and Marfurt, K.J. [2006] Multispectral estimates of reflector curvature and rotation. *Geophysics*, **71**, P41-P51.

Bergbauer, S., Mukerji, T. and Hennings, P. [2003] Improving curvature analyses of deformed horizons using scale-dependent filtering techniques. *AAPG Bulletin*, **87**, 1255-1272.

Chopra, S. and Marfurt, K.J. [2007a] *Seismic Attributes for Prospect Identification and Reservoir Characteriz*ation. Society of Exploration Geophysicists, Tulsa.

Chopra, S. and Marfurt, K.J. [2007b] Volumetric curvature attributes adding value to 3D seismic data interpretation. *The Leading Edge*, **26**, 856-867.

Chopra, S. and Marfurt, K.J. [2008] Gleaning meaningful information from seismic attributes. *First Break*, **26**(9), 43-53.

Rich, J. [2008] Expanding the applicability of curvature attributes through clarification of ambiguities in derivation and terminology. *SEG 78th Annual Meeting*, Expanded Abstracts, 884-887.

Roberts, A. [2001] Curvature attributes and their application to 3D interpreted horizons. *First Break*, **19**(2)**,** 85-100.

Wells, N.A. [2000] Are there better alternatives to standard rose diagrams? *Journal of Sedimentary Research*, **70**, 37-46.

Received 14 May 2009; accepted 31 July 2009.

Chapter 7 Conclusions

Geometric attributes related to structure such as apparent dip, amplitude gradient and curvatures help enhance the signature of geological reflectors, especially the reflectors related to faults and folds. While the apparent dip attribute shows a range of value, along a dipping reflector surface, the amplitude energy gradient shows a higher resolution where the properties of the reflector are changing. Rotating the apparent illumination direction gives the interpreter a visual tool to better delineate structurally complicated features such as faults and fractures.

Volumetric curvature attributes provide further indication of lineaments. With respect to faults, these attributes may not coincide with the exact fault location. They commonly bracket faults. Combining curvature with coherence and seismic amplitude, the interpreter can quickly visualize and quantify structural style on an uninterpreted seismic volume.

Combining two or more attributes and visualizing them in the form of multi-attribute displays or rose diagrams, allows the interpreter to further delineate location of faults or other lineament features, quantify their intensity and orientation (with rose diagrams), or define structural shapes (shape index).

Using a proper suite of attributes, we can generate a superior interpretation product, which can help in drilling or production design decision making.

Appendix

Overview

As part of the effort, I have generated a complete set of interactive Graphic User Interfaces (GUIs), shell scripts, and documentation on how to use the AASPI software for OU students, staff, as well as AASPI sponsors.

The AASPI software runs on a Linux system. It includes three parts (Figure A1):

- AASPI Graphic User Interfaces: provide an easy way to launch jobs, quality control user-defined parameters, and generate simple graphical displays. These GUIs are programmed in C++, using FOX Toolkit graphic libraries. I have written 100% of the GUIs.
- Shell scripts: read parameters from the GUIs, do some simple error checking when possible, and submit a job to AASPI computing applications in the background, typically running in parallel under the Message Passing Interface (MPI). I have modified all of the shell scripts to interface with the GUIs, and written from scratch those that invoke the Fortran90 applications I have written, as well as those that convert input and output to and from the SEGY standard
- AASPI computing applications: The heart of AASPI software that perform the actual seismic attributes computation. These applications are written in FORTRAN90. I have written applications that generate rose diagrams and Euler components of curvature, and significantly modified algorithms for multi-attribute display. I have also written the basic conversion codes that pad and quality control the data conversions from SEGY.



Figure A1: AASPI software workflow

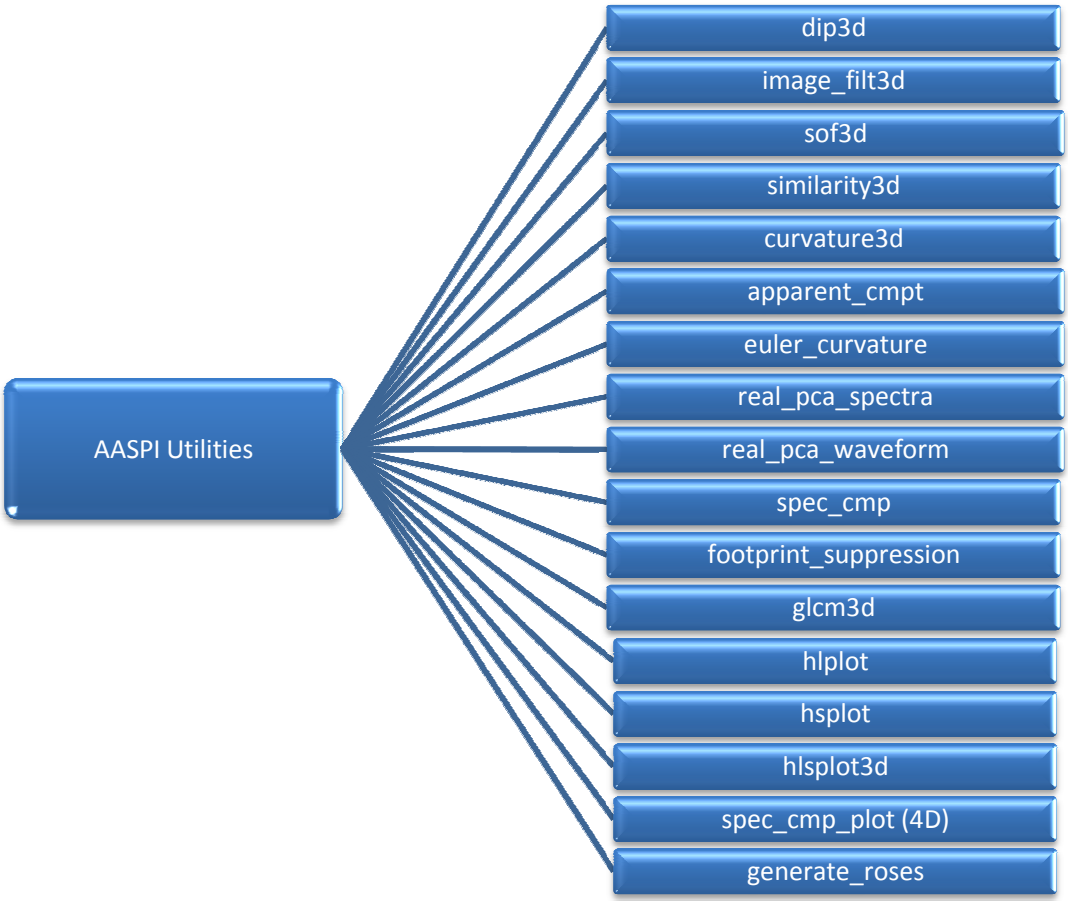


Figure A2: AASPI software components

The interface includes one master GUI (aaspi_util) and 17 seismic attribute computing and plotting GUIs (Figure A2). The attribute computing GUIs are classified into four groups:

- Volumetric Attributes: dip3d, image_filt3d, sof3d, similarity3d, curvature3d, apparent_cmpt, euler_curvature
- Formation Attributes: real_pca_spectra, real_pca_waveform
- Others: generate_roses, spec_cmp, footprint_suppresion, glcm3d.
- Plotting Tools: hlplot, hsplot, hlsplot3d, spec_cmp_plot

Each GUI is connected to one or more seismic attribute computing or displaying application.

Master Graphic User Interface (GUI): aaspi_util

All the seismic attribute applications can be called from the master GUI: aaspi_util (Figure A3), through the drop-down menu (Volumetric Attributes, Formation Attributes, Display Tools, and Others). The I/O and display utilities are: Segy2sep, Sep2Segy (auto), Sep2segy (single), and SEP Viewer.

Segy2sep converts 3D seismic files in SEG-Y standard format (IBM 32bits) into SEP format that we use internally for attribute computation.

Sep2Segy (auto) automatically searches and converts selected sets of attributes from SEP format to SEG-Y format for further processing and interpretation.

Sep2Segy (single) converts one selected seismic file from SEP format into SEG-Y format.

SepViewer does simple seismic data display of SEP format files, for quality control.

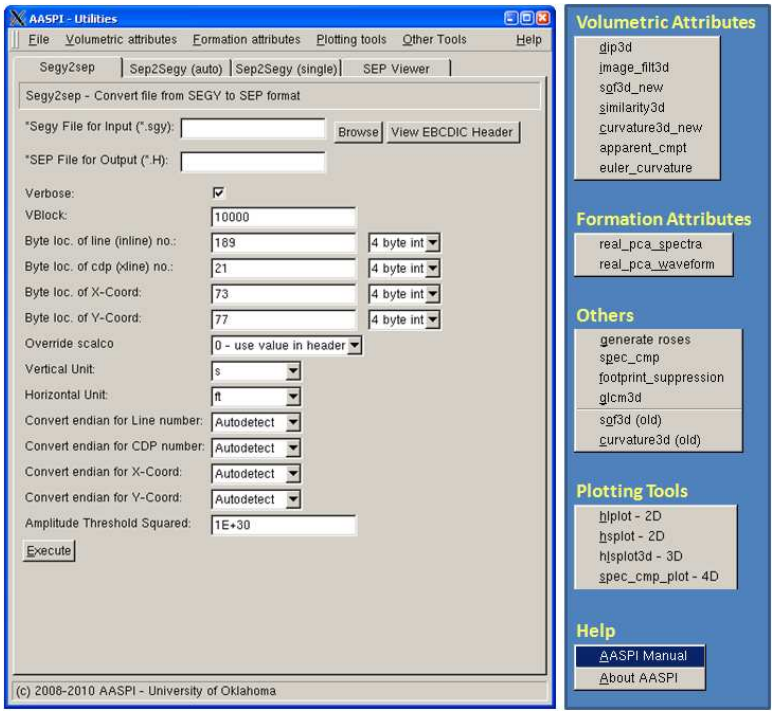


Figure A3: AASPI Utilities

The master GUI also links with an AASPI software manual (Figure A4), which include the detail description of each application and on how to use them.

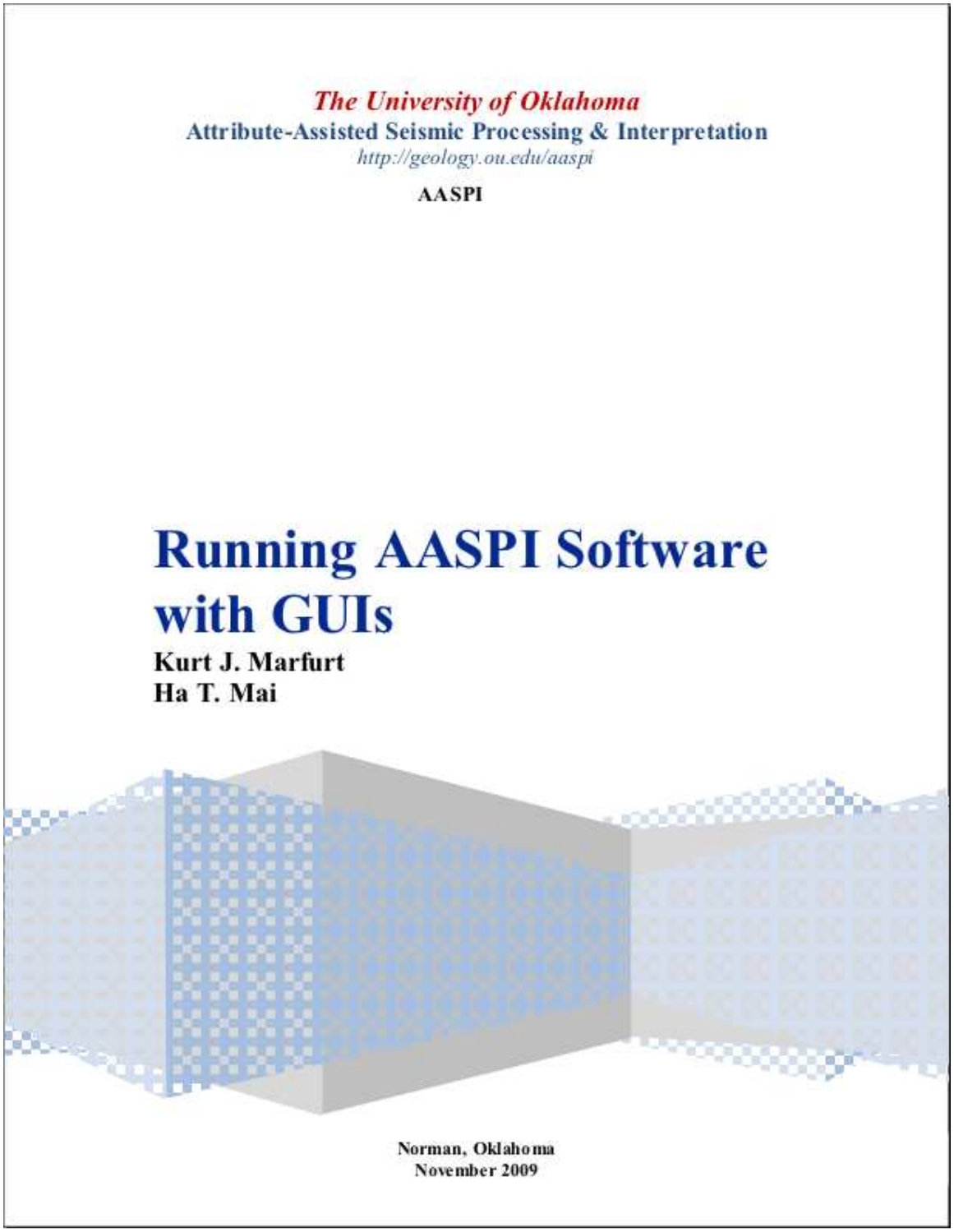


Figure A4: AASPI Manual: Running AASPI Software with GUIs

AASPI seismic attribute GUIs and computing programs

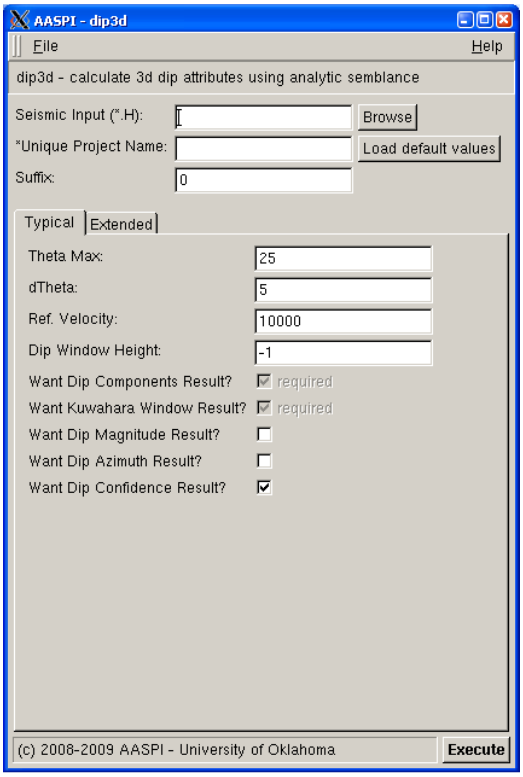
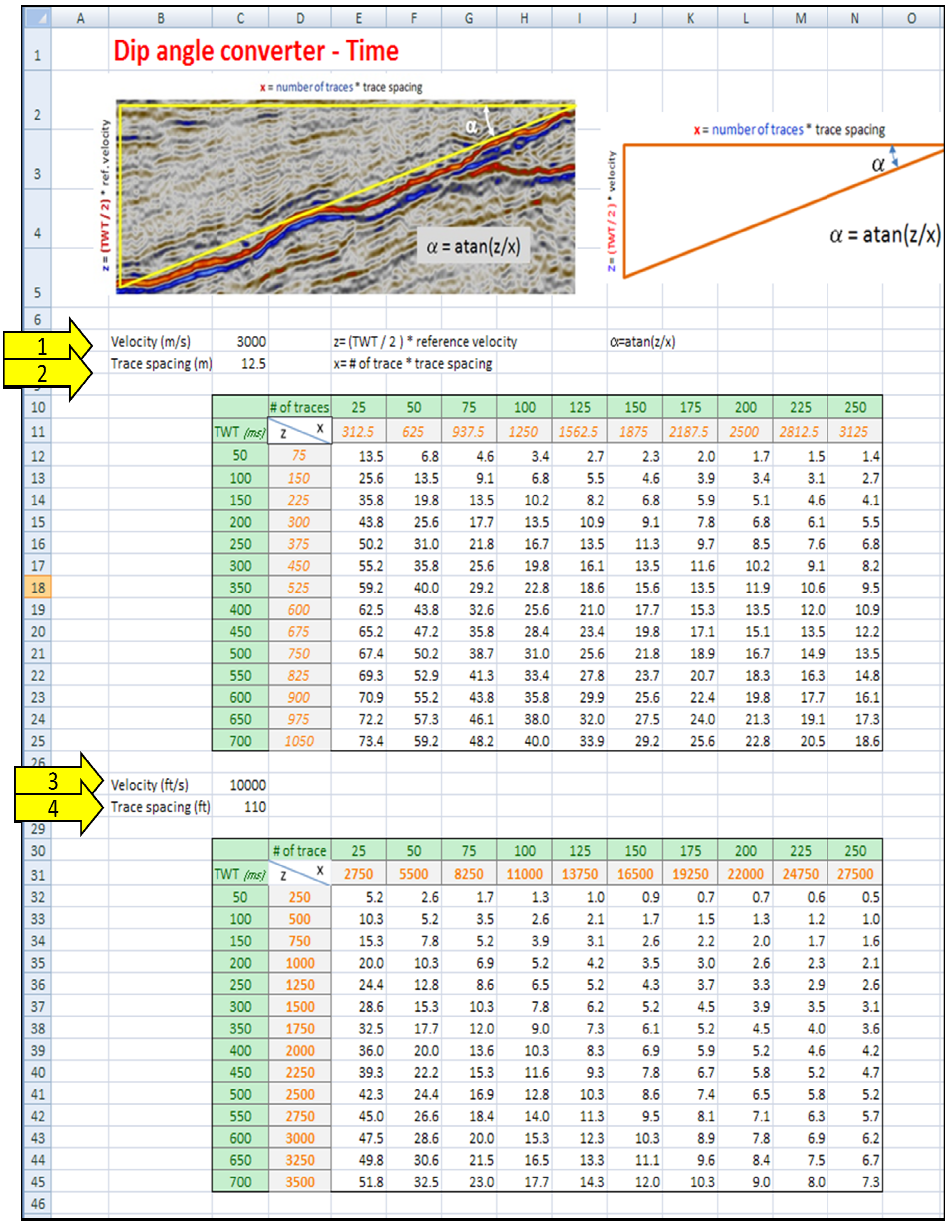


Figure A5: AASPI dip3d

dip3d - compute 3D dip components using analytic semblance in overlapping analysis windows (a Kuwahara implementation).

The program dip3d is supported by an external excel dip angle estimator (Figure A6). This estimator helps converting the degree of dipping events from seismic data units (traces and trace spacing for horizontal axis, and time or depth for vertical axis) into geometry unit (degree) to use as maximum dip search (theta_max) in dip3d program.



	# of traces	25	50	75	100	125	150	175	200	225	250
TWT (ms)	z \ x	312.5	625	937.5	1250	1562.5	1875	2187.5	2500	2812.5	3125
50	75	13.5	6.8	4.6	3.4	2.7	2.3	2.0	1.7	1.5	1.4
100	150	25.6	13.5	9.1	6.8	5.5	4.6	3.9	3.4	3.1	2.7
150	225	35.8	19.8	13.5	10.2	8.2	6.8	5.9	5.1	4.6	4.1
200	300	43.8	25.6	17.7	13.5	10.9	9.1	7.8	6.8	6.1	5.5
250	375	50.2	31.0	21.8	16.7	13.5	11.3	9.7	8.5	7.6	6.8
300	450	55.2	35.8	25.6	19.8	16.1	13.5	11.6	10.2	9.1	8.2
350	525	59.2	40.0	29.2	22.8	18.6	15.6	13.5	11.9	10.6	9.5
400	600	62.5	43.8	32.6	25.6	21.0	17.7	15.3	13.5	12.0	10.9
450	675	65.2	47.2	35.8	28.4	23.4	19.8	17.1	15.1	13.5	12.2
500	750	67.4	50.2	38.7	31.0	25.6	21.8	18.9	16.7	14.9	13.5
550	825	69.3	52.9	41.3	33.4	27.8	23.7	20.7	18.3	16.3	14.8
600	900	70.9	55.2	43.8	35.8	29.9	25.6	22.4	19.8	17.7	16.1
650	975	72.2	57.3	46.1	38.0	32.0	27.5	24.0	21.3	19.1	17.3
700	1050	73.4	59.2	48.2	40.0	33.9	29.2	25.6	22.8	20.5	18.6

	# of trace	25	50	75	100	125	150	175	200	225	250
TWT (ms)	z \ x	2750	5500	8250	11000	13750	16500	19250	22000	24750	27500
50	250	5.2	2.6	1.7	1.3	1.0	0.9	0.7	0.7	0.6	0.5
100	500	10.3	5.2	3.5	2.6	2.1	1.7	1.5	1.3	1.2	1.0
150	750	15.3	7.8	5.2	3.9	3.1	2.6	2.2	2.0	1.7	1.6
200	1000	20.0	10.3	6.9	5.2	4.2	3.5	3.0	2.6	2.3	2.1
250	1250	24.4	12.8	8.6	6.5	5.2	4.3	3.7	3.3	2.9	2.6
300	1500	28.6	15.3	10.3	7.8	6.2	5.2	4.5	3.9	3.5	3.1
350	1750	32.5	17.7	12.0	9.0	7.3	6.1	5.2	4.5	4.0	3.6
400	2000	36.0	20.0	13.6	10.3	8.3	6.9	5.9	5.2	4.6	4.2
450	2250	39.3	22.2	15.3	11.6	9.3	7.8	6.7	5.8	5.2	4.7
500	2500	42.3	24.4	16.9	12.8	10.3	8.6	7.4	6.5	5.8	5.2
550	2750	45.0	26.6	18.4	14.0	11.3	9.5	8.1	7.1	6.3	5.7
600	3000	47.5	28.6	20.0	15.3	12.3	10.3	8.9	7.8	6.9	6.2
650	3250	49.8	30.6	21.5	16.5	13.3	11.1	9.6	8.4	7.5	6.7
700	3500	51.8	32.5	23.0	17.7	14.3	12.0	10.3	9.0	8.0	7.3

Figure A6: AASPI Dip Angle Estimator

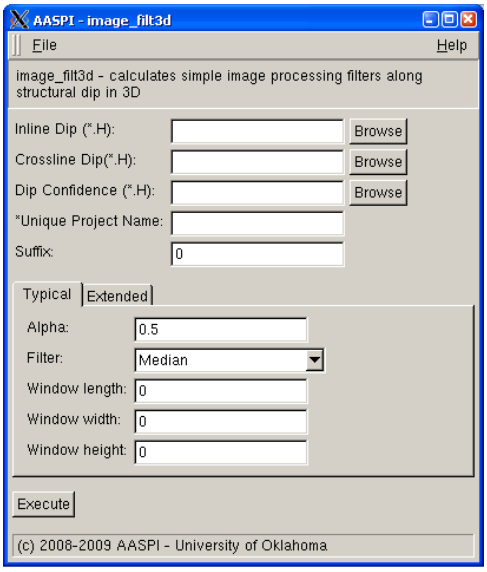


Figure A7: AASPI image_filt3d

image_filt3d - filters inline and crossline components of structural dip along the previous estimate of dip using edge-preserving filters.

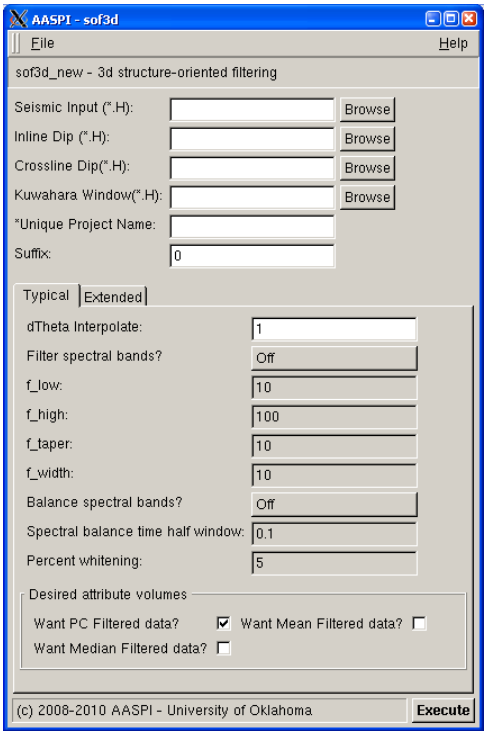


Figure A8: AASPI sof3d

sof3d - structure-oriented filtering of 3D data volumes, rejecting random noise and presser edges.

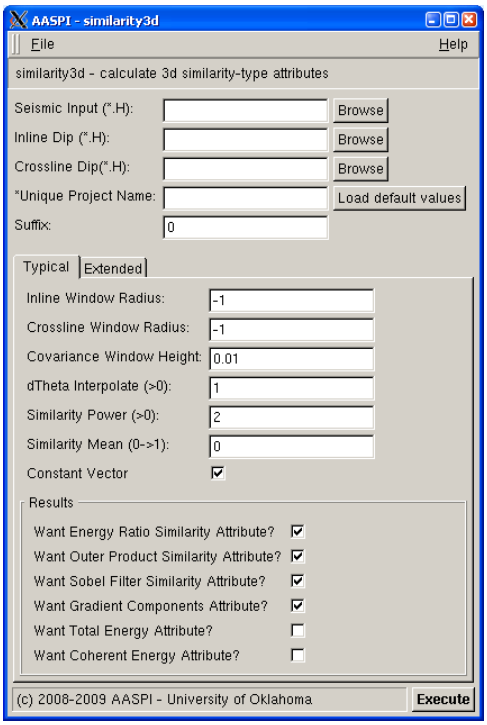


Figure A9: AASPI similarity3d

similarity3d - calculate 3D similarity-type attributes from a migrated data volume.

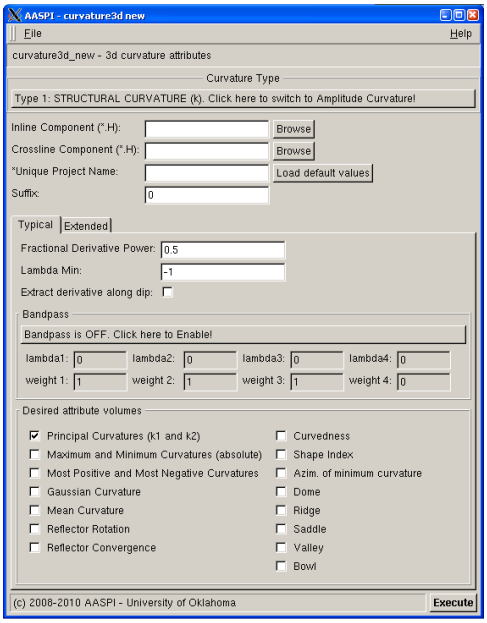


Figure A10: AASPI curvature3d

curvature3d - calculates curvature attributes from an input 2-component vector.

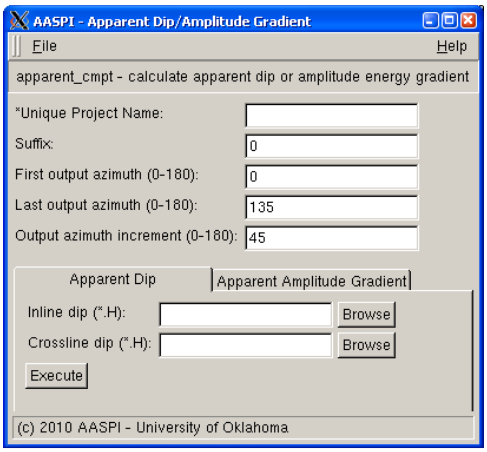


Figure A11: AASPI apparent_cmpt

apparent_cmpt - calculates apparent dip and amplitude gradient attributes from an input 2-component vector.

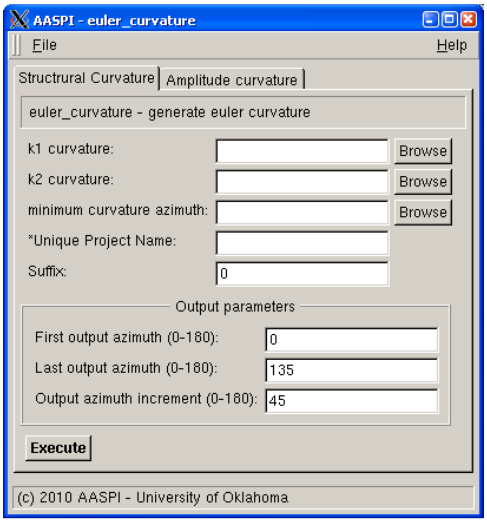


Figure A12: AASPI euler_curvature

euler_curvature - calculates Euler curvature attributes from k_1, k_2 and azimuth of minimum curvature.

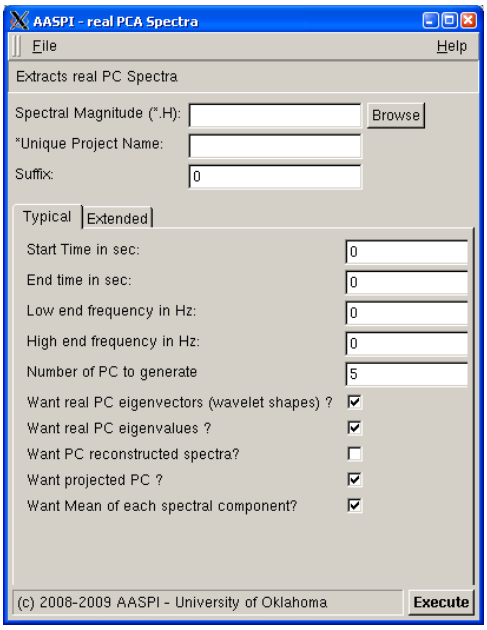


Figure A13: AASPI real_pca_spectra

real_pca_spectra - extract real principal components from a vertical suite of seismic amplitude or spectral magnitude data extracted along an interpreted surface.

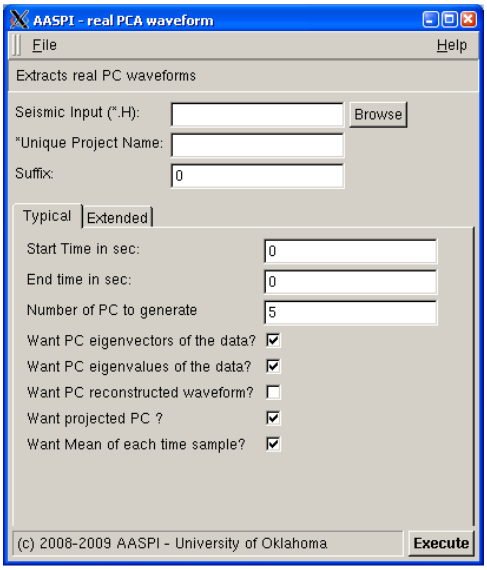


Figure A14: AASPI real_pca_waveform

real_pca_waveform - extract real principal component waveforms corresponding to a window of seismic data extracted parallel to an interpreted surface.

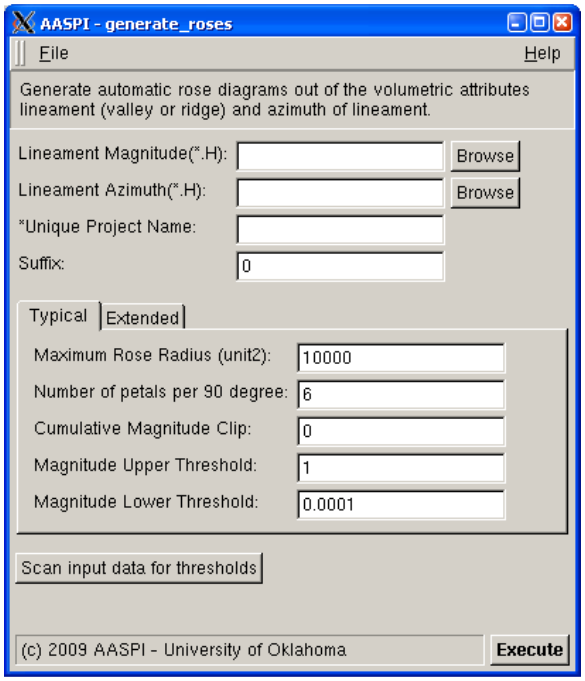


Figure A15: AASPI generate_roses

generate_roses – combine lineament curvedness and azimuth of minimum curvature components and generate 3D rose diagrams.

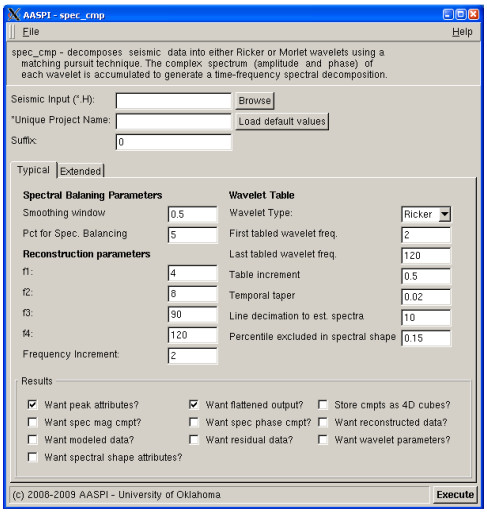


Figure A16: AASPI spec_cmp

spec_cmp – decomposes seismic data into either Ricker or Morlet wavelets using a matching pursuit technique. The complex spectrum (amplitude and phase) of each wavelet is accumulated to generate a time-frequency spectral decomposition.

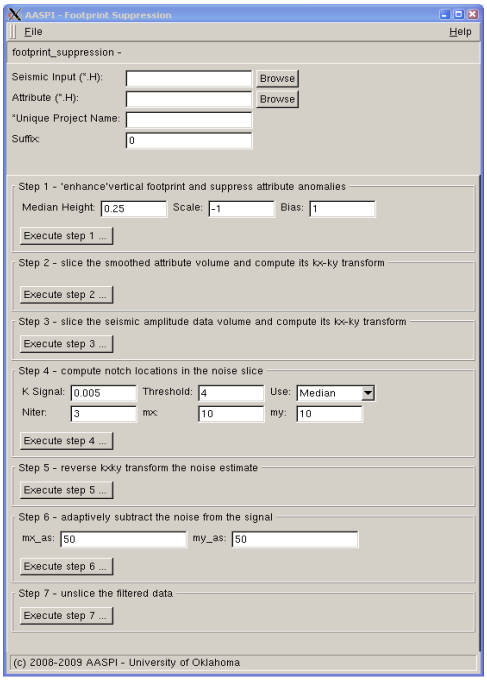


Figure A17: AASPI footprint_suppression

footprint_suppression – a processing workflow remove acquisition footprints.

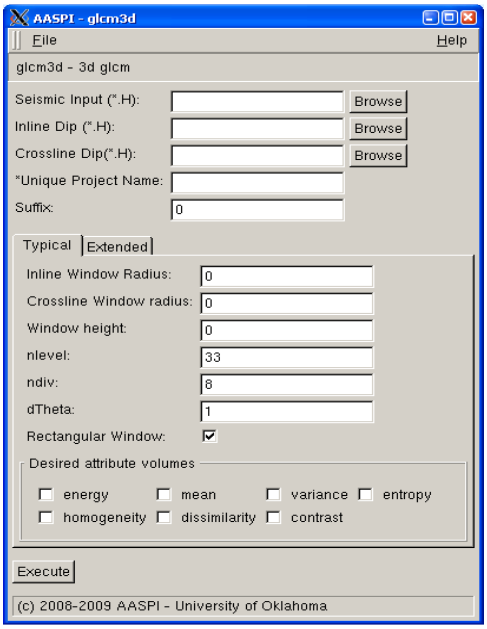


Figure A18: AASPI glcm3d

glcm3d – calculate grey level co-occurrence matrix attributes from a migrated data volume.

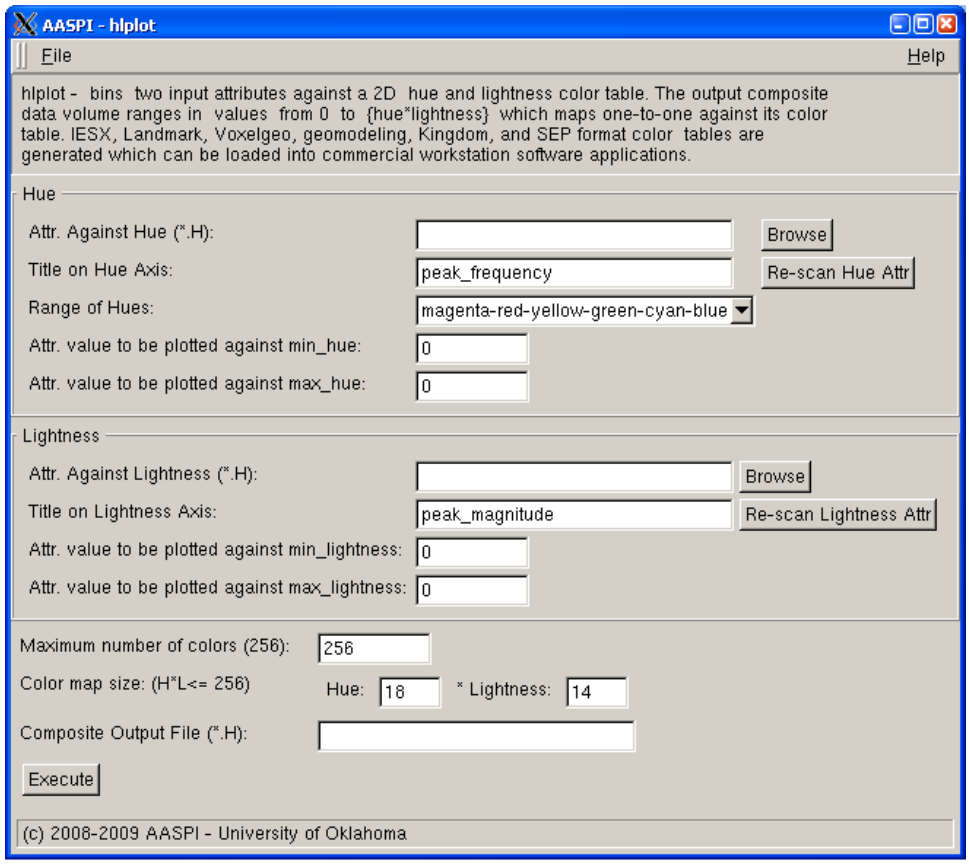


Figure A19: AASPI hlplot

hlplot - bins two input attributes against a 2D hue and lightness color table. The output composite data volume ranges in values from 0 to 255 (or n-color) which maps one-to-one against color tables that range from 0 to 255. Petrel, IESX, Landmark, Voxelgeo, Geomodelling, and SEP format color tables are generated which can be loaded into commercial workstation software applications.

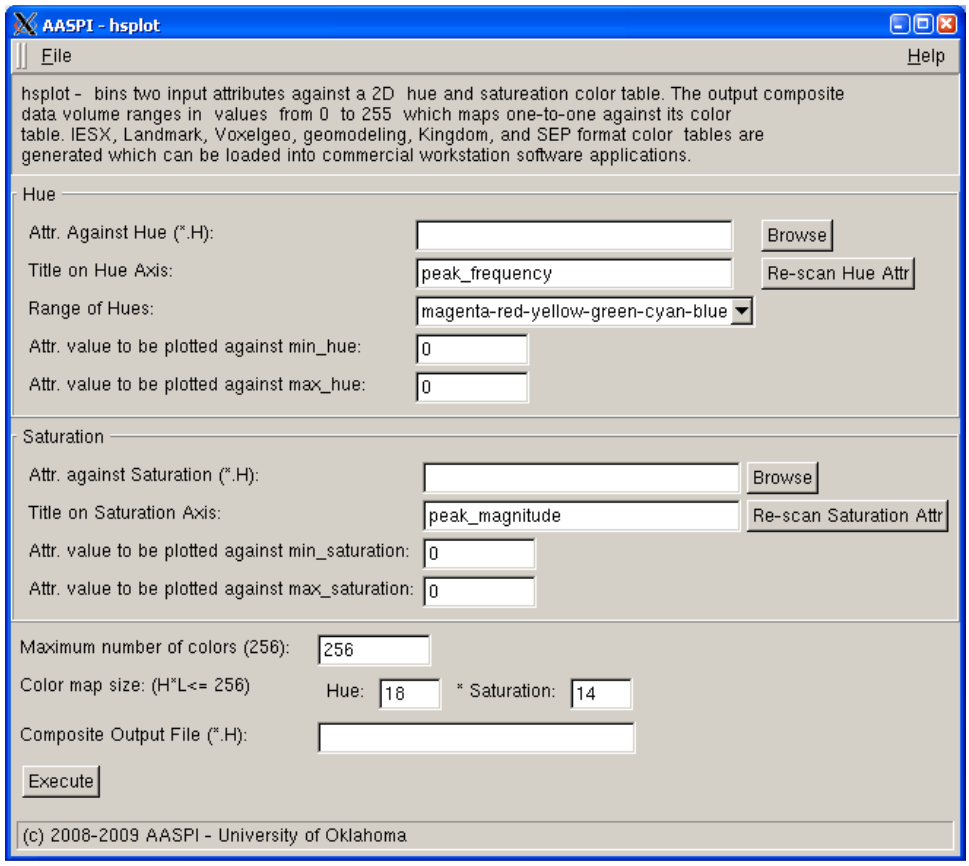


Figure A20: AASPI hsplot

hsplot - bins two input attributes against a 2D hue and saturation color table. The output composite data volume ranges in values from 0 to 255 (or n-color) which maps one-to-one against color tables that range from 0 to 255. Petrel, IESX, Landmark, Voxelgeo, Geomodelling, and SEP format color tables are generated which can be loaded into commercial workstation software applications.

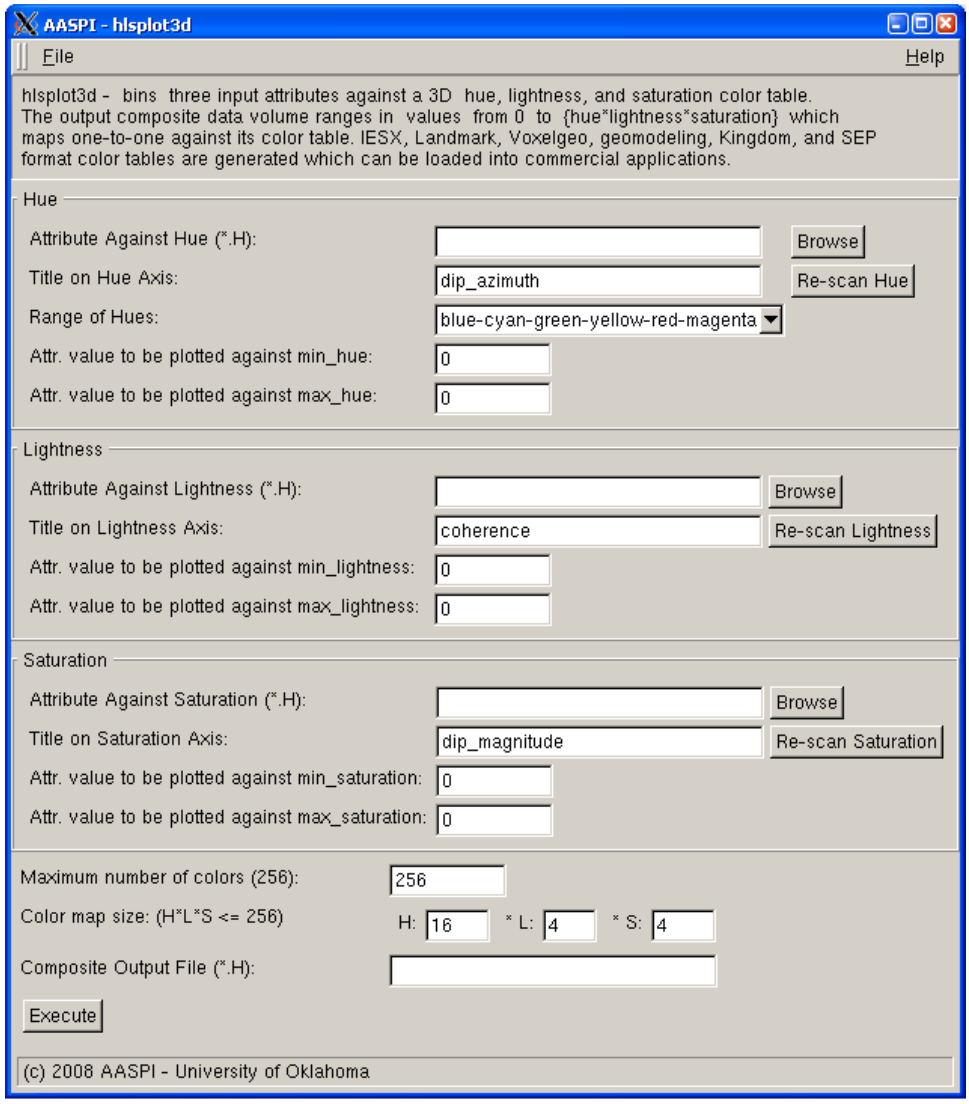


Figure A21: AASPI hlsplot3d

hlsplot3d - bins three input attributes against a 2D hue, lightness, and saturation color table. The output composite data volume ranges in values from 0 to (hue*lightness*saturation) which maps one-to-one against color tables that range from 0 to (hue*lightness*saturation). Petrel, IESX, Landmark, Voxelgeo, Geomodelling, and SEP format color tables are generated which can be loaded into commercial workstation software applications.

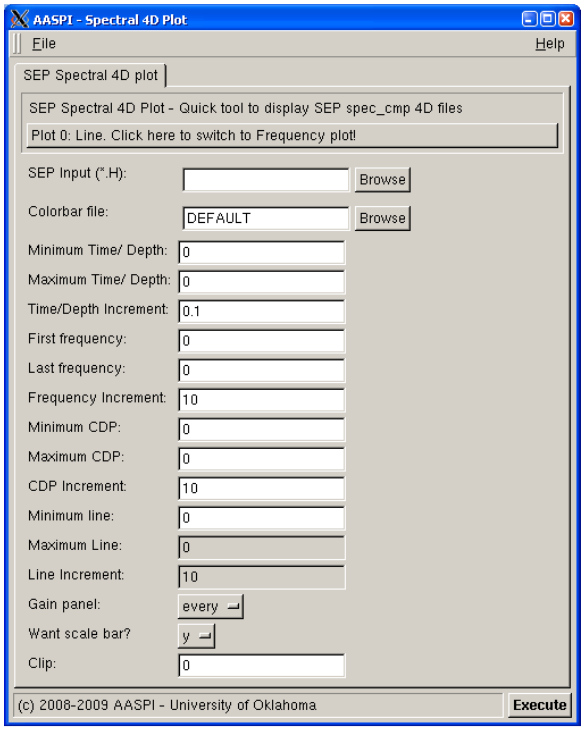


Figure A22: AASPI spec_cmp_plot (4D)

spec_cmp_plot – quick tool to plot SEP spec_cmp 4D volume.